

The economically feasible synthesis of porous silicon for lithium-ion battery anodes via the magnesiothermic reduction of silica at ultra-low temperatures

By:

Maximilian Yan

A thesis submitted in partial fulfilment of the requirements for the degree of
Doctor of Philosophy

The University of Sheffield
Faculty of Engineering
Chemical and Biological Engineering Department

Primary supervisor: Professor Siddharth V. Patwardhan
Secondary supervisor: Professor Solomon F. Brown

29/07/2022

Summary

In the electric vehicle (EV) sector, lithium-ion batteries are the energy device of choice however its energy density still leaves EVs unable to compete with their fossil fuelled counterparts in terms distance travelled on a single refuel event. The search for more energy dense materials has found that the most promising high-energy anode material is silicon, with a theoretical specific capacity 3579 mAh/g, compared to 372 mAh/g for the presently used graphite anode. The capacity of silicon fades quickly due to its anisotropic volumetric expansion of 280% at maximum lithiation capacity, causing the silicon particles to fracture and exfoliate. Creating void space in the silicon allows the dissipation of mechanical stresses, minimising anode degradation. While the existing method of manufacturing silicon is geared towards the transistor and metallurgy sectors, it is not suitable for making porous silicon (p-Si). The method requires temperatures $\geq 2000^{\circ}\text{C}$ followed by etching of the silicon in HF to produce p-Si. The magnesiothermic reduction (MgTR) is an alternative, more efficient bulk method of manufacturing p-Si which operates at 650°C . This method has been researched heavily since its first report in 2007, with studies showing that it can reduce commercial precipitated silica, glass, and even rice husks. The cost of producing p-Si via the MgTR using the methods reported in literature were calculated in this thesis. Strategies for lowering the temperature requirement, whilst increasing the yield and capacity of the p-Si are presented in this thesis.

Acknowledgements

This PhD has presented me with many challenges which I would not have overcome were it not for the people around me. I would firstly like to thank past members of the Energy Storage CDT. Sam Homan, for the many discussions on topics ranging from thermodynamics to particle physics that have benefitted my work and quenched my thirst for knowledge. I started this PhD with a degree in Chemical Engineering and limited knowledge in the field of Materials Science, so I am thankful to Laura Wheatcroft, the knowledgeable materials scientist who was always willing to answer my mostly silly questions on crystallography and phase diagrams. Huge thanks goes to Jake Entwistle for introducing me to the magnesiothermic reduction, enabling me to build a solid foundation of understanding of the field. I thank Laurie Middlemiss for creating a fun and cheerful research environment, livening up the days when work seemed slow, and motivation was low.

Secondly, I would like to thank Dr. Mita Dasog for the privilege of working with her and her talented group chemists. I am grateful to all the members of the Dasog group for creating such wonderful work and social environments, making me feel welcome as a visiting researcher, and as a tourist in Nova Scotia. In particular, I would like to thank Sarah Martell who has an incredible amount of energy and enthusiasm for research. Being able work alongside and bounce ideas off someone with extensive knowledge on the magnesiothermic reduction allowed me to greatly improve my own knowledge base and produce my best work.

Thirdly, I would like to thank the Prof. Gregory Beaucage, for enhancing my experience as a PhD student, encouraging me to engage in extra-curricular activities which allowed me to develop my skills within and without research. My deepest thanks goes to my supervisor Prof. Siddharth Patwardhan for his guidance, patience, encouragement, allowing me to be independent, challenging me, giving me the freedom to make my own mistakes and helping me achieve success.

Finally, I would like to thank Tess, my parents and my sister Samantha for their unending support and patience throughout my doctoral studies.

Contents

1.	INTRODUCTION	1
1.1.	BATTERY FUNDAMENTALS	5
1.1.1.	<i>Capacity of a cell</i>	5
1.1.2.	<i>Electrode potential, cell voltage and energy</i>	8
1.1.3.	<i>Electrolyte</i>	10
1.2.	SELECTION OF ACTIVE MATERIALS	11
1.3.	CATHODE MATERIALS	12
1.4.	ANODE MATERIALS	15
1.5.	CHOICE OF ELECTRODE DEVELOPMENT	19
1.6.	SILICON PRODUCTION	20
1.7.	THESIS STRUCTURE	20
1.8.	REFERENCES	22
2.	LITERATURE REVIEW	25
2.1.	SILICON ANODE	25
2.1.1.	<i>Lithiation and delithiation</i>	26
2.1.2.	<i>Mitigation of expansion associated damage</i>	28
2.1.3.	<i>Porous silicon nanoparticles</i>	31
2.2.	SILICON SYNTHESIS	34
2.2.1.	<i>Electrochemical etching of silicon wafer</i>	34
2.3.	MAGNESIOTHERMIC REDUCTION OF SILICA	36
2.3.1.	<i>Reaction parameters</i>	38
2.3.2.	<i>Thermal control</i>	39
2.3.3.	<i>Techno-economic analysis of the MgTR</i>	42
2.4.	SILICA TYPES, PROPERTIES AND PREPARATION	43
2.4.1.	<i>Silica sol, gel</i>	45
2.4.2.	<i>Precipitated silica</i>	47
2.4.3.	<i>Bioinspired silica</i>	47
2.4.4.	<i>Natural and waste sources of silica</i>	48
2.5.	AIMS	49
2.6.	REFERENCES	52
3.	MATERIALS AND METHODS	57
3.1.	SYNTHESIS	57
3.1.1.	<i>Stöber synthesis</i>	57
3.1.2.	<i>Bio-inspired silica synthesis</i>	57
3.1.3.	<i>Magnesiothermic reduction</i>	58
3.2.	ANALYTICAL TECHNIQUES	59
3.2.1.	<i>Scanning electron microscopy (SEM)</i>	59
3.2.2.	<i>Transmission electron microscopy (TEM)</i>	61
3.2.3.	<i>Powder X-ray diffraction (XRD)</i>	62
3.2.4.	<i>Thermal gravimetric analysis (TGA)</i>	65
3.2.5.	<i>Surface area and pore analysis</i>	67
3.2.6.	<i>Electrochemical testing</i>	71
3.3.	REFERENCES	73
4.	EXPLOITING NANOSCALE EFFECTS ENABLES ULTRA-LOW TEMPERATURE TO PRODUCE POROUS SILICON	75
4.1.	CONTRIBUTION	75
4.2.	GRAPHICAL ABSTRACT	76

4.3.	ABSTRACT	76
4.4.	EXPERIMENTAL METHODS	85
4.4.1.	<i>Materials and reagents</i>	85
4.4.2.	<i>Stöber silica synthesis</i>	85
4.4.3.	<i>Silicon synthesis</i>	86
4.4.4.	<i>Analytical techniques</i>	86
4.5.	ACKNOWLEDGEMENTS	87
4.6.	REFERENCES.....	88
5.	NANOSCALE TRIGGERING EFFECT UNLOCKS SUSTAINABLE MANUFACTURING OF HIGH-PERFORMANCE POROUS SILICON ANODES	90
5.1.	CONTRIBUTIONS.....	90
5.2.	ABSTRACT.....	ERROR! BOOKMARK NOT DEFINED.
5.3.	INTRODUCTION	ERROR! BOOKMARK NOT DEFINED.
5.4.	EXPERIMENTAL METHODS	ERROR! BOOKMARK NOT DEFINED.
5.4.1.	<i>Stöber silica synthesis</i>	<i>Error! Bookmark not defined.</i>
5.4.2.	<i>Bio-inspired silica synthesis</i>	<i>Error! Bookmark not defined.</i>
5.4.3.	<i>Silicon synthesis</i>	<i>Error! Bookmark not defined.</i>
5.4.4.	<i>Analytical techniques</i>	<i>Error! Bookmark not defined.</i>
5.5.	RESULTS AND DISCUSSION	ERROR! BOOKMARK NOT DEFINED.
5.5.1.	<i>Triggering the magnesiothermic reduction</i>	<i>Error! Bookmark not defined.</i>
5.5.2.	<i>Reduction of commercial silicas</i>	<i>Error! Bookmark not defined.</i>
5.5.3.	<i>Electrochemical performance</i>	<i>Error! Bookmark not defined.</i>
5.6.	CONCLUSION	ERROR! BOOKMARK NOT DEFINED.
5.7.	ACKNOWLEDGEMENTS	ERROR! BOOKMARK NOT DEFINED.
5.8.	REFERENCES.....	ERROR! BOOKMARK NOT DEFINED.
6.	LARGE-SCALE MANUFACTURING OF POROUS SILICON VIA THE MAGNESIOTHERMIC REDUCTION: A TECHNO-ECONOMIC ANALYSIS	92
6.1.	CONTRIBUTIONS.....	92
6.2.	ABSTRACT.....	ERROR! BOOKMARK NOT DEFINED.
6.3.	INTRODUCTION	ERROR! BOOKMARK NOT DEFINED.
6.4.	PROCESS OVERVIEW.....	ERROR! BOOKMARK NOT DEFINED.
6.4.1.	<i>Reaction stoichiometry</i>	<i>Error! Bookmark not defined.</i>
6.5.	METHODS.....	ERROR! BOOKMARK NOT DEFINED.
6.5.1.	<i>Demand and costing</i>	<i>Error! Bookmark not defined.</i>
6.6.	RESULTS	ERROR! BOOKMARK NOT DEFINED.
6.6.1.	<i>Baseline and energy costs</i>	<i>Error! Bookmark not defined.</i>
6.6.2.	<i>Feedstock costs</i>	<i>Error! Bookmark not defined.</i>
6.6.3.	<i>Fixed cost and total cost of production</i>	<i>Error! Bookmark not defined.</i>
6.6.4.	<i>Improving and optimising the MgTR</i>	<i>Error! Bookmark not defined.</i>
6.7.	CONCLUSIONS	ERROR! BOOKMARK NOT DEFINED.
6.8.	ACKNOWLEDGEMENTS	ERROR! BOOKMARK NOT DEFINED.
6.9.	REFERENCES.....	ERROR! BOOKMARK NOT DEFINED.
7.	CONCLUSIONS AND OUTLOOK	94
7.1.	CONCLUSIONS	94
7.2.	OUTLOOK	95
8.	APPENDIX.....	98
8.1.	CHAPTER 4 SUPPORTING INFORMATION.....	98
8.2.	CHAPTER 5 SUPPORTING INFORMATION.....	ERROR! BOOKMARK NOT DEFINED.
8.3.	CHAPTER 6 SUPPORTING INFORMATION.....	ERROR! BOOKMARK NOT DEFINED.

8.4. TEA CONDITIONS AND EQUATIONS **ERROR! BOOKMARK NOT DEFINED.**
8.4.1. *Reaction equations* **Error! Bookmark not defined.**
8.4.2. *Annotated Matlab script* **Error! Bookmark not defined.**

1. Introduction

Lithium-ion batteries (LIB) can be found in almost every device in the portable technologies sector. Its high operating voltages ($>3V$) makes it well suited to energy intensive applications such as grid-scale energy storage and electric vehicles. A lithium-ion cell (Figure 1.1) consists of two electrodes immersed in a liquid electrolyte, and connected externally through an electronic circuit¹.

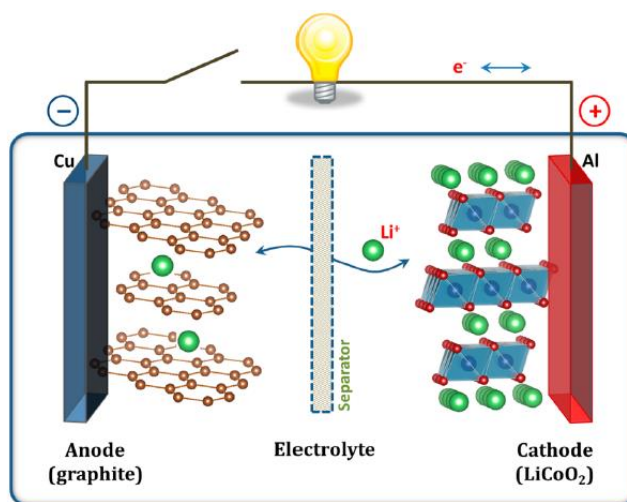


Figure 1.1: Schematic showing key components of a lithium ion cell. Image taken from ref¹.

The electrode material, which is in a powder form, is connected to a current collector – copper for the anode and aluminium for the cathode. A separator is placed in the electrolyte in between the electrodes to prevent contact and subsequent short-circuiting between the two electrodes. To travel from one electrode to the other, lithium ions move through the electrolyte whilst electrons are forced through the external electronic circuit. In this way, the energy from the flow of electrons can be harvested for useful work.

Lithium-ion batteries have greatly benefitted portable devices as well as the broad category of energy storage applications, in a way that preceding battery chemistries have not². Their higher operating cell voltage equates to much higher energy densities than earlier battery technologies, so they have catalysed the development of other technologies that require energy storage, such as electric vehicles, renewable energy generation. The lead acid battery has been used in vehicles with

combustion engines for decades and is suited for low-capacity duties such as ignition and providing auxiliary power. The highest specific energy density that can be achieved with this chemistry is 50 Wh/kg (Figure 1.2)³, an order of magnitude lower than that of lithium-ion cells. Another common cell type is the nickel-cadmium cell. This type of cell is available in AA cell constructions and are used in portable electronic applications. Although this cell possesses a higher specific energy density of 70 Wh/kg higher than lead acid.

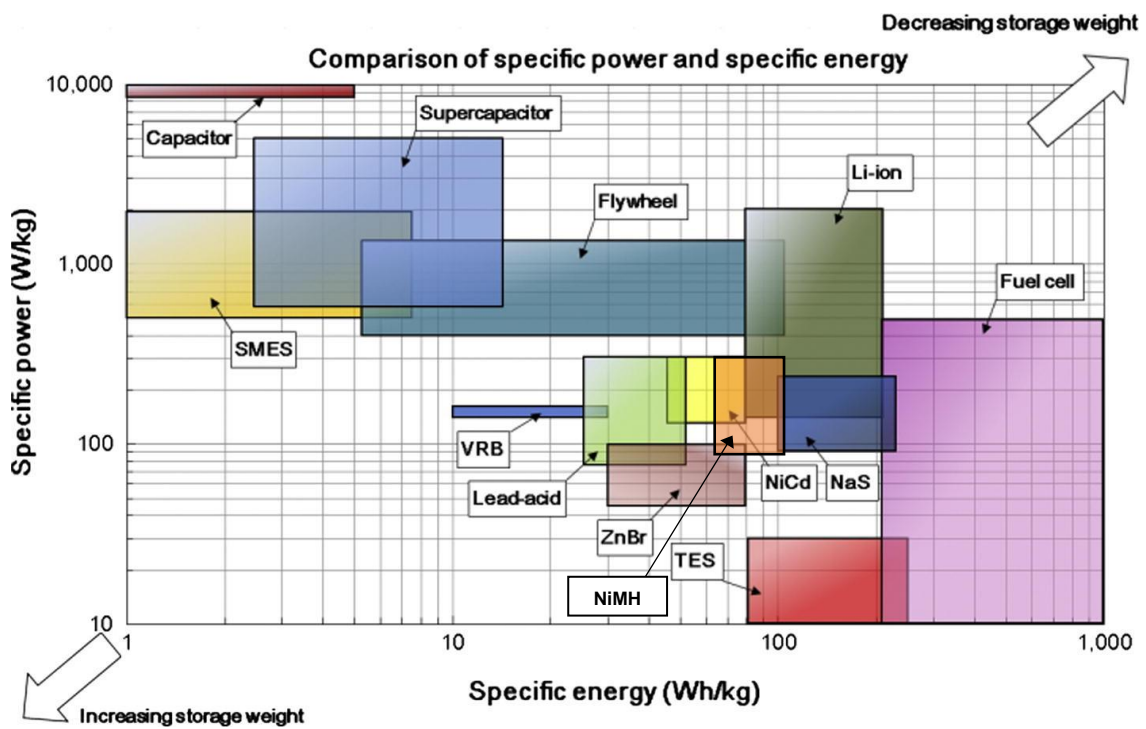


Figure 1.2: Ragone plot comparing the specific energy and specific power of different energy storage devices. Image adapted from³. For clarification, the yellow region represents the specific power and energy of NiCd while the orange region represents that of NiMH.

However, in these sectors, the performance of a lithium-ion battery is still the limiting factor. For example, the energy density (gravimetric and volumetric), although high in electrochemical energy storage terms, is low compared to hydrocarbons, the conventional medium for storing energy in the transportation sector⁴. In general, to store enough energy for a car to travel 500 km, 33 kg of fuel is required whereas a lithium-ion battery weighing more than 10x this amount is required (Figure 1.3)⁴.

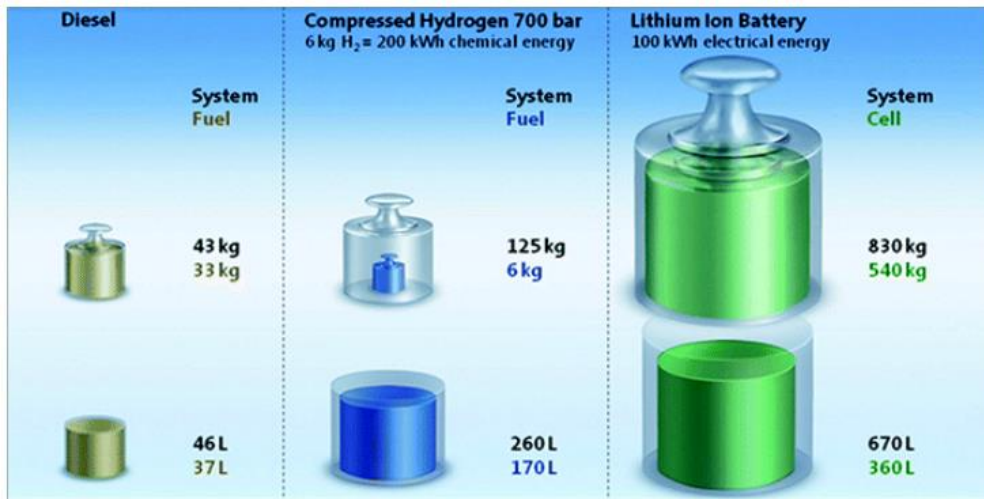


Figure 1.3: The diagram illustrates the difference in energy densities of different energy storage medium in vehicles. Image taken from ref⁴.

Having a heavy battery restricts the total distance a car can be driven before recharging. Due to weight of a lithium-ion battery, the size of the battery that can be put in a car is limited, so the resulting car mileage does not exceed one with an internal combustion engine. Energy density matters, to a lesser extent, in portable electronics⁵. Mobile devices are being designed smaller in form, and more power hungry than ever, demanding batteries with high energy densities.

Looking at energy storage from an environmental angle, the ideal for a method of storing energy is one which consumes far less energy to manufacture than it can store over its lifetime. It was shown that the cost of manufacturing a 1 kWh lithium-ion battery releases 13 kg CO₂⁶. A Nissan leaf with an energy density of 67 kWh would therefore have 871 kg CO₂ associated with its production. This car has a rated distance of 168 miles on a single charge, releasing 93.2g of CO₂/mile assuming a grid CO₂ emission of 233 g/kWh⁷. An internal combustion engine (ICEV) vehicle releases 195 g CO₂/mile⁸. The difference in CO₂ emitted per mile travelled is therefore 102 g less for an EV compared to an ICEV. To offset the 871 kg of CO₂ emitted in the production of the battery, the EV has to have travelled 8540 miles or be charged 50 times. A lithium-ion battery is capable of many more charges than this, which makes LIBs a suitable, low or zero carbon alternative to internal combustion engines. Looking at the breakdown of the energy consumption, it was shown that the greatest proportion of energy consumed in the production of a battery was taken by materials production (Figure 1.4)⁹. Therefore,

it is crucial that improvements are made to the materials production part of a battery manufacturing process.

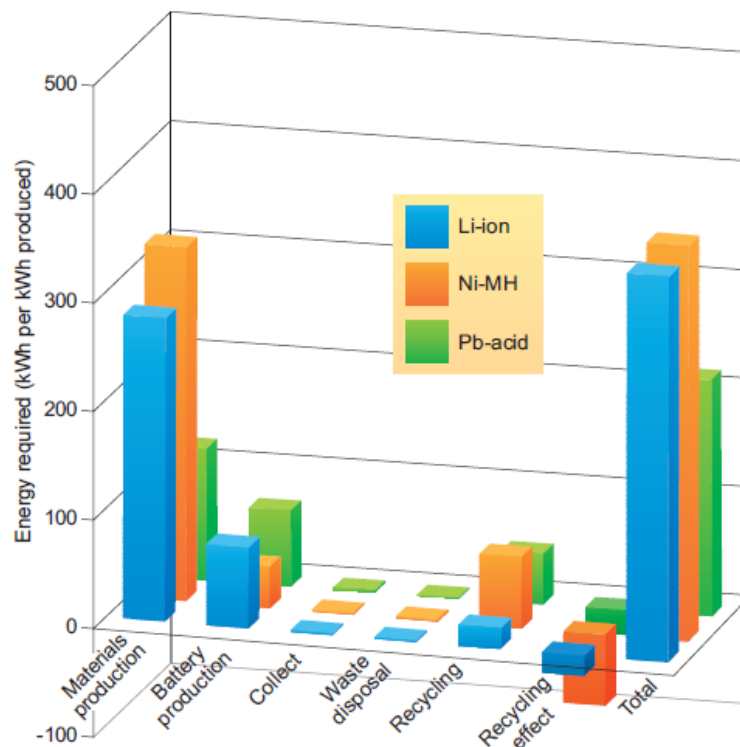


Figure 1.4: The energy consumption of different sectors in the production of a lithium-ion battery. Image taken from ref⁵.

Lithium-ion batteries should not be solely merited based on energy storage metrics such as energy density and CO₂ offset and cost per energy stored. By these quantifications, it is difficult to see why lithium-ion batteries should be considered over other technologies, for example pumped hydro and compressed air energy storage¹⁰. Despite the disadvantages that come with lithium-ion batteries, there are reasons which point to the need for lithium-ion batteries and for its advancement. For portable electronic applications, it is clear that batteries are the answer, and under the umbrella of batteries, lithium-ions are best suited for the power- and energy-hungry electronic devices of the modern day¹¹. In the transportation sector a shift from carbon-based fuels to low-carbon or zero-carbon fuels is crucial for cutting CO₂ emissions and combatting climate change, and batteries will play a major role amongst the fuel cell and plug-in hybrid technologies that will be used in different modes of transportation¹². Lithium-ion batteries are therefore important as a means for storing energy

across various sectors, however they still suffer from high manufacturing costs and large physical size, which sparks the need for research in this field.

This section of the report introduces key components (charge carriers, electrode, electrolyte) of a lithium-ion cell and the relevant parameters (voltage, specific capacity, specific energy) used to measure the performance of these components, which will form a basis for the selection of appropriate materials to use in lithium-ion batteries.

1.1. Battery fundamentals

1.1.1. Capacity of a cell

In a lithium-ion cell, lithium ions move from the anode to the cathode when energy is being drawn from the cell¹³. The lithium ions travel in the opposite direction when the cell is being charged by applying a voltage from an external source. The materials used in the negative electrode (anode) and the positive electrode (cathode) determine the capacity of the cell, measured in units of milliamp-hours (mAh)¹⁴. A cell with a capacity of 1 mAh is able to supply a current of 1 milliamp for 1 hour. This unit can be rewritten in units of coulombs (C):

$$1mA * h = 1 \frac{mC}{s} * 3600 s = 3600 mC \quad (1.1)$$

Therefore, mAh fundamentally indicates the amount of charge. To predict the theoretical maximum capacity of an electrode material, whether it is the anode or the cathode, the appropriate chemical equation for the half-reaction occurring at the given electrode is required. For example, the following half-reaction occurs in graphite, a commonly used anode material in lithium-ion batteries:



Each lithium ion reacts with 6 carbon atoms – that is, 6 carbon atoms are required to store 1 lithium ion. The amount of lithium ions in moles, n_{Li} , that a given mass of carbon, m_c can theoretically react with (and therefore store) is¹⁵:

$$n_{Li} = \frac{m_C}{6 * M_{rC}} \quad (1.3)$$

where M_{rC} is the molar mass of carbon, which is 12 g/mol. The charge on each lithium ion is +1, so associated with the movement of each lithium ion is the movement of 1 electron. The amount of charge (Q_{Li}) in coulombs associated with n_{Li} moles of lithium ions is given by:

$$Q_{Li} = z * n_{Li} * N_0 * e_c \quad (1.4)$$

Where z is the charge number of a lithium ion, in this case, 1, N_0 is Avogadro's constant, 6.022×10^{23} , and e_c is the elementary charge of an electron, 1.602×10^{-19} C. Using equation 1.1, Q_{Li} can be converted from units of coulombs to amp-hours (Ah) by dividing by 3600, then mAh by multiplying by 1000. Table 1.1 gives the values for each of the parameters calculated using equations 1.3 and 1.4, by taking a basis of 1 g of carbon (graphite).

Table 1.1: The amount of lithium, charge and capacity 1 g of graphite can store is shown, calculated using equations 1.3 and 1.4. Capacity was calculated by dividing charge by 3.6.

Parameter	Value	Units
Amount of lithium	0.01389	moles
Charge	1338	coulombs
Capacity	371.7	milliamp-hours

The units for capacity normalised to 1 gram (called specific capacity) of material so that different materials can be compared on a normalised scale (mAh/g).

For a given electrochemical reaction between an electrode material and lithium, the reaction half-equation can be written in the form:



Combining equations (1.3) and (1.4) gives, and generalising for any active material, A , which can undergo a reversible reaction with Li as given in equation 1.5, equation 1.6 can be written as:

$$Q_{Li} = \frac{z \times m_A \times N_0 \times e_c \times y}{x \times M_{rA}} \quad (1.6)$$

where x and y are known stoichiometries from equation 1.5. N_0 multiplied by e_c gives the Faraday constant (F), which takes the value of approximately 96500 C/mol. z is always 1 in the case of lithium, and the specific capacity of a material is given in units of mAh/g, therefore m_A takes the value of 1. Equation 1.6 can then be simplified to equation 1.7:

$$Q_{Li} = \frac{F \times y}{x \times M_{rA}} \quad (1.7)$$

Multiplying Q_{Li} by 1000 and dividing by 3600 converts C to mAh, so the overall equation for calculating the theoretical maximum specific capacity (C_g) in mAh, of a material storing lithium is given by¹⁶:

$$C_g = \frac{y * F}{3.6 * x * M_{rA}} \quad (1.8)$$

Unsurprisingly, the equation indicates that materials with a lower molecular weight result in higher specific capacities. The implications of this will be discussed in the materials selection section of this report (section 2.1).

The steps listed above can be applied for cathode materials. The lithium ions in a cell can only be in one electrode at a time, and only one electrode can be saturated with lithium ions at any given time. When a cell is fully charged, the anode is saturated with lithium ions, and when all the energy in a cell has been spent, the cathode is saturated with lithium ions. To release energy, they have to move from anode to cathode. If both electrodes were saturated with lithium ions, then movement of ions from the anode to the cathode would be impossible, so energy cannot be released. When two electrodes are put together as would occur in a cell, the overall capacity of the cell is equal to the lowest of the two electrode capacities. If one electrode stored significantly more lithium ions than the other, then lithium

ions would move from the former to the latter only until the latter has been saturated with lithium ions; movement of lithium ions would therefore halt since there is no more physical space or chemically available electrode material to accept more lithium ions. The limiting factor in the overall electrochemical reaction is the lower capacity electrode. For this reason, electrodes with similar capacities are used in cells.

It is important to remember that although lithium ions are described here as moving from one electrode to another spatially, redox reactions are occurring between the lithium ions and the electrodes. The electrode is oxidised when a lithium ion 'leaves' it, the electrode is reduced, when a lithium ion 'enters' it.

1.1.2. Electrode potential, cell voltage and energy

Electric current arises from the movement of electrons across a medium. The length of time for which a given current can be sustained by a battery can be calculated as shown in the previous section. While the capacity of the cell tells you how many electrons can be moved to produce a current, to enable the flow of electrons or negative charge, an electric potential is required, the units for which is joules per coulomb (J/C) or, more conveniently, volts (V). The potential of an electrode can be measured with respect to a reference electrode¹⁷. Conventionally, the standard hydrogen electrode is used, so the hydrogen electrode has an electrode potential of 0.00 V by definition. This, along with the more practical silver/silver chloride electrode are used for measurements of aqueous electrochemical systems. Lithium-ion cells operate at voltages exceeding the thermodynamic breakdown potential of water (1.23 V), and will react violently with water, hence measuring potentials of lithium-ion cell electrodes in an aqueous environment is inappropriate. Lithium metal is used as the reference electrode as it satisfies the criteria for reference electrode selection¹⁸; it is stable in the electrolytes that are commonly used in lithium ion cells, and the electrode potential stays practically constant throughout electrochemical measurement. Electrode potential is dependent upon the concentration of its active material (Li in this case) according to the Nernst equation¹⁹, and the

concentration of lithium in the lithium reference electrode is considered to be in excess compared to the working electrode.

When two electrodes of different potentials are placed together in the same body of electrolyte and connected externally through an electronic circuit, a spontaneous redox reaction can occur. Electrons are transferred through the external circuit from the anode to the cathode. An oxidation reaction occurs at the anode, and a reduction reaction occurs at the cathode, and it is the coupling of these reactions that causes the flow of electrons. The direction of flow of electrons, therefore, is from the more reducing electrode to the more oxidising electrode. The overall chemical reaction that occurs will have associated with it a change in Gibbs free energy (ΔG), and from this, the voltage of the cell (ΔE) can be calculated by¹⁴.

$$\Delta E = \frac{-\Delta G}{nF} \quad (1.9)$$

where n is the oxidation state of the active ion and F is the Faraday constant equivalent to the charge of one mole of electrons. It is important to note that the anode is defined as the electrode where oxidation spontaneously occurs and the cathode the electrode where reduction spontaneously occurs²⁰.

When two electrodes with different electrode potentials are coupled, then the open circuit voltage (V_{OC}) of the resulting cell, that is the voltage measured using a high impedance voltmeter, is simply the difference in potential between the two electrodes. This is given by¹⁶:

$$V_{OC} = E_{anode} - E_{cathode} \quad (2.0)$$

where E_{anode} is the electrode potential of the anode and $E_{cathode}$ is the electrode potential of the cathode. The total energy in joules that can be delivered by a cell is the product of the cell's voltage and capacity:

$$Energy\ density = V_{Op} * C_g \quad (2.1)$$

In the same way that specific capacity is used for comparison, specific energy (J/g) of a material is used for meaningful comparison.

1.1.3. Electrolyte

The function of the electrolyte is to conduct lithium ions from the anode to the cathode and vice versa¹⁸. The electrolyte also has to limit electronic conduction so that electrons are forced to flow through an external circuit instead of short-circuiting through the electrolyte. Short circuiting can occur through dendrite formation whereby the dendrites that form on a lithium metal electrode grows across the electrolyte and makes electrical contact with the other electrode²¹. The use of a solid electrolyte curbs this problem however this type of electrolyte suffers from low ionic conductivities. Polymer electrolytes of various types have been developed with beneficial properties such as higher ionic conductivities than solid electrolytes and improved electrode-electrolyte contact which allows for more efficient transfer of lithium ions²². Liquid electrolytes possess the highest ionic conductivities of all the electrolytes due to better electrolyte-electrode contact and low ionic diffusion resistance²³.

The maximum energy that can be delivered by a cell increases with the maximum voltage and therefore ΔG of a reaction. Hence, it seems almost obvious that one will find the best material combination for a high energy lithium-ion battery by coupling lithium redox reactions which give the highest ΔG . However the maximum voltage that can be maintained between the anode and the cathode in a reusable battery is limited by the electrolyte used in the battery²⁴. There is a voltage window, the limits of which were associated with the highest occupied molecular orbital (HOMO) and lowest unoccupied molecular orbital (LUMO) of the electrolyte compound. This voltage window is linked to the stability of an electrolyte in contact with an electrode. If an anode with energies higher than the LUMO or a cathode with lower energies than the HOMO of the electrolyte, reduction or oxidation of the electrolyte would be facilitated by the anode or the cathode respectively²⁴. It was reasoned that because HOMO-LUMO energies are based on electronic structure theory which does not take into account the change in energies due to the presence of an electrode, using HOMO-LUMO energies of an electrolyte offers an inaccurate and only approximate window of stability²⁵. It follows

that although it is a good approximation, it does not coincide with the true window of stability, which is defined by the reduction and oxidation potentials of the electrolyte when in contact with an electrode (Figure 1.5).

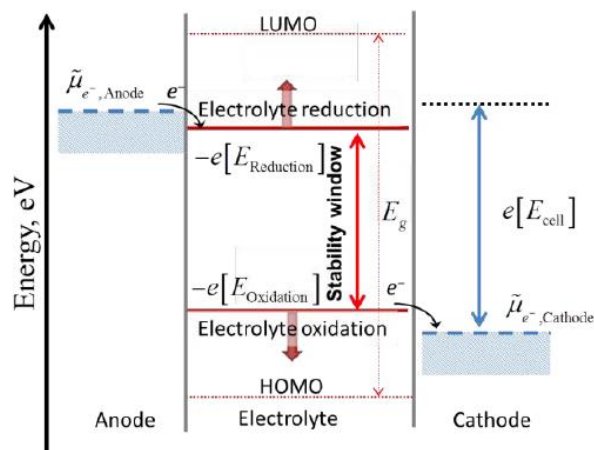


Figure 1.5: Diagram showing the difference between the HOMO-LUMO energies and the actual window of stability of an electrolyte image taken from ref²¹.

The processes by which a cell stores and releases energy, and the parameters that describe the amount of energy that can be stored have been briefly explained here. The amount of lithium ions stored in a cell directly relates to its capacity. Oxidation and reduction reactions occur at the anode and cathode respectively but are coupled to facilitate the flow of lithium ions through an electrolyte and electrons through an external circuit. The reduction and oxidation reactions have associated with them Gibbs free energies, which translate into electrode potentials, and the difference in the potentials gives rise to the voltage of the cell. A higher voltage results in more energy stored, however it is important that the voltage does not exceed the window of stability of the electrolyte so that the electrolyte does not become reduced or oxidised by the electrodes.

1.2. Selection of active materials

It was shown in the previous section that the voltage of the cell is the difference between the potentials of the redox reactions occurring at each electrode. Based on equation 1.8, lighter materials are favoured for high specific capacities. Additionally, the greater the amount of lithium ions (y) to amount

of active material (x), the more electrons stored and the higher the specific capacities. The former point results in the exclusion of heavier elements from consideration when choosing suitable electrode materials and the latter point indicates that transition metals are favoured because they possess multiple oxidation states²⁴. Figure 1.6 shows the elements that are eliminated based on these selection criteria²⁴.

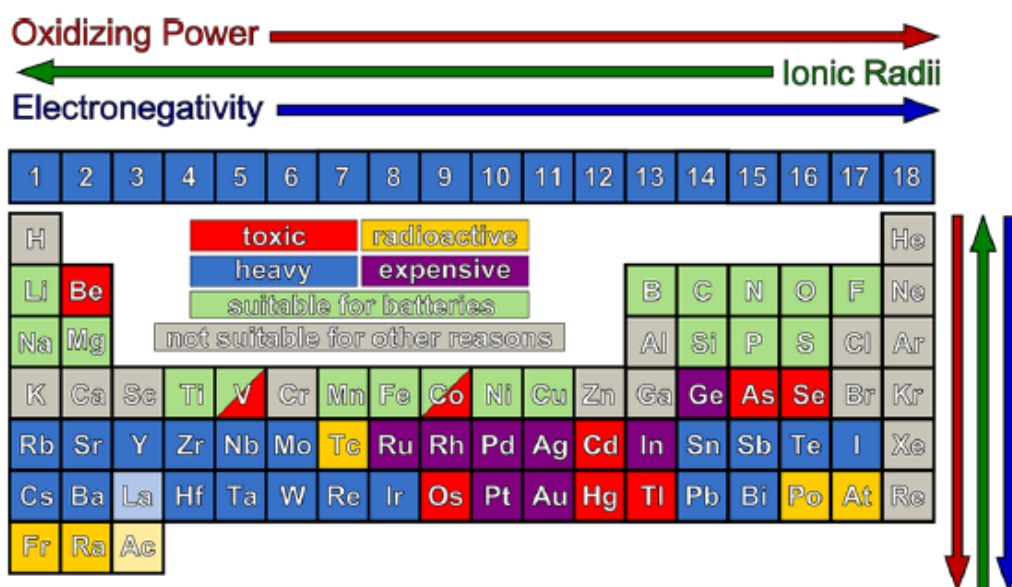


Figure 1.6: Candidate elements for electrode materials in lithium-ion batteries are identified by eliminating elements that are too heavy or too expensive, or unsuitable due to physical state. Black lines mark the boundaries between elements, while vertical red, green and blue arrows indicate oxidising power, ionic radii and electronegativity respectively. Image taken from ref²⁰.

The selection elements are for the fabrication of active materials for lithium-ion batteries. This means that although elements such as H and Zn are used in other battery chemistries (lead acid and NiMH for H and Zn-air battery for Zn), they are deemed unsuitable for LIB chemistries.

1.3. Cathode materials

The characteristics of chemical bonds are determined by electronegativity. The more similar the electronegativities of two elements in a bond, the more covalent the bond. Conversely, the bigger the difference in electronegativities, the more ionic¹⁹. Ionic bonds result in a more densely packed material compared to covalently bonded materials, increasing volumetric capacity. The atomic radii of transition metals decrease with atomic number in the same period. Outer electrons are more strongly

attracted to the nuclei so its binding energy increases. This results in a trend of increasing electric potential going across period 4 of transition metals, as shown in Figure 1.7²⁰. Since cobalt has a higher number of electrons in its outer shell compared to iron and manganese, lithium cobalt oxide, LiCoO_2 , has a higher voltage compared to other transition metal oxides.

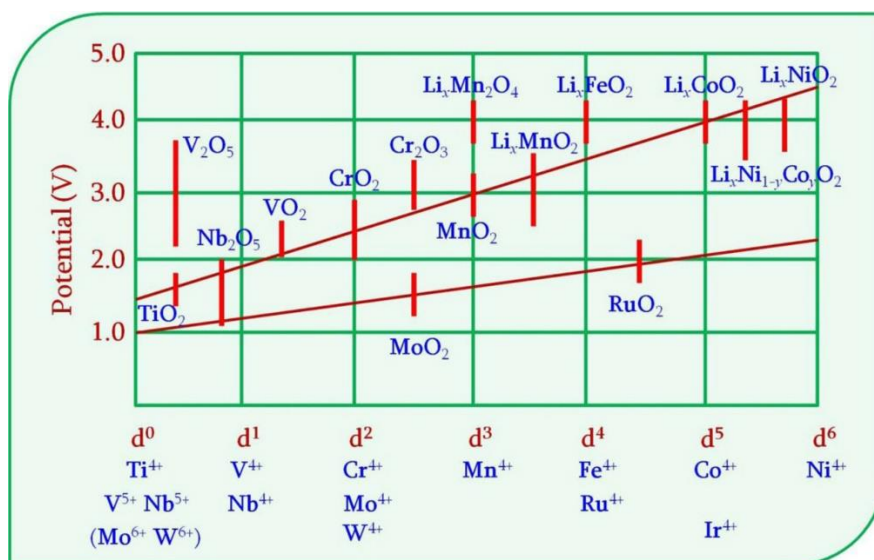


Figure 1.7: Potential of candidate transition metal oxides in period 4. The potential increases with element number. Image taken from ref¹⁶.

The bond of transition metal oxides can be tuned to increase ionic character. Replacing the oxygen anion in Li_xFeO_2 for a phosphate polyanion, PO_4^{2-} , causes the electrons in the Fe-O bond to be pulled towards the covalent P-O bonds, resulting in a higher electrochemical potential of the iron, and a higher voltage seen in the phosphate compared to the oxide²⁶. A trend can also be seen in electronegativity of polyanions and electrode potential (Figure 1.8)¹⁶.

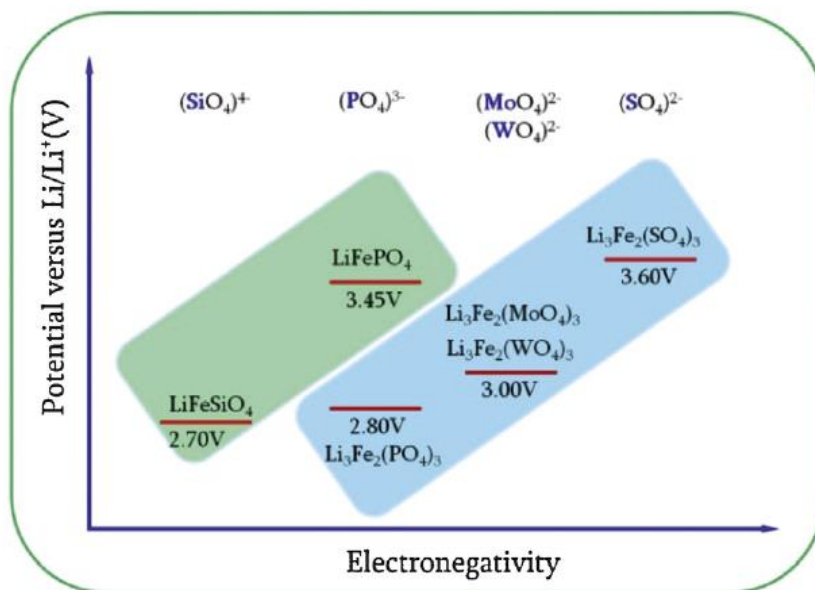


Figure 1.8: The increasing electronegativity of different polyanions leads to an increase in the potential of the electrode. Image taken from ref¹².

A more electronegative polyanion results in a highly ionic bond between the polyanion and the transition metal. The electrons are pulled away from the transition metal, so its redox potential versus lithium increases²⁷.

Another important property of the cathode materials used is the crystal structure. Crystal lattices take the form of layered, olivine or spinel structures, with spaces in the lattice which allow the insertion of lithium during discharge²⁸. For example, the crystal structure can affect the cell's discharge characteristics (Figure 1.9)²⁹.

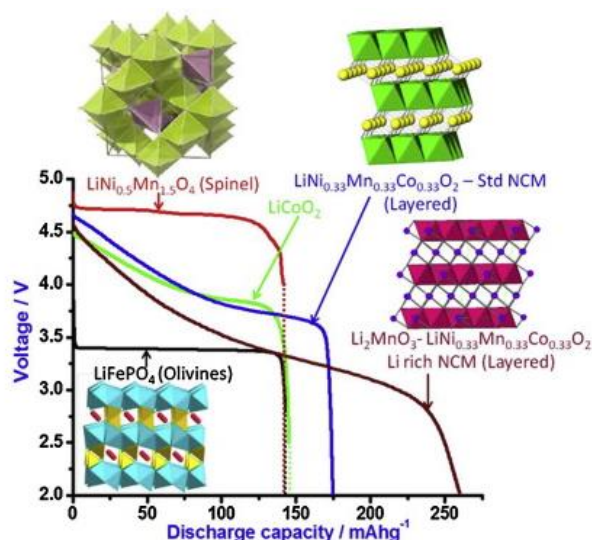


Figure 1.9: Olivine, spinel and layered structures used in cathode materials and their discharge characteristics. Image taken from ref²⁵.

A steep voltage drop upon discharge of a layered structured cathode material is due to the ‘breathing’ of the layers to accommodate the lithium ions. This distortion in structure consumes some energy, which translates to an early drop in voltage, followed by a final sharp drop at the limit of the cell’s capacity²⁹. Conversely in more rigid spinel and olivine structures, the voltage stays constant throughout discharge followed by a sharp drop at the limit of the cell’s capacity.

1.4. Anode materials

In secondary, or rechargeable LIBs, lithium metal was originally used as the anode since it has the most negative electrode potential on the standard hydrogen scale. Being a light metal it has a high specific capacity of 3860 mAh/g³⁰. Lithium metal forms dendrites over multiple cycles which grows into the electrolyte towards the cathode and creates an electronic short circuit, leading to thermal runaway²¹. Due to this safety issue, lithium anodes have been replaced with graphite, which is at present, is the most commonly used anode material in lithium-ion batteries. Lithium ions intercalate in between the layers of graphene during charge and for each lithium ion, 6 carbon atoms are required, as shown in Equation 1.2, rewritten below for convenience.



Anodes and cathodes can be categorised by lithiation mechanism. Intercalation materials, such as graphite and lithium cobalt oxides have crystal structures which lithium ions can move into or out of during charge or discharge. Conversion type materials undergo a change in crystal structure during lithiation/delithiation, and these undergo reactions of the form shown in Equation 1.5 of this thesis³¹. Metals which can alloy with lithium are examples of conversion anodes. Figure 1.10³¹ compares the capacities and relative potentials of groups of electrodes.

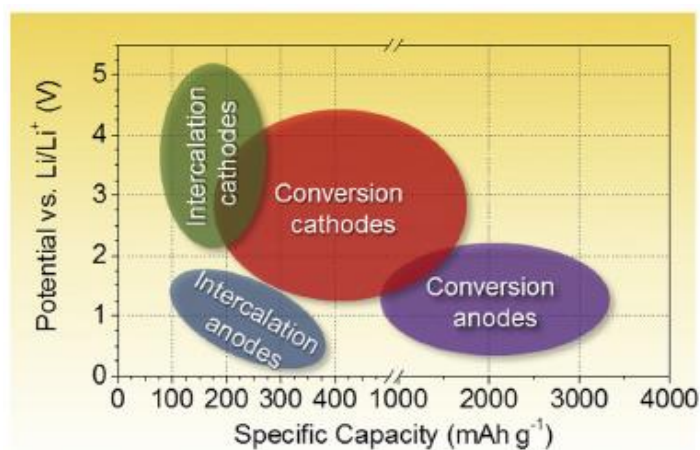


Figure 1.10: Anodes and cathodes are grouped according to lithiation mechanism, which are plotted to compare capacities and relative potentials. Image taken from:²⁷.

The lower the relative potential, the more reducing the material. It is important to note here that electrodes potentials are relative to a standard electrode – in this case lithium – hence the term *relative* potential, measured in volts. From here on, relative potential will simply be referred to as potential, using the reduction potential of Li⁺ to Li as the 0 V standard.

In an electrochemical cell operating in galvanic mode (i.e. the cell is being discharged and current is being drawn), the more reductive electrode material will spontaneously become oxidised, and release electrons which flow to the more oxidative electrode. *By definition, the anode is the electrode which spontaneously becomes oxidised when a cell is operating in galvanic mode*²⁰ so it is the anodes that have lower potentials (close to 0 V). Cathodes with higher potentials are desirable, as with anodes

possessing lower potentials, since it is the difference in the potentials that gives rise to the cell voltage. From Figure 1.10 it can be seen that conversion anodes are the best candidates for improving the specific capacity of lithium-ion cells – their potentials are around 1 V, comparable to intercalation anodes, however they possess almost ten times the specific capacities.

In Figure 1.11³², it can be seen that graphite, the most commonly used anode material at present has one of the lowest potentials, which makes them well suited for their application but it also has one of the lowest capacities. Lithium metal is one of the highest capacity anodes, but as mentioned, suffers from poor cyclability due to formation of dendrites, resulting in thermal runaway.

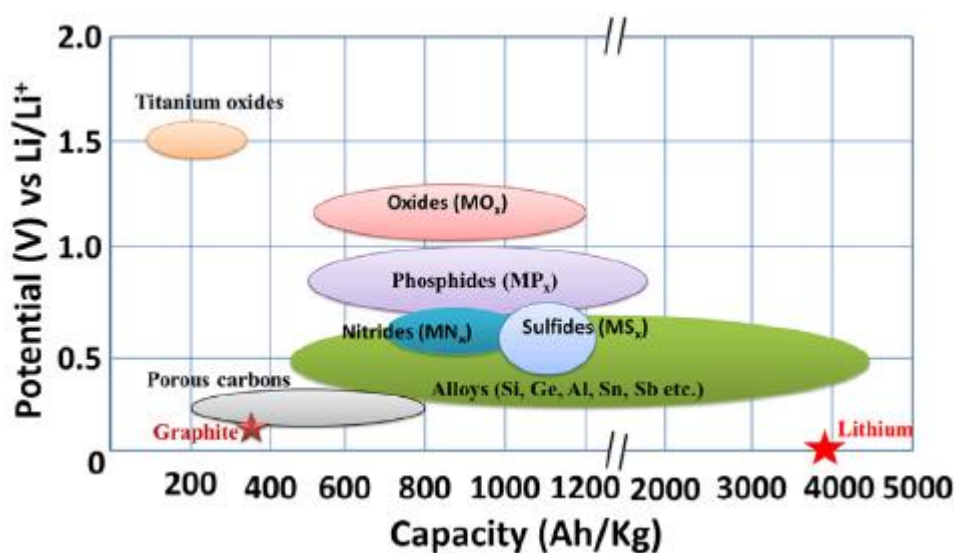


Figure 1.11: The potentials (against a reference Li electrode) of various anode materials. The units of capacity are equivalent to mAh/g. Image taken from:²⁸.

Under the umbrella of conversion anodes are metals which are able to form alloys with lithium. During lithiation/delithiation, the alloy composition changes according to their respective binary phase diagrams. Metals grouped in this category are represented by the green ellipse in Figure 1.11³². These materials have the highest specific capacities and one of the lowest potentials, making them excellent candidates for use in lithium-ion cells. Another notable material is titanium oxide, which, although has an undesirably high potential for an anode, is useful for high power applications due to its ability to deliver a larger current than other anode materials, with minimal damage to its structure³³.

It was first found that lithium was able to undergo spontaneous electrochemical alloying (SEA) with certain metals by Dey in 1971³⁴. Alloying electrode materials exhibit high storage capacity for lithium, much higher than intercalation materials, however, they incur a large volume expansion during lithiation³⁵. Various metals which are capable of forming alloys with lithium have been identified as potential electrode materials³⁶, however as a consequence of the large volume expansion, the lithiation of these materials are largely irreversible. This is due mechanical stress experienced by the material when it expands during lithiation. As a result, the material cracks and loses electronic conductivity and therefore can no longer participate in electrochemical reactions³⁶. It is however, possible to mitigate the destructive effects of the physical expansion by incorporating nano-scaled features into the structure of the material³⁷. A list of some of the metals that can alloy with lithium along with their theoretical specific capacities are shown in Figure 1.12³⁸.

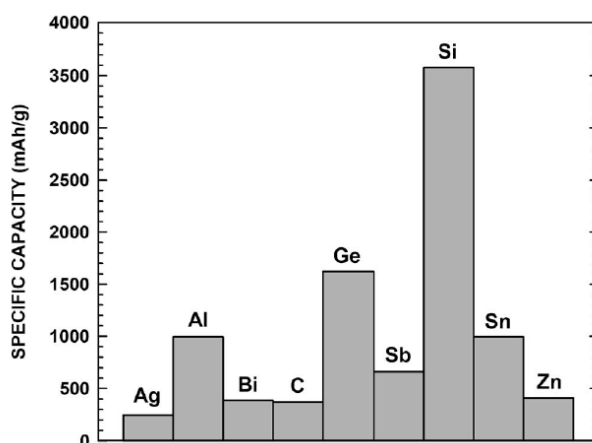


Figure 1.12: Specific capacities of some materials capable undergoing SEA with lithium are shown. Graphitic carbon is included for comparison. Image taken from:³⁴.

Certain metals, however, have additional disadvantages which eliminates them from the shortlist of promising anode materials. Germanium and silver are expensive metals³¹ and tin, antimony, and bismuth, have hindered specific capacities due to their relatively large molecular weight. Of the remaining candidates, silicon possesses by far the highest specific capacity, and is a non-toxic, cheap and abundant element.

1.5. Choice of electrode development

In a lithium-ion cell, the electrochemical potential of the cathode vs. a lithium reference is higher than that of the anode, as shown in Figure 1.9³¹. This difference in potential gives rise to the operational voltage window and the total energy of the cell. Increasing the total energy density of the cell at the cell-chemistry level can be done by increasing the cell voltage window or increasing the amount of lithium-ions that can be stored per unit electrode active material. Of course, there are other components that are required for a cell to be useful in real-life applications. The electrode active materials have to be mixed with conductive and binding additives that create a complete electron conducting pathway. The cells are then packaged in a suitable container containing an ionically conductive electrolyte. These cells are often combined with more identical cells to build a battery pack. This means the final energy density of the cell is the energy arising from its chemistry, divided by the total weight of all the components in the battery pack. It follows that there are plenty of improvements that could be made to the lithium-ion cell at every level from the molecular level to the battery pack level which would indirectly translate to higher energy density.

In full-cell configuration, the cathode and anode capacities have to be matched closely, with the anode's capacity exceeding that of the cathode's for battery safety³⁹. This is called the N/P ratio (negative to positive electrode) and if either exceeds the other greatly ($N/P > 1.5$), this will have implications in the degradation of the cell and the formation of lithium metal which raises safety concerns¹³. Therefore, developments in both the anode and the cathode are needed to increase the energy stored at the cell-level. It has been shown, however, just replacing graphite with a high capacity anode such as Si, a higher energy density can be achieved in a full-cell⁴⁰. Though there are still challenges with using silicon as a pure anode material, silicon can be added in small amounts (5-10 wt%) to graphite anodes to improve the overall energy density. A study has shown that in a full-cell containing LiCoO_2 as the cathode and graphite as the anode, adding silicon has the potential to increase the energy density at the cell level by 15%⁴¹.

In brief, it is important that specific capacities of both cathode and anode are improved proportionally to see the maximum gains in energy density at the cell-level. At present, incremental improvements can be still made to the energy of the cell by using a high-capacity anode such as silicon.

1.6. Silicon production

Silicon is an abundant element on earth, however, does not naturally occur in the elemental form. Silica from broad natural resources such as sand and rock is reduced into silicon via the carbothermal reduction process. This process occurs at 2000°C and produces high purity silicon which can be further purified by zone refining for electronic applications. Silicon melts at 1414°C so this process is unsuitable for producing silicon anodes as the product is non-porous. The pure silicon is electrochemically etched in an electrolyte solution, to leave behind a porous material. To achieve porous silicon (p-Si) from a silica raw feedstock, multiple energy-intensive steps are required.

The magnesiothermic reduction process (MgTR) process can reduce silica to silicon in a single step at 650°C. This is a bulk process whereby the silica is mixed with magnesium and heated in a furnace under inert atmosphere. This process is suitable for producing p-Si since the operating temperature is far below the melting point of silicon. At present there are limitations to the reaction chemistry as well as the process economics which inhibits its scale up.

1.7. Thesis structure

This thesis has been prepared in 'by publication' format. The first results chapter has been published in a peer review journal, and the second two results chapters have been prepared in a format suitable for publication in relevant peer review journals and will be submitted after the submission of this thesis. The chapters have been ordered in this way to create a thesis with a coherent structure. This subsection is written for the purpose of providing each chapter with context under the narrative of the whole thesis.

A review of the literature is laid out in Chapter 2, where the limitations in the magnesiothermic reduction are identified and the aims of the work in this thesis are laid out.

The experimental and modelling methods used in to achieve these aims are given in Chapter 3. The working principles of each method and the procedures were described.

In Chapter 4, the dependence of reduction temperature on the particle size of SiO₂ is demonstrated using monodisperse silica nanospheres. This work has been published in the journal RSC Advances, titled '*Exploiting nanoscale effects enables ultra-low temperature to produce porous silicon*'. In this publication fumed silica around 7 nm are shown to undergo the MgTR at 380°C giving a yield of 54 mol% p-Si. It is well known that as the reduction temperature is decreased, so does the resulting yield of silicon and at 450°C the yield of silicon becomes negligible. The significance of the work in this chapter is that the conditions required for the ultra-low temperature MgTR reaction are now known.

Chapter 5 sees the application of the concept presented in the previous chapter. Commercial and bio-inspired silica was reduced at 380°C, giving high yields of silicon which exhibit favourable electrochemical performance in a lithium-ion cell.

In Chapter 6, the process economics will be evaluated by building an economic model of the process using experimental data presented in the previous chapters and found in the literature. The aim is to calculate the operational cost of producing p-Si via the MgTR process under lab-tested conditions. This is then compared with the price of silicon produced via the current commercial state-of-the-art. Experimental data collected in chapters 4 and 5 is fed into the model to calculate the decrease in cost compared to the reduction at 650°C. The model is also used to calculate the decrease in operational cost under hypothetical, optimised scenarios. This highlights the limiting steps in the process, in terms of operational cost or product throughput, which can be used to inform future experiments in the field.

1.8. References

- 1 J. B. Goodenough and K. S. Park, *J Am Chem Soc*, 2013, **135**, 1167–1176.
- 2 B. Scrosati, *Journal of Solid State Electrochemistry*, 2011, **15**, 1623–1630.
- 3 X. Luo, J. Wang, M. Dooner and J. Clarke, *Applied Energy*, 2015, **137**, 511–536.
- 4 U. Eberle and R. von Helmolt, *Energy and Environmental Science*, 2010, **3**, 689–699.
- 5 M. Armand and J. M. Tarascon, *Nature*, 2008, **451**, 652–657.
- 6 P. Moon, A. Burnham and M. Wang, *SAE Technical Paper*, 2006, 1–375.
- 7 E. and I. S. Department for Business, Greenhouse gas reporting: conversion factors 2020, <https://www.gov.uk/government/publications/greenhouse-gas-reporting-conversion-factors-2020>, (accessed July 28, 2022).
- 8 Department for Transport, New car carbon dioxide emissions, <https://www.gov.uk/government/publications/new-car-carbon-dioxide-emissions#:~:text=The%20average%20carbon%20dioxide%20emissions,of%20carbon%20dioxide%20per%20kilometre.>, (accessed July 29, 2022).
- 9 D. Larcher and J. M. Tarascon, *Nature Chemistry*, 2015, **7**, 19–29.
- 10 H. Kim, D. A. Boysen, J. M. Newhouse, B. L. Spatocco, B. Chung, P. J. Burke, D. J. Bradwell, K. Jiang, A. A. Tomaszowska, K. Wang, W. Wei, L. A. Ortiz, S. A. Barriga, S. M. Poizeau and D. R. Sadoway, *Chemical Reviews*, 2013, **113**, 2075–2099.
- 11 J. M. Tarascon and M. Armand, *Nature*, 2001, **414**, 359–367.
- 12 M. Contestabile, G. J. Offer, R. Slade, F. Jaeger and M. Thoenes, *Energy and Environmental Science*, 2011, **4**, 3754–3772.
- 13 J. K. Park, *Principles and Applications of Lithium Secondary Batteries*, Wiley-VCH, Weinheim, Germany, 2012.
- 14 K. B. Oldham, J. C. Myland and A. M. Bond, *Electrochemical Science and Technology: Fundamentals and Applications*, John Wiley & Sons Ltd, Chichester, 2011.
- 15 D. Deng, *Energy Science and Engineering*, 2015, **3**, 385–418.
- 16 C. Liu, Z. G. Neale and G. Cao, *Materials Today*, 2016, **19**, 109–123.
- 17 G. Inzelt, *Electrode potentials*, Oxford University Press Oxford, 2013.
- 18 D. Linden and T. B. Reddy, *Handbook of Batteries*, McGraw-Hill, Inc, New York, Third Edit., 2002.
- 19 P. Atkins and J. de Paula, *Elements of Physical Chemistry*, Oxford University Press Oxford, Fifth Edit., 2009.
- 20 I. Mills, T. Cvitas, K. Homann, N. Kallay and K. Kuchitsu, *International Union of Pure and Applied Chemistry: Quantities, Units and Symbols in Physical Chemistry*, Blackwell Science Ltd, Oxford, Second Edi., 1993.
- 21 W. Xu, J. Wang, F. Ding, X. Chen, E. Nasybulin, Y. Zhang and J. G. Zhang, *Energy and Environmental Science*, 2014, **7**, 513–537.

- 22 A. Arya and A. L. Sharma, *Ionics (Kiel)*, 2017, **23**, 497–540.
- 23 Q. Wang, L. Jiang, Y. Yu and J. Sun, *Nano Energy*, 2019, **55**, 93–114.
- 24 B. C. Melot and J. M. Tarascon, *Accounts of Chemical Research*, 2013, **46**, 1226–1238.
- 25 P. Peljo and H. H. Girault, *Energy and Environmental Science*, 2018, **11**, 2306–2309.
- 26 A. K. Padhi, *Journal of The Electrochemical Society*, 1997, **144**, 1188.
- 27 C. Masquelier and L. Croguennec, *Chemical Reviews*, 2013, **113**, 6552–6591.
- 28 Y. Mekonnen, A. Sundararajan and A. I. Sarwat, in *Conference Proceedings - IEEE SOUTHEASTCON*, 2016, vol. 2016- July.
- 29 H. D. Yoo, E. Markevich, G. Salitra, D. Sharon and D. Aurbach, *Materials Today*, 2014, **17**, 110–121.
- 30 M. S. Whittingham, in *Proceedings of the IEEE*, 2012, vol. 100, pp. 1518–1534.
- 31 N. Nitta, F. Wu, J. T. Lee and G. Yushin, *Materials Today*, 2015, **18**, 252–264.
- 32 S. Goriparti, E. Miele, F. De Angelis, E. Di Fabrizio, R. Proietti Zaccaria and C. Capiglia, *Journal of Power Sources*, 2014, **257**, 421–443.
- 33 X. L. Yao, S. Xie, C. H. Chen, Q. S. Wang, J. H. Sun, Y. L. Li and S. X. Lu, *Electrochimica Acta*, 2005, **50**, 4076–4081.
- 34 A. N. Dey, *Journal of The Electrochemical Society*, 1971, **118**, 1547.
- 35 C. M. Park, J. H. Kim, H. Kim and H. J. Sohn, *Chemical Society Reviews*, 2010, **39**, 3115–3141.
- 36 R. A. Huggins, *Journal of Power Sources*, 1999, **81–82**, 13–19.
- 37 J. R. Szczech and S. Jin, *Energy and Environmental Science*, 2011, **4**, 56–72.
- 38 M. N. Obrovac, L. Christensen, D. B. Le and J. R. Dahn, *Journal of The Electrochemical Society*, 2007, **154**, A849.
- 39 S. Krueger, R. Kloepsch, J. Li, S. Nowak, S. Passerini and M. Winter, *Journal of The Electrochemical Society*, 2013, **160**, A542–A548.
- 40 D. Andre, S. J. Kim, P. Lamp, S. F. Lux, F. Maglia, O. Paschos and B. Stiaszny, *Journal of Materials Chemistry A*, 2015, **3**, 6709–6732.
- 41 M. Ko, S. Chae, J. Ma, N. Kim, H. W. Lee, Y. Cui and J. Cho, *Nature Energy*, 2016, **1**, 1–8.

2. Literature review

2.1. Silicon anode

Silicon is one of the most promising materials being explored as an anode for lithium-ion batteries. Si undergoes spontaneous electrochemical alloying with lithium, so as it becomes lithiated, it undergoes phase changes according to the Li-Si binary phase diagram (Figure 2.1)¹, moving from the right to the left ordinate.

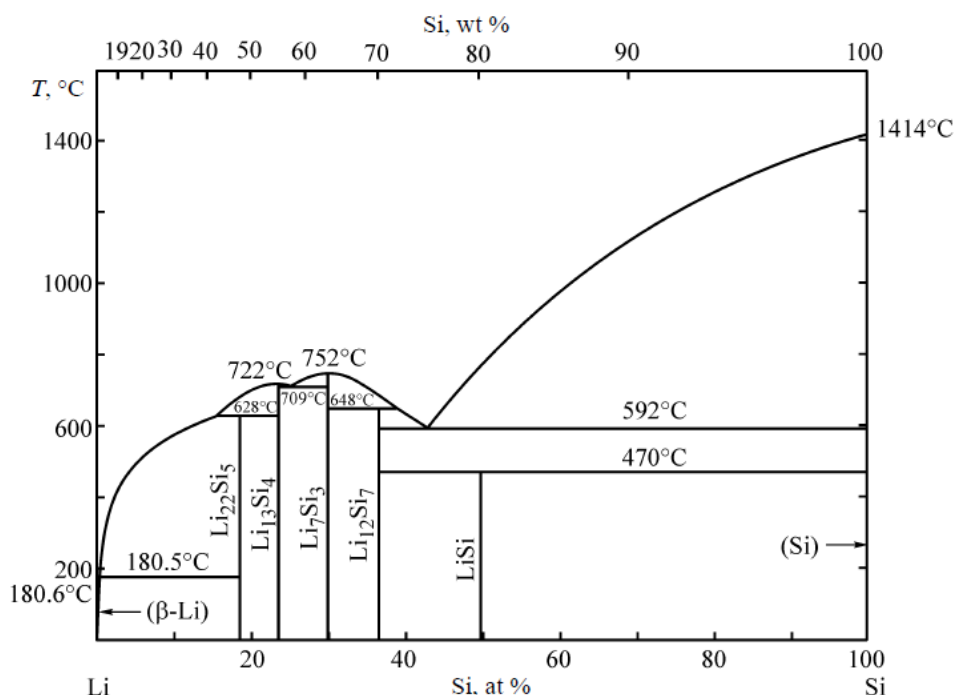
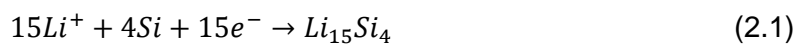


Figure 2.1: Li-Si binary phase diagram. The temperature range of importance for the scope of work is below 200°C, so the $\text{Li}_{22}\text{Si}_4$ phase does not exist within the lithium-ion cell's operating temperature range. Image taken from ref³⁸.

At low atomic percentages (at%) of Si, it can be seen in Figure 2.1 that two Li-Si phases exist. Above 180°C, fully lithiated silicon is present as the $\text{Li}_{22}\text{Si}_5$ phase², however at temperatures that lithium-ion cells are operated, the $\text{Li}_{15}\text{Si}_4$ phase exists³. This alloy of lithium and silicon has a theoretical capacity of 3579 mAh/g⁴ at room temperature which can be calculated using Equation 1.8 in Section 1 of this thesis. This value is calculated using the stoichiometry for the reaction of lithium to silicon to give fully lithiated silicon:



Crystalline silicon will lithiate and become an amorphous alloy. As it moves across the phase diagram (Figure 2.1) from right to left, the mole ratio of Li to Si increases from a minimum to a maximum, hence, the value of y in Eqn. 1.8, increases, thereby increasing its specific gravimetric capacity. During lithiation it undergoes volumetric expansion of up to 280% to accommodate the lithium⁵. During this expansion, individual particles of silicon crack and exfoliate due to the associated mechanical stress⁶. The exfoliated particles become electrically isolated and so do not participate in the redox reactions that store and release energy. This expansion is therefore detrimental to its structure and its ability to store lithium, resulting in a rapid decline in its capacity over multiple charge cycles⁷.

2.1.1. Lithiation and delithiation

Understanding how the process of lithiation and delithiation occurs is crucial in the design of better anodes with high specific energy density as well as durability. Lithiation occurs when lithium ions approach the surface of a body of crystalline silicon (c-Si). An amorphous-crystalline layer forms at the surface of the silicon particle, moving as an amorphous-crystalline interface (ACI) reaction front toward the centre of the particle as the silicon becomes lithiated (Figure 2.2)⁸. The thickness of the ACI does not change as it moves towards the centre of the particle and the crystalline structure is not reformed during lithiation. In that study it was found that due to kinetic favourability, lithium atoms penetrated the crystalline silicon lattice only in the $\langle 110 \rangle$ and $\langle 112 \rangle$ directions, but in the $\langle 111 \rangle$ direction, a ledge peeling mechanism was observed.

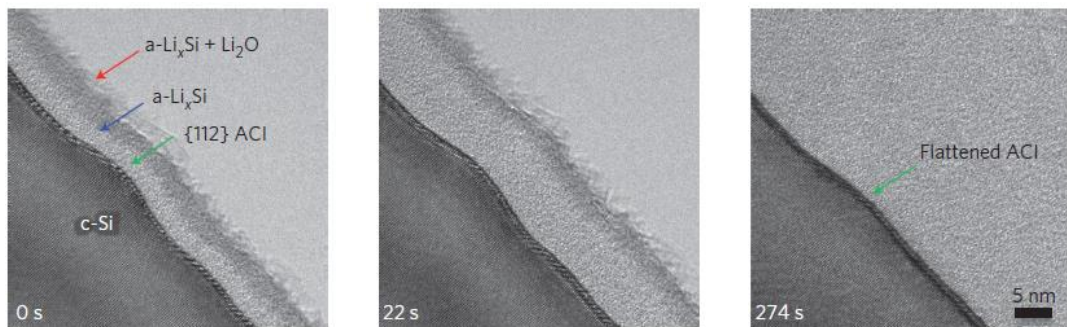


Figure 2.2: Movement of the amorphous-crystalline interface into the crystalline silicon phase during lithiation. Image taken from ref⁴⁴.

During lithiation of amorphous silicon, a shrinking core mechanism is observed similar to the lithiation of crystalline silicon, however the core shrinks isotropically (Figure 2.3)⁹ so mechanical stress is not concentrated in a certain region in the particle.

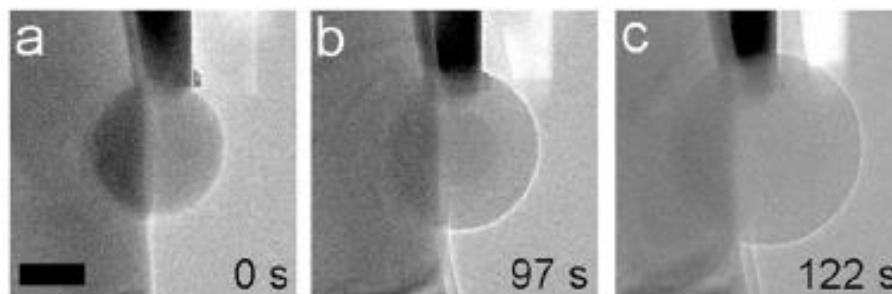


Figure 2.3: (a) Amorphous silicon sphere exhibits two-phase shrinking core behaviour during lithiation. This structure is observed in (b). Further reaction results in the formation of an amorphous particle of lithiated silicon, shown in (c). Image source: ⁴⁵

The fully lithiated silicon is an amorphous alloy, unless cycled below 50 mV in which case the silicon spontaneously crystallises to the $\text{Li}_{15}\text{Si}_4$ phase¹⁰. Regardless of whether the silicon used was crystalline or amorphous, upon lithiation, an amorphous phase forms, which then delithiates as a single phase without a visible reaction front, and subsequent lithiation and delithiation will also proceed in a single phase (Figure 2.4)⁹.

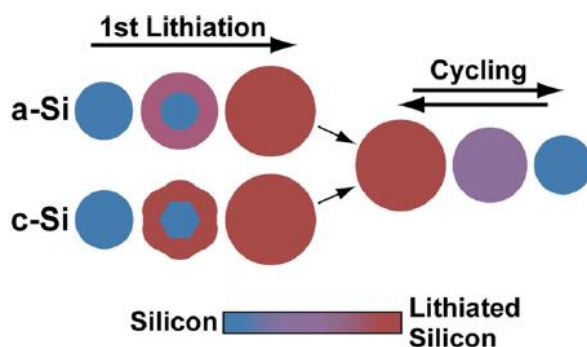


Figure 2.4: Schematic showing the lithiation and delithiation behaviours of amorphous silicon (a-Si) and crystalline silicon (c-Si). Image source: ⁴⁵.

The difference in lithiation and delithiation mechanisms are linked to the way stress is concentrated in silicon particles during lithiation. Crystalline silicon cracks at 150 nm due to anisotropic lithiation – the mechanical stresses are focussed on the crystal faces of the particles. Amorphous silicon lithiate isotropically so the stress is distributed throughout the particle, cracking only occurs when particles are larger than 870 nm ¹¹.

2.1.2. Mitigation of expansion associated damage

Various strategies have been demonstrated to be effective at mitigating the structural damage and subsequent capacity fade of silicon anodes. One of the challenges facing micro- and nanoparticles of silicon is ensuring electrical connection between particles and the current collector. To enable this, the silicon can be made into films, by vacuum deposition as demonstrated in one study by Ohara *et al.*¹² The benefits of this method are that the thickness of the film can be easily controlled and that a conductive connection can be ensured between the silicon at the top of the layer (furthest from the current collector) and the current collector. In that study, a film thickness of 50 nm had a lower capacity fade, maintaining a capacity of 3500 mAh/g after 200 cycles at 2 C rate compared to a thicker film of 150 nm with a capacity of only 2200 mAh/g after the same number of cycles. This is a surface manufacturing method, which is difficult to scale or integrate into existing bulk-process techniques used in the manufacture of electrodes.

Silicon can also be made in nanowire form attached on one end to a substrate current collector, which ensures that all the silicon is electronically connected and can participate in energy storing reactions¹³. The nanowires can be spaced apart on the substrate, allowing room for expansion, and being connected to the current collector eliminates the need for conductive additive and binder. They are capable of expanding and contracting during lithiation and delithiation, filling the void space and avoiding collision induced mechanical damage, achieving a stable capacity of ~3500 mAh/g after 10 cycles. With the aim of avoiding fracture of the anode material, similar structures have been made in other work such as silicon pillars of 1 μm diameter on a silicon substrate¹⁴, achieving ~2800 mAh/g after 23 cycles. Silicon nanotube arrays 150 nm in diameter have also been synthesised in a study by Song *et al.*¹⁵ maintaining a capacity of ~2300 mAh/g after 40 cycles. While nanowires are effective at mitigating structural damage, proven by their high, stable capacities, the method of synthesis, like in films, are surface-based techniques which are slow, costly, and unscalable. In order to meet the demand for Si in LIB, in particular, for transport applications, a bulk method of synthesis is required. The demand of Si in transport applications, and ways to meet this demand will be discussed in Chapter 6 of this Thesis.

Wang *et al.* have shown that hydrogen-bond-directed self-healing binders (SHP) can be used to reverse the effects of mechanical damage that occurs during the lithiation and delithiation of silicon¹⁶. In that study silicon microparticles 3-8 μm in size were mixed with SHP and conductive carbon then put in a cell and it was found that cells were able to retain a high capacity of 2000 mAh/g after 100 cycles. In comparison, the capacities of cells with alginate, CMC and PVDF as binders dropped to 1000, 600 and 400 mAh/g respectively after just 30 cycles. The enhanced cyclability of cells made with SHP was due to the ability of the SHP to stretch, and to reform using the randomly branched hydrogen bonds. While nanotube structures were able to mitigate fracture and exfoliation of active material, this work using SHP takes a different approach, demonstrating that the exfoliation can, to a certain extent, be reversed. This concept supports the use of bulk silicon particles which are easier to synthesise than surface grown nanotubes.

Rather than repairing or minimising the mechanical damage caused by electrochemical cycling, the damage can be avoided altogether by limiting the volumetric expansion. One of the problems associated with the expansion of silicon material over multiple charge and discharge cycles is based on the formation of the solid electrolyte interface (SEI). When an electrode surface comes into contact with an electrolytic solution, a SEI forms where the electrolyte and the electrode meet, which consumes lithium ions and prevents further formation of SEI¹⁷. In silicon anodes, the repeated outward expansion and contraction expose more anode to the electrolyte, which encourages the growth of SEI, and consumes lithium ions, leading to a steady decrease in the overall capacity¹⁸. Double-walled silicon nanotubes have benefit of mechanical clamping of outer tube, limiting the outward expansion of silicon and therefore preventing material fracture and growth of SEI. Wu *et al.* have demonstrated that hollow silicon nanotubes surrounded on the outer surfaces by SiO_x as a mechanical clamp were able to retain a capacity of 600 mAh/g after 6000 cycles¹⁹. The rigid SiO_x outer layer prevented the outward expansion of silicon. Instead, the silicon expanded into the hollow centre. After 6000 cycles the coulombic efficiency of the cell was 99.938%, indicating that degradation rate of the cell was still very low. The motive behind this strategy was to prevent the growth of SEI as a result of repeated exposure of fresh silicon to the electrolyte which occurs during volumetric expansion. Limiting the expansion of the silicon meant that higher volume phases which store the maximum amount of lithium per silicon atom (Li₁₅Si₄) were prevented from forming, so there was a clear trade-off – the cyclability was drastically improved at the cost of specific capacity.

Various nanostructures effective at mitigating, preventing or repairing damage from mechanical stress of expansion have been discussed. To reduce the loss of conductivity, wires, pillars or films were used to ensure good electrical connections between the active material and current collector. To limit the extreme volumetric expansion, silicon could be grown as wires and mechanically clamped with a rigid outer layer, forcing the silicon to expand inward into its own hollow space. To make these structures, surface techniques or complex, energy intensive methods are required which hinders their sustainability and viability for scale-up. p-Si nanoparticles can be made using simpler, bulk

manufacturing techniques rather than surface techniques. The benefits of using this type of silicon will be the focus of discussion in the next section.

2.1.3. Porous silicon nanoparticles

The lithiation of pure silicon results in a volume expansion of 280%, however the accepted swelling limit for anodes is 5% to allow for the inevitable evolution of gases released from electrolyte breakdown²⁰. By incorporating porous volume in the anode, theoretically the swelling can occur within the pores so that the overall outward swelling limit of 5% is not exceeded when the cell is lithiated. By expanding into the pores, not only is the outward expansion avoided, but the mechanical stress between particles is also reduced which minimises damage caused by electrochemical cycling. As a result of this, p-Si shows improved cyclability over non-porous silicon (Figure 2.5)²¹.

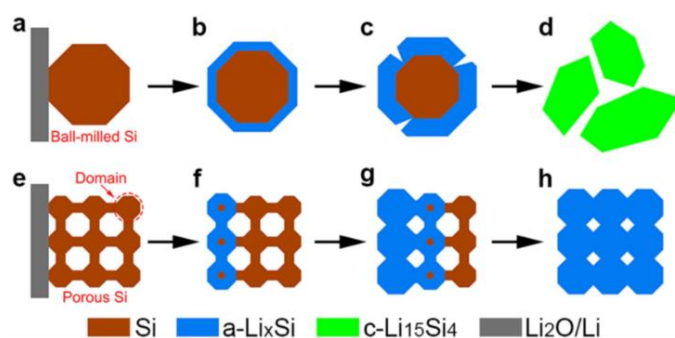


Figure 2.5: Schematic depicting the lithiation behaviour of non-porous (a-d) and porous (e-h) silicon. Image source:⁵⁷.

Particles can consist of internal pores (pores within each distinct particle) or external pores (space between small particles). Void space means lower specific capacities and energy densities however since the specific capacity of silicon is very high in comparison to the cell's capacity (Figure 2.6), this compromise can be made in the interest of cyclability²².

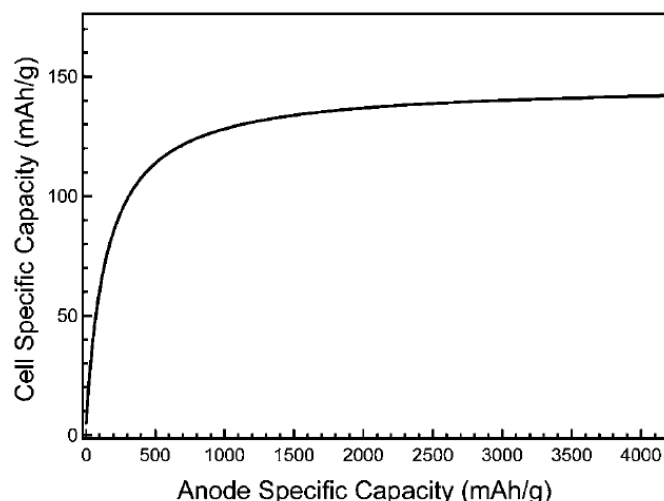


Figure 2.6: Full-cell specific capacity (with LiCoO_2 as cathode) is shown relative to the anode specific capacity, considering only the masses of active materials used and not cell construction materials. Image source:³³.

The maximum theoretical specific capacity of silicon is 3579 mAh/g, however the cell capacity starts to plateau at much lower anode capacities (1000 mAh/g, Figure 2.6)²². Should a silicon-based anode material be developed such that the theoretical maximum is achieved, then in a full cell the mass of silicon required to achieve the maximum cell capacity will be less.

Silicon nanoparticles can be added as a minority component to another anode material with lower capacity (such as graphite) which does not suffer from such drastic volume changes. By replacing a small amount of the lower capacity material with silicon, the overall capacity of the cell is increased²³.

The particle size of silicon determines the performance of a lithium-ion battery. When an anode material comes into contact with an electrolyte, a SEI layer forms at the interface between the two. Smaller particles generally have higher external specific surface area (SSA), which means a larger SEI layer forms compared to bigger particles which tend to have less SSA. However, smaller particles have shown to be beneficial in terms of mitigating stress and shrinking to original size rather than cracking and forming new SEI layers²⁴. In that study, silicon nanoparticles of sizes 5 nm, 10 nm and 20 nm were synthesised and their electrochemical performances were compared. 20 nm particles had the lowest SSA and showed the highest initial coulombic efficiency of 85%. The 10 nm particles, with their increased SSA, showed a lower coulombic efficiency of 80%, whereas the 5 nm particles

showed a coulombic efficiency of 60%. After 40 cycles, the 10 nm particles and 20 nm particles showed the highest and lowest capacity retention of 81% (2750 mAh/g) and 67% (2300 mAh/g), respectively. The 10 nm particles were able to shrink back to their initial particle size after cycling, rather than fracture into smaller particles or grow in size over multiple cycles due to continuous formation of SEI. Furthermore, the initial coulombic efficiency and capacity retention after 40 cycles were improved to 89% and 96% (3393 mAh/g) respectively when the 10 nm particles were coated in a layer of conductive carbon. This improvement in performance was due to the effect of carbon stabilising the SEI layer, by preventing further growth from repeated electrochemical cycling^{24,25}. In another study by Liu *et al.*, it was found that the critical size for fracture of a single particle of crystalline silicon was 150 nm¹¹. As a single particle of c-Si was lithiated, a two-phase, core-shell structure was formed whereby the outer lithiated layer, surrounded the c-Si core. As the c-Si became lithiated it experienced the large volume expansion and the reaction front moved toward the core. The difference in the volume between the surface layer and core led to the development of hoop tensile stress experienced by the lithiated surface layer. This hoop stress was dissipated anisotropically in the lithiated phase which then led to propagation of cracks from flaws on the surface. This size-dependent fracture was not seen in amorphous silicon in particles even as large as 870 nm, due to the isotropic propagation of the hoop stress⁹. It is important to note that while nanoparticles are porous, each particle is not necessarily porous so the pores and SSA are external (interparticle pores), rather than internal pores. The definition of p-Si here refers to particles which may not be nano-sized, however possess pores in the nano regime.

p-Si show great promise as an anode material for lithium-ion batteries. Being a bulk material, they can be added to anode materials with low capacity and low volumetric expansion to incrementally increase the overall capacity of the cell. Their porous structure allowed the particles to expand volumetrically without degrading. Their electrochemical performance is dictated by their structural properties, which needs to be controlled and in the next section, the methods for doing this by tailoring synthesis parameters will be described. In particular, the magnesiothermic reduction will be discussed

as a method for making porous silicon which will highlight further advantages of choosing p-Si nanoparticles over other structures of silicon for lithium-ion batteries.

2.2. Silicon synthesis

Elemental silicon is most widely used for making alloys (metallurgical grade) for various purposes such as electric motors²⁶, engine blocks²⁷, and semiconductors (transistor grade) for electronic devices, the latter requires the highest purity silicon²⁸.

Silicon can be found naturally in sand as quartz, a crystalline form of silicon dioxide. The silicon is extracted via a reduction process using carbon as the reducing agent (Eqn 2.2). This process is called carbothermal reduction and occurs at 2200°C²⁹.

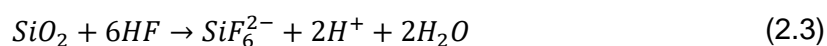


From this, metallurgical grade silicon is made which is between 95-97 mol% pure²⁹. This can be further refined by firstly converting into silane, trichlorosilane, or tetrachlorosilane via hydrogenation or chlorination, then transistor grade silicon via thermal decomposition³⁰. To produce a boule of monocrystalline silicon, the pure silicon is first melted in a crucible. A pulling rod is dipped into the silicon and drawn from the crucible while rotating, forming a boule of monocrystalline silicon. This is the Czochralski pulling process³¹ used to make silicon wafers for the transistor industry.

2.2.1. Electrochemical etching of silicon wafer

Porous silicon was first discovered by Uhlir in 1956 in Bell Laboratories in a study which aimed to produce smooth silicon wafers for electronic circuits using an electrochemical etching method³².

Silicon is etched away from the wafer by the HF, as given in Eqn 2.3:



This method involved the use of a hydrofluoric acid (HF) electrolyte and a platinum electrode. During the study it was found that rather than producing a smooth surface on the silicon wafer, the surface of the silicon wafer was etched unevenly, resulting in a rough and porous structure. This method is a top-down approach whereby external voltage is applied to the silicon and platinum, causing the dissolution of silicon on the surface and leaving behind a porous wafer (Figure 2.7)³³.

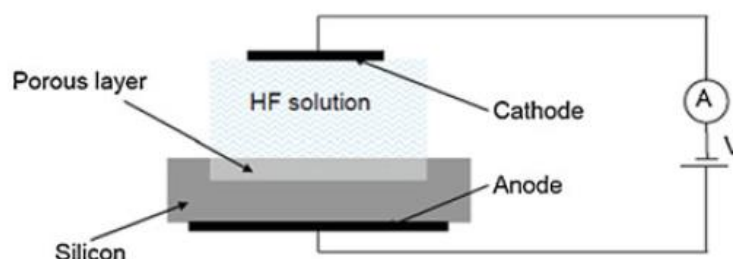


Figure 2.7: Schematic depicting the key components required for the electrochemical etching of silicon. Image source:⁷⁰.

In this process, the operating parameters can be changed in order to give different pore morphologies. These parameters are etching current density, HF concentration, and wafer doping. The etching process begins when an anodic potential is applied to the cell and the surface of the silicon begins to dissolve unevenly. Pore formation occurs at all current densities below a critical current density, above which, pore formation ceases to occur, and instead, electropolishing dominates, creating a smooth rather than a porous morphology on the surface of the silicon. Up to the critical limit, as current density increases, more material is etched and so porosity increases. The current density changes with HF concentration – higher concentrations favour high current densities. Higher concentrations of HF also results in smaller pore sizes formed on the surface of the silicon. N-type doping in the porous silicon leads to the formation of macro- and mesopores, while p-type doping results in micropores.

While this method has its merits including low temperature requirement, high purity of the final product and good control of product properties, it is not without its drawbacks. The first and most important drawback of this method is the requirement of the extremely hazardous chemical, HF which raises issues primarily with process safety but also with sustainability and scalability. Aside from the safety aspects, high-purity silicon is also required as the feedstock which is produced via the carbothermal

reduction method. A second drawback relates to the suitability of the silicon produced for the application of lithium-ion batteries. This is a surface technique and wafers are made with pores etched into one of the surfaces. The active material in an electrode of a lithium-ion battery is in the form of a powder spread on a current collector rather than a single solid material with an etched surface, so silicon wafers made by electrochemical etching would be difficult to integrate into existing cell configurations³⁴ and manufacturing infrastructure³⁵.

From a cell performance viewpoint, porous silicon powder is more suitable for the application over porous wafers. It was found in a study that particles of silicon smaller than a critical diameter (150 nm) exhibit greatly improved cycling capabilities in a lithium-ion cell compared to particles larger than this diameter due to better management of mechanical stress¹¹. Porous silicon made via electrochemical etching does not give individual nanoparticles, but a single, continuous wafer of silicon with pores throughout.

In short, the drawbacks of this method of producing porous silicon are the need for hazardous chemicals and high purity feedstock, the incompatibility of the silicon product with lithium-ion cell architecture and unsuitable morphology. Clearly, to manufacture silicon for use as anodes in lithium-ion batteries, a more suitable process is required. The details of a more appropriate process are discussed in the following section. This is the MgTR process, which is a bulk synthesis method that produces powdered porous silicon from a wide variety of silica feedstock without the requirement of extremely hazardous chemicals.

2.3. Magnesiothermic reduction of silica

One method of producing porous silicon that has a huge potential for scaling up is the magnesiothermic reduction reaction (MgTR). Unlike electrochemical etching, this is a bulk method whereby a stoichiometric amount (Eqn. 2.4) of silica is mixed with solid magnesium and heated in an inert atmosphere. The products include silicon, magnesium oxide, magnesium silicide as well as unreacted magnesium and silica. The silica used for this reaction is dry and usually in powder form

to promote mixing with magnesium, however silica sources such as sand³⁶ and crushed glass³⁷, which are coarse in comparison have also been used.



The same reaction can also occur between gaseous Mg and solid SiO₂, with a higher reaction enthalpy of 546.42 kJ mol⁻¹. The feasibility of a coupled redox reaction can be determined from the Ellingham diagram, shown in Figure 2.8³⁸. Oxidation reactions of metals are shown, with their corresponding reaction Gibbs free energy (ΔG°) at different temperatures. The oxidation of magnesium at any given temperature has a lower Gibbs free energy than the oxidation of silicon, hence, at all temperatures the MgTR can proceed, and the reduction of magnesium oxide by silicon cannot. Additionally, the oxidation of C to CO has a ΔG° which decreases with temperature, meeting with the line corresponding to the oxidation of silicon at around 1800 K. Above this temperature the ΔG° of the latter reaction is greater than that of the former, and carbon is able to reduce silica. This is why the carbothermal reduction of silica requires high temperatures to proceed, however, the MgTR does not. Si can be further reduced by Mg to form the intermediate product Mg₂Si. This intermediate can then be oxidised, forming Si and MgO. In a furnace at temperatures above 450°C and under flowing Ar, reactions 2.4, 2.5 and 2.7 can occur. Reaction 2.6, which is the oxidation of Mg₂Si by O₂ cannot proceed in a properly sealed furnace but can proceed at 500°C if O₂ is fed into the furnace³⁹.

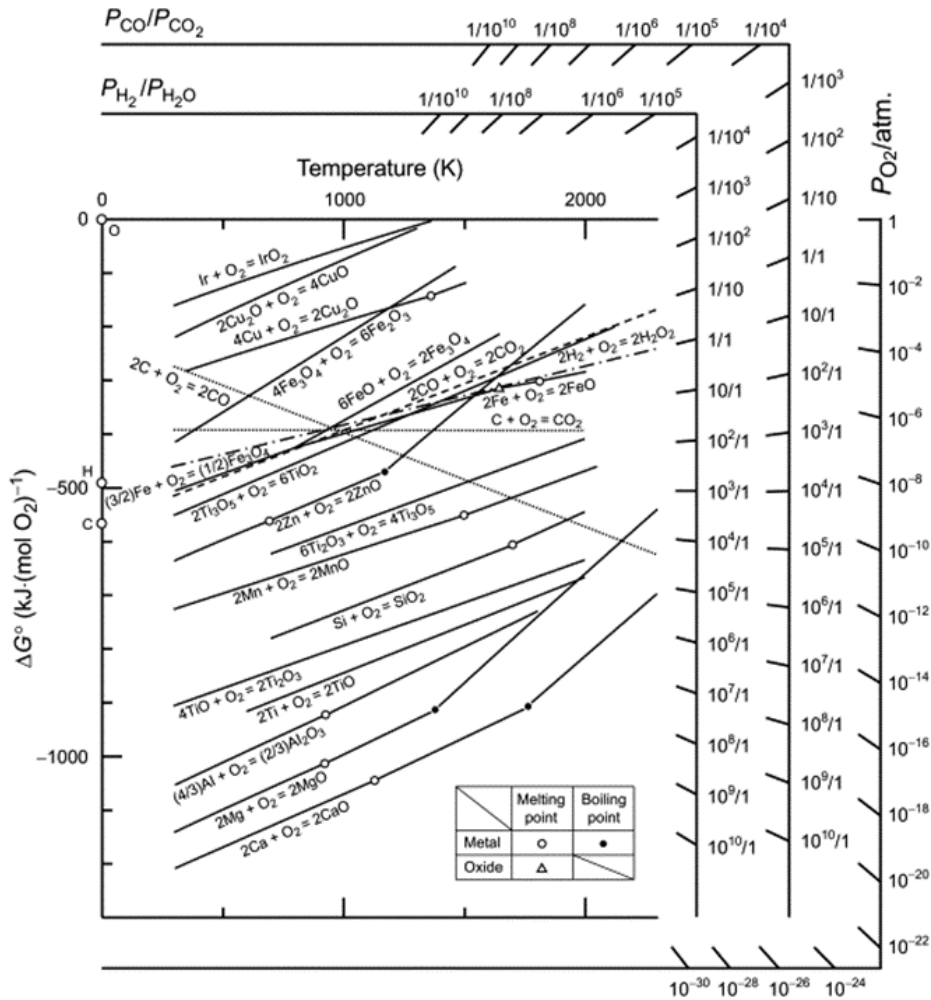


Figure 2.8: Ellingham diagram showing the change in Gibbs free energy of oxidation of metals with temperature.

Image source:⁴⁰.

2.3.1. Reaction parameters

Typically, the mixture is heated in a furnace $\geq 650^\circ\text{C}$ (the melting point of magnesium) for 1-6 hours under flowing argon. It has been shown that reaction times as short as 30 minutes at 650°C is enough to produce porous silicon however the yield was not reported in that study⁴¹. Reaction times between 1 and 10 hours are most common and it has been shown that the reaction reaches completion within 2 hours and does not increase with longer reaction times⁴². The temperatures used for the MgTR are far below the melting point of silicon (1414°C) so a porous structure can form without collapsing. At 650°C , the solid, liquid and vapour forms of magnesium are present, and each of these phases will react with silica. Magnesium begins to form a significant vapour pressure at 400°C , with a vapour

pressure of 1 Pa at 428°C. Due to its volatility, when silica and magnesium are placed in a sealed reactor without being in contact with each other, the magnesium vapour, is able to migrate towards the silica and chemically reduce it, forming MgO and porous Si⁴³. After the heating stage, the mixture is allowed to cool naturally, then removed from the furnace and etched in 1M HCl in order to remove the MgO by-product and unreacted Mg by dissolution. What remains is a powder, which is separated by filtration and dried. This powder contains silicon and silica, and separating the two requires the use of HF to dissolve the latter. This step is the most hazardous and unsustainable part of the whole process and elucidates the need to achieve high yields of silicon especially in the context of process economics and scalability. Increasing the ratio of Mg to SiO₂ used favours a parasitic side reaction which generates the undesired by-product magnesium silicide (Mg₂Si)⁴⁴, however this can be converted into silicon through an additional oxidation step. A silicide oxidation route takes advantage of this reaction route, producing Mg₂Si at 500°C then oxidising at 600°C to produce mesoporous silicon with a yield of 90%³⁹. This method is not economical as the amount of Mg required is in large excess. The impact of Mg on the cost of production will be discussed further in Chapter 6.

2.3.2. Thermal control

Although silicon does not completely melt at the low temperatures of the MgTR reaction, sintering still occurs due to its exothermic nature⁴⁵. This is undesirable as sintering also leads to pore collapse in the silicon product. Thermal control needs to be implemented in this process, in order to produce silicon with favourable pore properties and limit the amount of sintering which occurs during the reaction. To do this, the effects of certain basic parameters such as furnace temperature and ramp rate on the pore properties and yield of the silicon product need to be understood.

As the maximum furnace temperature used for the reduction increases, sintering is promoted, resulting in larger average pore diameters, loss of pore volume and a decrease in the specific surface area (SSA). This was shown in a study where bio-inspired silica was mixed with a stoichiometric amount of Mg and reduced at temperatures between 550 and 850°C⁴². The reduction carried out at 550°C resulted in a product with an average pore diameter of 4 nm and a SSA of 402 m² g⁻¹, however

when carried out at 850°C, the product had an average pore diameter of 34 nm, and a SSA of 110 m² g⁻¹. It was shown that in contrast to the pore properties, the yield of silicon is favoured at higher temperatures, whereby at 550°C the wt% yield of silicon by weight, measured by oxidation methods, was 29 wt%, increasing to 87 wt% for a reduction carried out at 850°C. At temperatures between 750 and 950°C, higher temperatures have been shown to decrease the formation of Mg₂Si⁴⁶. This intermediate product reacts with SiO₂ to form Si and MgO, and the kinetics of this reaction is favoured at higher temperatures, hence, improving the yield of Si. From an economic perspective an improvement in the yield is beneficial however such high temperatures make this process highly unsustainable, so in selecting the correct temperature, one aspect (economics or environmental impact) will be favoured at the cost of the other.

With regards to the rate of increase in furnace temperature, higher ramp rates add large amounts of heat to an already hot reaction mixture. This leads to excessive heat build-up which can melt the silicon and encapsulate the MgO by-product, making it difficult to be removed from the acid etching step. In one study, it was reported that when a ramp rate of 5°C/min was used, the resulting mesoporous silicon had a SSA of 240 m² g⁻¹ whereas when the rate was increased to 40°C/min, macroporous silicon was produced with a SSA of 54 m² g⁻¹³⁶. In short, to limit sintering of the porous silicon product, it is important to avoid excess heat build-up in the mixture, so lower furnace temperatures and ramp rates should be used for the MgTR reaction. If a higher yield is desired then the furnace temperature should be increased at low ramp rates.

In addition to controlling the basic parameters, the protocol for the MgTR process can be modified to add another layer of thermal control. Various methods for dampening the large amount of heat released by the reduction have been successfully employed to produce porous silicon with improved structure and pore properties. Salts can be used as heat sinks which absorb excess heat either as sensible heat or latent heat (melting), thereby limiting sintering. It was first demonstrated by Luo *et al.* that when NaCl was added to a reduction mixture the resulting silicon had inherited the morphology of the feedstock silica with superior pore properties⁴⁷. A mixture with NaCl produced silicon with a SSA of 295.5 m² g⁻¹ at 650°C with a dwell time of 2.5 hours whereas a mixture without NaCl under the

same conditions produced non-porous silicon with a SSA of $5 \text{ m}^2 \text{ g}^{-1}$. In a systematic study of various heat sink salts, it was shown that salts with higher heat capacities serve as better thermal moderators for the purpose of producing porous silicon⁴⁸. In this study, when silica was reduced in the presence of calcium chloride at 650°C , the SSA of the silicon produced was highest ($465 \text{ m}^2 \text{ g}^{-1}$) compared to when other salts were used. Through Scherrer analysis it was found that the crystallite size of this silicon sample was the smallest (9.4 nm), indicating that the available heat for crystal growth was the lowest. The particle size of the magnesium powder was shown to have an effect on the thermal characteristics of the reduction reaction⁴⁹. When larger particles of magnesium were used, the rate of reaction proceeded at a slower rate, hence the exothermic release of heat from the reaction is limited. Silicon formed from reduction by larger magnesium particles (4 mm) had pore diameters centred around 10 nm, with a SSA of $228.3 \text{ m}^2 \text{ g}^{-1}$ and when smaller particles (4 μm) were used, the silicon consisted of macropores centred around 80 nm, with a SSA of $56.8 \text{ m}^2 \text{ g}^{-1}$. Thermal moderation can also be achieved by varying the temperature of the furnace during reduction. Martell *et al.* demonstrated that once activated, the MgTR reaction produces enough heat so that further reactions can continue with minimal addition of heat⁵⁰. When the reaction mixture was firstly heated to 650°C for 30 minutes then cooled to 300°C for the remainder of the duration, excessive sintering was not seen in the sample, resulting in porous silicon with a surface area of $542 \text{ m}^2 \text{ g}^{-1}$.

One reported method for producing porous silicon via MgTR below 650°C requires the use of a eutectic mixture of magnesium and aluminium⁵¹. It was shown that because the eutectic mixture could melt at 450°C the reduction of SiO_2 could proceed at this temperature. As a result the spherical structure of the Stöber silica used in the study was preserved during the reduction and inherited by the silicon product proving to be an effective method of reducing silica at low temperatures. The drawback, however, is that in order to form a eutectic mixture from a physical mixture of magnesium and aluminium, both of the metals have to first be allowed to mix as a liquid, which requires heating to 660°C (the melting point of Al).

The methods that have thus been reported requires in one way or another that heat is supplied at 650°C . From scalability and sustainability point of views, being able to lower this temperature without

sacrificing yield would have positive implications to this process. A wide range of silica has been used as feedstocks in the MgTR to produce porous silicon with no systematic study. In order to minimise the cost of production, the cheapest, most abundant feedstock should be used, however choosing a cheaper feedstock over a more costly one should not involve a compromise to the quality or yield of the silicon. It is clear that a quantitative comparison of various types of silica is needed in order to determine how different properties affect the MgTR reaction and change the silicon product. From this, the most desirable properties, and therefore the type of silica possessing these properties can be identified.

2.3.3. Techno-economic analysis of the MgTR

An economic analysis of the MgTR process is not available in the literature. It would, however, be crucial in determining the scalability using experimental results. In the interest of transferring research output to the industrial setting, the overarching objective of this project is to study the key parameters which govern the MgTR process by use the results to make technical improvements in favour of economic feasibility. This study is common in a design process, whereby an economic analysis is carried out on chosen designs to create a basis for optimisation⁵².

In terms of functional material produced, both quality and quantity matter – assuming a fixed yield of silicon, large amounts (quantity) of non-porous (quality) silicon will not be equal to the same amount of porous silicon. Since the application of this silicon is in energy storage it would be meaningful to calculate the cost of manufacture in terms of \$/kg of silicon. From this, the cost of energy stored, in terms of \$/mAh can be calculated by taking into consideration the amount of energy each kg of silicon can store, kg/mAh. The MgTR modelled as a scaled-up process will have to be evaluated based on the cost of making silicon and this will have to be compared with its current market value⁵³.

Although the literature specifically on the economics and scale-up of the MgTR process is lacking, the process can be split into common processes such as, mixing, heating, cooling and drying. In this way, the MgTR process can be modelled from fundamentals as a powder handling process⁵⁴. There are existing industrial processes which are analogous to the MgTR, such as silicothermic reduction

process (Pidgeon process)^{55,56}. In this process, Mg is produced from magnesium oxide, using silicon as the reductant. This process was invented in the 1940s and modern variations of this process have been developed, which are the Magnetherm⁵⁷ and Mintek⁵⁸. These processes are well studied, so where appropriate, data from these processes will be combined with fundamental design principles when building the model of the MgTR for the techno-economic analysis part of this project.

2.4. Silica types, properties and preparation

Silica is abundant in the earth's crust, mainly in the form of crystalline silicates such as quartz, cristobalite and tridymite²⁸. The chemical composition and crystal structures vary, depending on the geological source of silicate. There are different requirements for processing quartz to make suitable for different applications, with the overall aim of separating out impurities. The raw material is washed with water, crushed, then friction washed to remove any strongly adhering impurities. The quartz is then screened/sized, then treated with various acids depending on the grade required to remove any impurities incorporated into its crystal structure. Further purification can be achieved by treating the quartz with Cl₂ at high temperatures (1200°C). This process is called hot chlorination in which mineral impurities are drawn to the surface of the quartz to form chloride salts which can then be removed. An additional step to remove any metal oxide contaminants is magnetic and electrostatic separation. Purified quartz is then converted into various types of silica (Figure 2.9). The carbothermal reduction is carried out at high temperatures to produce metallurgical grade silicon and silicon carbide as a by-product. These products can be treated with chlorine gas to produce the volatile silicon tetrachloride, which is then burned in a hydrogen flame to produce fumed silica. These are made up primary particles between 5 and 40 nm, possessing SSAs around 300 m²/g for the smallest particles and 50 m²/g for the largest⁵⁹. For the semiconductor industry, the metallurgical grade silicon is purified and zone refined before going through the Czochralski process, where monocrystalline silicon boules are grown.

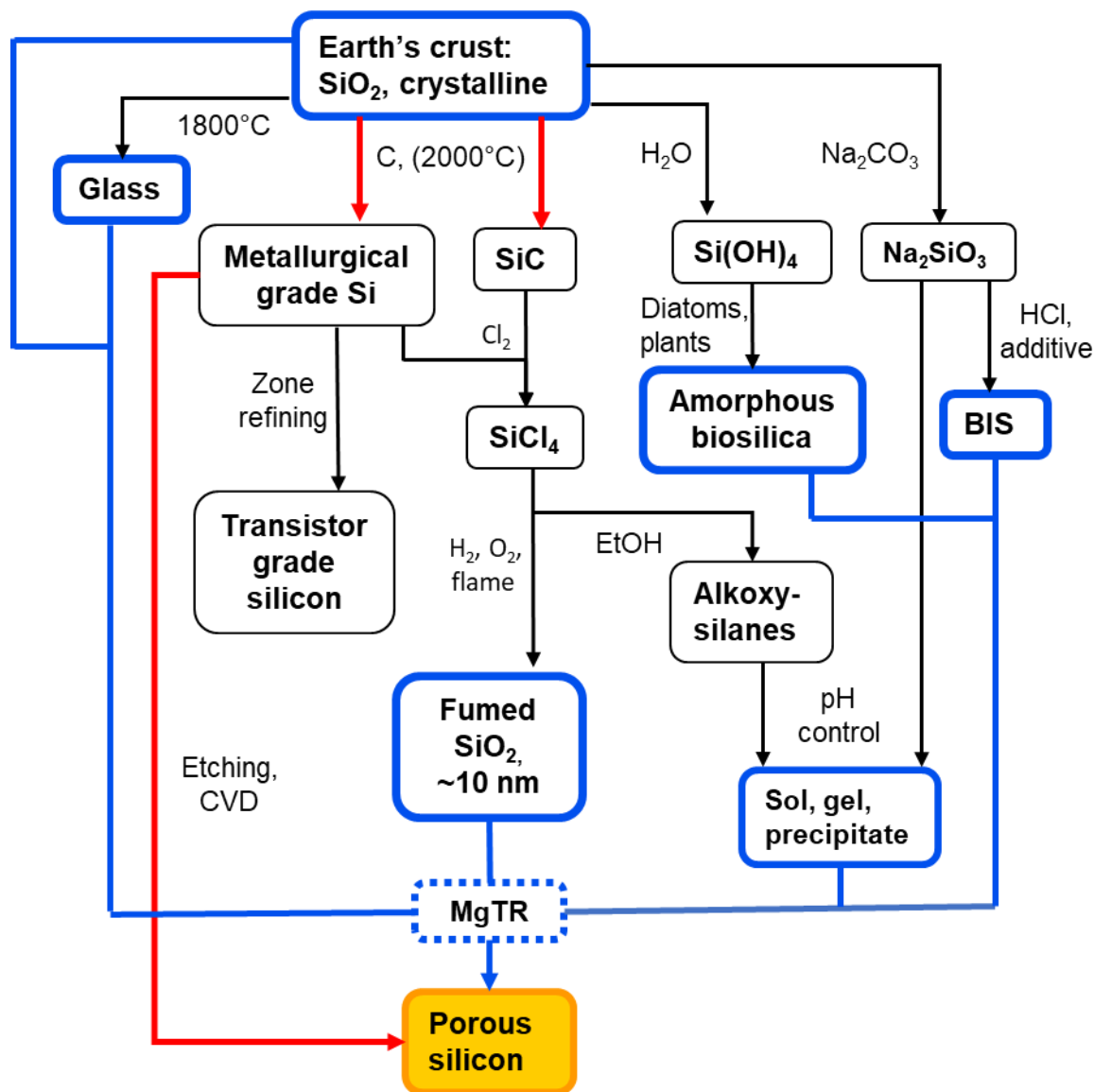


Figure 2.9: This schematic was constructed from information gathered from ^{65, 94, 95}. Red arrows show the current route taken to produce porous silicon, while blue arrows show the possible silica types that can be used to produce porous silicon via MgTR.

2.4.1. Silica sol, gel

Industrially, sodium silicate (Na_2SiO_3), formed by reacting silica quartz with sodium carbonate (Na_2CO_3), is the silica source used to form colloidal silica (silica sol). A sol is a liquid containing a stable suspension of silica particles which are small (<800 nm), and do not settle over time by gravity⁶⁰. Na_2SiO_3 is dissolved in water to form silicic acid ($\text{Si}(\text{OH})_4$), which undergoes a condensation-polymerisation reaction to form silica particles. At high pH (>9), the surfaces of silica particles in a sol are charged, repelling other particles and hence aggregation is suppressed⁶⁰. Particles in this environment grow individually to a stable size according to the pH of the solution. Smaller silica particles are more soluble than larger ones at high pH, so in highly basic environments newly formed silica particles dissolve and re-deposit themselves onto larger particles. This process is called Ostwald ripening, and gives rise to larger particles at high pH. If colloidal silica is formed in acidic conditions ($\text{pH} < 7$), the silica particles are uncharged, and so aggregate during growth. Unlike particles formed in basic conditions, these particles are not dispersed or uniformly sized, since growth and aggregation happens simultaneously. This results in the formation of a gel.

The IUPAC definition of a gel is a non-fluid polymer network that is expanded throughout its whole volume by a fluid⁶¹. Two interconnected phases exist within a gel - in a silica gel the polymer network is formed of $\text{Si}(\text{OH})_4$ monomers and the fluid is usually water, an alcohol, or a gas such as air. The method of removal of the fluid from the gel affects the final structure of the gel. When there is water or alcohol trapped within the gel network, the gel is known as a hydrogel or alcogel. Removal of the trapped solvent by evaporation leads to the collapse of pores by capillary action. This network of silica with collapsed pores is called a xerogel. The structure of the pores can be preserved if the solvent is supercritically dried, resulting in an aerogel, resulting in greater specific surface areas.

Silicon tetrachloride can be reacted with alcohols to form alkoxy silanes such as tetraethyl orthosilicate (TEOS), which is used to make silica via solution synthesis⁶⁰. TEOS dissolves in ethanol and is hydrolysed by water to form $\text{Si}(\text{OH})_4$. In the presence of a basic catalyst, such as ammonium hydroxide a condensation-polymerisation reaction occurs to form non-porous spherical particles of silica. This method of making silica is called the Stöber method and results in uniformly sized particles

within the range of 10 nm and 800 nm⁶². Their uniformity and ease of synthesis at the gram scale is the reason why Stöber particles have been widely used in the MgTR process^{63,64}. Using SEM, it is easy to track changes in the spherical structure under different conditions (temperature, ramp rate, dwell time). Wu *et al.* have shown that the reduction of Stöber silica at 700°C produces p-Si capable of storing a capacity of 1100 mAh/g after 100 cycles⁶³. This was due to the sintering of the silicon, creating an interconnected structure that was created as a result of etching away MgO and unreacted SiO₂. The SSA was not reported in this study. Wang *et al.* have shown that by addition of NaCl at the reduction stage, the excess heat can be absorbed, allowing the structure of the silica to be preserved during the reduction⁶⁴. Even though this reduction was carried out at 700°C the p-Si formed inherited the spherical structure, rather than forming a sintered interconnected structure. The silicon possessed a SSA of 214 m²/g and was able to store a capacity of 1500 mAh after 100 cycles.

Ordered structures of silica can be formed through a micelle templating method⁶⁵. Quarternary alkyl-ammonium surfactants form a micellar template, around which silicates can condense to form silica. By changing the length of the alkyl chain, micelles of different sizes could be formed, in this way, the pore diameters can be uniformly controlled. The surfactants can be removed by calcination. This is the basis of the formation of MCM-41, which is an ordered porous silica. The ordered structure results in a high SSA of ≥1000 m²/g, however, through the MgTR at 650°C, a lot of the surface area is lost, and the silicon product only possesses a SSA of ~150 m²/g, as demonstrated in a study by Shivaraju *et al.*⁶⁶ In another study, MCM-41 was reduced at 800°C, achieving p-Si with a SSA of 370 m²/g⁶⁷. It is important to note that the discrepancy could be due to the difference in reduction conditions but also that the preparation of p-Si in the work described in⁶⁶ used HF, while the work in⁶⁷ did not.

Stöber silica is considered non-porous, as each spherical particle does not possess pores while in contrast MCM-41 is highly porous due to the ordered, hollow structure. Using Stöber and MCM-41 as opposite extremes for comparison, it is clear that porous Si can be formed from either porous or non-porous SiO₂ via the MgTR.

2.4.2. Precipitated silica

Metal silicates are soluble in water and can be used to form silica particles upon the addition of acid. Initially a sol is formed, however if the final pH of the sol is low, then a gel is formed. At higher pH, due to the presence of metal ions, the surface charge of the particles are neutralised, eliminating repulsive forces and so a precipitate is formed, where the silica particles aggregate to form individual clusters throughout the sol, which can be separated by centrifugation. In the industrial setting, formation of precipitated silica tends to be on the order of hours and requires temperatures of around 60-80°C⁶⁸.

2.4.3. Bioinspired silica

A promising new method of synthesising silica draws inspiration from nature. Diatoms assimilate silica in the form of a hard exoskeleton, and through the study of the biological processes occurring within this organism, silica can be synthetically made in the lab at room temperature and neutral pH with reaction times in the order of minutes using sodium silicate⁶⁹. Silica made via this synthetic route is referred to as bioinspired silica. These “green” reaction conditions are made possible through the use of additives which catalyse and direct the formation of silica, increasing the rate of silica condensation and forming various morphologies mimicking biological organisms. The mild conditions (ambient temperature and pressure, neutral pH) required for the bioinspired synthesis allows enzymes and bacterial cells to be immobilised during the synthesis step without being denatured or destroyed, an advantage the method has over the traditional precipitated silica synthesis method. Although this method has many merits, the main caveat with the bioinspired synthesis route is the requirement of biological or synthetic additives to which a large proportion of the costs of scale up is attributed to⁷⁰. Should this type of silica be chosen as a feedstock for the MgTR then large quantities would be required, and cheaper additives would need to be found.

2.4.4. Natural and waste sources of silica

While synthetic silicas are commonly used as feedstock for the MgTR, it is important to consider natural as well as waste sources because of their low cost. This would not only benefit the economics of the process but would also help maintain feedstock flexibility of the MgTR (further discussion in Chapter 6 of this thesis). It was shown that quartz sand could be reduced into p-Si, giving a stable capacity of 1500 mAh/g after 100 cycles. The quartz sand was non-porous however, the p-Si after etching in HCl and HF had a SSA of 323 m²/g. Quartz has been shown to have a higher activation energy for the MgTR reaction than amorphous silicon due to its more stable crystalline structure⁷¹. While the successful reduction of sand into p-Si is promising, more work is needed in order to improve the conversion of this low-cost material into p-Si. Crushed glass bottles have been reduced to p-Si at 700°C by Li *et al.*³⁷, showing a high specific capacity of ~2500 mAh/g after 60 cycles. Rice husks have been reduced at 650°C, showing a high specific capacity of 1500 mAh/g after 300 cycles.

The use of the various forms of silica including low value, non-porous silica highlights the feedstock flexibility of the MgTR. High performance silicon can be made, capable of achieving capacities above 1000 mAh/g. With comparably lower temperature requirements the MgTR is a promising alternative to the carbothermal reduction (~650°C vs ~2000°C), however there are issues which need to be resolved in order for the process to be commercially viable. Firstly, the temperature requirement of ≥650°C still makes the process economically unfeasible (Chapter 6 of this thesis), however using a lower temperature is not straightforward as the yield decreases with temperature. Secondly, in the studies cited above, most, if not all of the work involve the use of HF to remove unreacted SiO₂. HF etching is highly hazardous and seriously impedes the scalability of any process. Therefore, it is important that while the temperature requirement is lowered, the yield is not hindered, so that the requirement of HF can be eliminated. To tackle these issues is the aim of the work presented in this thesis. It is also important that while improvements are being made to the process, the impact on the economics is evaluated.

2.5. Aims

The application for p-Si in lithium-ion batteries have been shown to be successful in the last two decades. To summarise, silicon forms an alloy with lithium and can achieve a maximum theoretical capacity of 3579 mAh/g when it undergoes this alloying reaction, however mechanical stresses associated the volumetric expansion of 280% causes rapid failure of the electrode. Multiple solutions have been successfully demonstrated to limit overcome this issue, and have been discussed in the literature review of this thesis:

1. Ordered silicon nanotubes grown on a substrate, improving conductivity and creating void space to allow for expansion
2. Elastic, self-healing binders capable of reversing mechanical fracture
3. Decreasing the size of Si to the nano regime, below the critical fracture size of 150 nm
4. Using amorphous Si as it expands isotropically, spreading mechanical stress over a larger area.

These solutions indicate that issues relating to the degradation of silicon anode have in principle been tackled however, other barriers still need to be removed so that the widespread use of Si in lithium-ion batteries can be realised.

Firstly, solution 1 above is difficult to implement at large scale because the fabrication of ordered nanotubes involves a surface technique, which is slow and costly. For silicon to be adopted in the market, not only does the performance need to be high, but a crucial factor that as to be accounted for is the economics. The material has to be cost-competitive, and a discussion of the techno-economics of the synthesis of Si is presented in Chapter 6 of this thesis. Solution 2 enables the use of larger (≥ 150 nm) silicon particles that are commercially available but fracture upon multiple charge-discharge cycles in a cell. This can be considered in future work whereby silicon with optimised morphologies can be mixed with elastic binders to help prevent mechanical fracture and further prolong lifetime. Solution 3 identifies a particle size limit below which fracture would not occur. The synthesis of silicon in bulk is a challenge, and surface techniques which are common and effective at the lab scale are not suitable for scale up. Therefore, this solution supports the need to for a bulk

process for manufacturing nano-sized silicon. Solution 4, like solution 1, and in some respects, solution 3, is also challenging to implement at large scales, due to the surface nature of their synthesis procedures.

The work in this thesis takes a process-level approach, using commercially available silicas such as Syloid and fumed silica, and therefore has large focus on the economics of the process. Stöber silica, though not commercially available in bulk, is used for proof of concept, and further investigations into the transferability of the concept uses Syloid and fumed silica.

p-Si can be made in bulk via a few existing processes however, these processes have not been developed beyond lab-scale. The primary objective driving every large-scale chemical process is economics. If the choice of silica were to be based on economics alone, as long as the quality and the value of the product remains the same, the cheaper feedstock will be chosen over a more expensive one. The quality of p-Si is based on its yield and properties, which in turn, are based on the effect of the chosen conditions on the kinetics and thermodynamics of the reaction. The MgTR, as with all solid-state reactions, is diffusion limited due to lack of mobility of SiO₂. It is well known in solid-state reactions that by decreasing reactant particle size, mass-transfer limitations can be minimised⁷². Changing the rate of mass transfer will affect local concentrations of reactants which in turn will affect the rates of competing reactions. At present, little is known about the way in which particle size of silica affects the MgTR reaction. A wide range of silica sources of different particle sizes have been used in the MgTR process to produce Si however, a systematic study of how silica particle size affects the reaction does not exist. An understanding of the effect of particle size on the reaction would better inform researchers in the field on the selection of feedstock based on their properties, or how to change the conditions to achieve desirable properties in the product silicon. Once the silica particle size has been investigated, the next step would be to carry out an economic analysis on the MgTR so that the impact of hypothetical improvements to the process can be quantified by energy and cost savings. The aims of this thesis can therefore be summarised:

1. Determine the effect of silica particle size on the process conditions and the properties of the product.
2. Apply the understanding from Aim 1 to come up with a novel, economically efficient method for reducing commercial silica into p-Si with high electrochemical performance
3. Assess the economics of method found in Aim 2 and compare with the baseline method and identify ways to make improvements to the process in favour of economics.

As part of the first aim, the extent to which particle size of SiO_2 affects the temperature requirement of the process will be determined. This will be carried out using spherical, monodisperse, non-porous silica, described in Chapter 4. The concepts found in Chapter 4 will be applied to modify the process so that commercially available silica can be converted into porous silicon at temperatures below 650°C , achieving the second aim. This study is laid out in Chapter 5, where electrochemical performance of the silicon produced is presented. The economics of the baseline, and low temperature process will be evaluated in a techno-economic analysis (TEA) of the process laid out in Chapter 6. TEA is to quantify the different operating costs of the process and to identify the most expensive steps, which will guide future research. In the final section of this thesis, "Conclusion and outlook", suggestion will be made on ways to further improve the economics of the process, beyond what is described in this thesis.

2.6. References

- 1 A. G. Morachevskii and A. I. Demidov, *Russian Journal of Applied Chemistry*, 2015, 88, 547–566.
- 2 M. T. McDowell, S. W. Lee, W. D. Nix and Y. Cui, *Advanced Materials*, 2013, 25, 4966–4985.
- 3 J. Li and J. R. Dahn, *Journal of The Electrochemical Society*, 2007, 154, A156.
- 4 M. N. Obrovac, L. Christensen, D. B. Le and J. R. Dahn, *Journal of The Electrochemical Society*, 2007, 154, A849.
- 5 L. Y. Beaulieu, K. W. Eberman, R. L. Turner, L. J. Krause and J. R. Dahna, *Electrochemical and Solid-State Letters*, 2001, 4, A137–A140.
- 6 R. A. Huggins and W. D. Nix, *Ionics (Kiel)*, 2000, 6, 57–63.
- 7 M. T. McDowell, I. Ryu, S. W. Lee, C. Wang, W. D. Nix and Y. Cui, *Advanced Materials*, 2012, 24, 6034–6041.
- 8 X. H. Liu, J. W. Wang, S. Huang, F. Fan, X. Huang, Y. Liu, S. Krylyuk, J. Yoo, S. A. Dayeh, A. V. Davydov, S. X. Mao, S. T. Picraux, S. Zhang, J. Li, T. Zhu and J. Y. Huang, *Nature Nanotechnology*, 2012, 7, 749–756.
- 9 M. T. McDowell, S. W. Lee, J. T. Harris, B. A. Korgel, C. Wang, W. D. Nix and Y. Cui, *Nano Letters*, 2013, 13, 758–764.
- 10 M. N. Obrovac and L. Christensen, *Electrochemical and Solid-State Letters*, 2004, 7, A93.
- 11 X. H. Liu, L. Zhong, S. Huang, S. X. Mao, T. Zhu and J. Y. Huang, *ACS Nano*, 2012, 6, 1522–1531.
- 12 S. Ohara, J. Suzuki, K. Sekine and T. Takamura, *Journal of Power Sources*, 2004, 136, 303–306.
- 13 C. K. Chan, H. Peng, G. Liu, K. McIlwrath, X. F. Zhang, R. A. Huggins and Y. Cui, *Nature Nanotechnology*, 2008, 3, 31–35.
- 14 M. Green, E. Fielder, B. Scrosati, M. Wachtler and J. Serra Moreno, *Electrochemical and Solid-State Letters*, 2003, 6, A75–A79.
- 15 T. Song, J. Xia, J. H. Lee, D. H. Lee, M. S. Kwon, J. M. Choi, J. Wu, S. K. Doo, H. Chang, W. Il Park, D. S. Zang, H. Kim, Y. Huang, K. C. Hwang, J. A. Rogers and U. Paik, *Nano Letters*, 2010, 10, 1710–1716.
- 16 C. Wang, H. Wu, Z. Chen, M. T. Mcdowell, Y. Cui and Z. Bao, *Nature Chemistry*, 2013, 5, 1042–1048.
- 17 W. Wang and S. Yang, *Journal of Alloys and Compounds*, 2017, 695, 3249–3255.
- 18 J. Guo, A. Sun, X. Chen, C. Wang and A. Manivannan, *Electrochimica Acta*, 2011, 56, 3981–3987.
- 19 H. Wu, G. Chan, J. W. Choi, I. Ryu, Y. Yao, M. T. Mcdowell, S. W. Lee, A. Jackson, Y. Yang, L. Hu and Y. Cui, *Nature Nanotechnology*, 2012, 7, 310–315.
- 20 J. H. Lee, H. M. Lee and S. Ahn, in *Journal of Power Sources*, 2003, vol. 119–121, pp. 833–837.

- 21 C. Shen, M. Ge, L. Luo, X. Fang, Y. Liu, A. Zhang, J. Rong, C. Wang and C. Zhou, *Scientific Reports*, 2016, 6, 1–11.
- 22 J. R. Szczech and S. Jin, *Energy and Environmental Science*, 2011, 4, 56–72.
- 23 C. H. Yim, F. M. Courtel and Y. Abu-Lebdeh, *Journal of Materials Chemistry A*, 2013, 1, 8234–8243.
- 24 H. Kim, M. Seo, M. H. Park and J. Cho, *Angewandte Chemie - International Edition*, 2010, 49, 2146–2149.
- 25 J. Song, S. Chen, M. Zhou, T. Xu, D. Lv, M. L. Gordin, T. Long, M. Melnyk and D. Wang, *Journal of Materials Chemistry A*, 2014, 2, 1257–1262.
- 26 S. M. Lu, *Renewable and Sustainable Energy Reviews*, 2016, 59, 1–12.
- 27 M. Javidani and D. Larouche, *International Materials Reviews*, 2014, 59, 132–158.
- 28 N. N. Greenwood and A. Earnshaw, *Chemistry of the Elements*, Butterworth-Heinemann, Oxford, 2012.
- 29 N. V. Nemchinova, V. A. Bychinskii, S. S. Bel'skii and V. E. Klets, *Russian Journal of Non-Ferrous Metals*, 2008, 49, 269–276.
- 30 C. H. Lewis, H. C. Kelly, M. B. Giusto and S. Johnson, *Journal of The Electrochemical Society*, 1961, 108, 1114.
- 31 G. Fisher, M. R. Seacrist and R. W. Standley, in *Proceedings of the IEEE*, 2012, vol. 100, pp. 1454–1474.
- 32 M. J. Sailor, *Porous Silicon in Practice: Preparation, Characterization and Applications*, Wiley-VCH, Weinheim, Germany, 2012.
- 33 K. Urmann, E. Tenenbaum, J. G. Walter and E. Segal, *Springer Series in Materials Science*, 2015, 220, 93–116.
- 34 J. W. Choi and D. Aurbach, *Nature Reviews Materials*, 2016, 1, 1–16.
- 35 C. Yuan, Y. Deng, T. Li and F. Yang, *CIRP Annals - Manufacturing Technology*, 2017, 66, 53–56.
- 36 N. Liu, K. Huo, M. T. McDowell, J. Zhao and Y. Cui, *Scientific Reports*, 2013, 3, 1–7.
- 37 C. Li, C. Liu, W. Wang, Z. Mutlu, J. Bell, K. Ahmed, R. Ye, M. Ozkan and C. S. Ozkan, *Scientific Reports*, 2017, 7, 1–11.
- 38 M. Hasegawa, in *Treatise on Process Metallurgy*, 2013, vol. 1, pp. 507–516.
- 39 J. Liang, X. Li, Z. Hou, W. Zhang, Y. Zhu and Y. Qian, *ACS Nano*, 2016, 10, 2295–2304.
- 40 N. Birks, G. H. Meier and F. S. Pettit, *Introduction to the High Temperature Oxidation of Metals*, Second Edition, 2006, 9780521480420, 1–338.
- 41 D. Cho, M. Kim, J. Hwang, J. H. Park, Y. L. Joo and Y. Jeong, *Nanoscale Research Letters*, 2015, 10, 1–8.
- 42 J. E. Entwistle, G. Beaucage and S. v. Patwardhan, *Journal of Materials Chemistry A*, 2020, 8, 4938–4949.

- 43 Z. Bao, M. R. Weatherspoon, S. Shian, Y. Cai, P. D. Graham, S. M. Allan, G. Ahmad, M. B. Dickerson, B. C. Church, Z. Kang, H. W. Abernathy, C. J. Summers, M. Liu and K. H. Sandhage, *Nature*, 2007, 446, 172–175.
- 44 W. Chen, Z. Fan, A. Dhanabalan, C. Chen and C. Wang, *Journal of The Electrochemical Society*, 2011, 158, A1055.
- 45 J. Ryu, T. Bok, S. Kim and S. Park, *ChemNanoMat*, 2018, 4, 319–337.
- 46 K. K. Larbi, M. Barati and A. McLean, *Canadian Metallurgical Quarterly*, 2011, 50, 341–349.
- 47 W. Luo, X. Wang, C. Meyers, N. Wannemacher, W. Sirisaksoontorn, M. M. Lerner and X. Ji, *Scientific Reports*, 2013, 3, 2222.
- 48 L. Khanna, Y. Lai and M. Dasog, *Canadian Journal of Chemistry*, 2018, 96, 965–968.
- 49 Z. Yang, Y. Du, G. Hou, Y. Ouyang, F. Ding and F. Yuan, *Electrochimica Acta*, 2020, 329, 135141.
- 50 S. A. Martell, Y. Lai, E. Traver, J. MacInnis, D. D. Richards, S. MacQuarrie and M. Dasog, *ACS Applied Nano Materials*, 2019, 2, 5713–5719.
- 51 Y. Lai, J. R. Thompson and M. Dasog, *Chemistry - A European Journal*, 2018, 24, 7913–7920.
- 52 R. K. Sinnott and G. Towler, *Chemical Engineering Design*, Elsevier Ltd, Oxford, Fifth Edit., 2009.
- 53 N. Lebedeva, F. Di Persio and L. Boon-Brett, *Lithium ion battery value chain and related opportunities for Europe*, 2016, vol. EUR 28534.
- 54 J. B. Butt, *Chemical Engineering Science*, 1960, 13, 93.
- 55 I. M. Morsi, K. A. El Barawy, M. B. Morsi and S. R. Abdel-Gawad, *Canadian Metallurgical Quarterly*, 2012, 41, 15–28.
- 56 S. N. Mathaudhu, A. A. Luo, N. R. Neelameggham, E. A. Nyberg and W. H. Sillekens, *Essential Readings in Magnesium Technology*, John Wiley & Sons Ltd, New Jersey, 2014.
- 57 C. Faure and J. Marchal, *Jom*, 1964, 16, 721–723.
- 58 M. Abdellatif, *J South Afr Inst Min Metall*, 2011, 111, 393–399.
- 59 O. W. Florke, H. A. Graetsch, F. Brunk, L. Benda, S. Paschen, H. E. Bergna, W. O. Roberts, W. A. Welsh, C. Libanati, M. Ettlinger, D. Kerner, M. Maier, W. Meon, R. Schmoll, H. Gies and D. Schiffmann, *Ullmann's Encyclopedia of Industrial Chemistry*, Wiley-VCH, Weinheim, Germany, 2012, vol. 32.
- 60 H.-P. Boehm, *Angewandte Chemie*, 1980, 92, 328–328.
- 61 J. Alemán, A. V. Chadwick, J. He, M. Hess, K. Horie, R. G. Jones, P. Kratochvíl, I. Meisel, I. Mita, G. Moad, S. Penczek and R. F. T. Stepto, *Pure and Applied Chemistry*, 2007, 79, 1801–1829.
- 62 W. Stöber, A. Fink and E. Bohn, *Journal of Colloid And Interface Science*, 1968, 26, 62–69.
- 63 H. Wu, N. Du, X. Shi and D. Yang, *Journal of Power Sources*, 2016, 331, 76–81.
- 64 W. Wang, Z. Favors, R. Ionescu, R. Ye, H. H. Bay, M. Ozkan and C. S. Ozkan, *Sci Rep*, 2015, 5, 1–6.

- 65 C. T. Kresge, M. E. Leonowicz, W. J. Roth, J. C. Vartuli and J. S. Beck, *Nature* 1992 359:6397, 1992, 359, 710–712.
- 66 G. C. Shivaraju, C. Sudakar and A. S. Prakash, *Electrochimica Acta*, 2019, 294, 357–364.
- 67 H. Sun, J. Chen, S. Liu, D. K. Agrawal, Y. Zhao, D. Wang and Z. Mao, *International Journal of Hydrogen Energy*, 2019, 44, 7216–7221.
- 68 S. V. Patwardhan, J. R. H. Manning and M. Chiacchia, *Current Opinion in Green and Sustainable Chemistry*, 2018, 12, 110–116.
- 69 S. V. Patwardhan, *Chemical Communications*, 2011, 47, 7567–7582.
- 70 C. Drummond, R. McCann and S. V. Patwardhan, *Chemical Engineering Journal*, 2014, 244, 483–492.
- 71 I. Gutman, L. Klinger, I. Gotman and M. Shapiro, *Scripta Materialia*, 2001, 45, 363–367.
- 72 S. E. Dann, *Reactions and Characterization of Solids*, Royal Society of Chemistry, Cambridge, 2000.

3. Materials and methods

3.1. Synthesis

3.1.1. Stöber synthesis

Silica nanospheres of various sizes were made via the Stöber method¹. Ethanol (Absolute, VWR) and TEOS (Sigma-Aldrich, $\geq 99.0\%$) were added to volumetric flask and mixed with a Teflon coated magnetic stirring bar. After 10 minutes of mixing, de-ionised water was added, and following 10 more minutes of mixing, ammonium hydroxide solution (VWR, 29%) was added dropwise to the solution. The amounts of ethanol and ammonium hydroxide were varied to achieve the desired concentration of ammonium hydroxide. The solution was stirred for a further 24 hours at 20°C, followed by centrifugation at 5000 rpm for 15 minutes to separate the particles from the solution. The particles were rinsed with deionised water (to remove excess ethanol, ammonium hydroxide and TEOS, then centrifuged once more at 5000 rpm for 15 minutes, before being dried overnight at 80°C. Smaller particles (≤ 20 nm) were separated using a dialysis membrane with a 14 kDA molecular weight cut-off, immersed in a de-ionised water bath. The conductivity (inverse resistance) of the water bath was measured at 4-hourly intervals using a multimeter on 2 M Ω resistance setting, and when two consecutive readings were the same, the water in the bath was removed and replenished with fresh de-ionised water to introduce a new diffusion gradient. This was repeated several times until the conductivity was unchanging, then the particles within the dialysis membrane were separated by drying on an evaporating dish.

3.1.2. Bio-inspired silica synthesis

31.82 g of sodium metasilicate (Sigma Aldrich) was dissolved in 4650 mL of de-ionised water at 25°C in a 5L agitated Radley Reactor. 5.81 g of pentaethylene hexamine (PEHA) (Sigma Aldrich) was then added to the reactor and allowed to dissolve completely. At this point, the pH was recorded, and then continuously monitored. 350 mL of 1M HCl (Sigma Aldrich) was added to the reactor, then additional HCl was added using a micropipette to bring the solution down to pH 7 ± 0.05 within 5 minutes. The

silica precipitate was then promptly filtered using a cellulose filter paper. The filter cake was rinsed multiple times with de-ionised water, then collected and dried in a drying oven at 80°C. The dried silica was crushed into a powder using a mortar and pestle then calcined in a furnace at 500°C for 5 hours to remove the PEHA.

3.1.3. Magnesiothermic reduction

The general procedure for carrying out the magnesiothermic reduction is described in this section. Modifications made to the procedure are further described in relevant sections of this thesis. Silica powders were ground with magnesium powder in an agate mortar and pestle at various weight ratios then placed in a stainless steel or alumina crucible and covered with a loose lid (Figure 3.1). The crucible was placed in a tube furnace at room temperature, then the furnace was hermetically sealed. Argon gas flowing through the tube furnace was set to a flow rate of 125 mL/min throughout the time the sample remained in the furnace. The furnace was held at room temperature before heating to purge oxygen from within the furnace. Typically, 0.5 g of Mg (Alfa Aesar, 99.8%) would be grinded with 0.5 g of silica powder. This mixture has a molar excess of magnesium (2.5:1 mole ratio). The basic heat treatment programme included ramping the furnace temperature at a rate of 1°C/min to 650°C, then dwelling at this temperature for 6 hours. The furnace and its contents were allowed to cool naturally to room temperature, still under flowing argon. Once the crucible was removed from the furnace, the reaction mixture was then added to 1M aqueous HCl and stirred with a magnetic stirrer at 200 rpm, at room temperature for 24 hours to dissolve Mg, Mg₂Si and MgO. Following this, the solution was filtered using cellulose filter paper and a Büchner flask under an active vacuum to separate the undissolved solids – a mixture of Si and unreacted SiO₂. The wet cake was dried in a drying oven at 80°C, then stored in a vacuum oven at 120°C.



Figure 3.1: A) Magnesium and silica powders in an agate mortar. Stainless steel crucible containing B) magnesium and silica before heating, and C) after heat treatment. D) Sample in 1M HCl after heat treatment.

3.2. Analytical techniques

3.2.1. Scanning electron microscopy (SEM)

3.2.1.1. Theory

Scanning electron microscopy (SEM) is used to gain information about the physical structure of a material. SEM can achieve magnifications up to 100,000x, and provide a 3D topographical image of a sample due to its depth of focus. In an electron microscope, electrons are accelerated by an electron gun at a target sample at accelerating voltages between 5-50 keV. The electron beam is focused by passing through magnetic condenser lenses, before colliding with the sample. Upon collision, the electrons are scattered by the sample elastically or inelastically. In inelastic scattering, the sample absorbs most of the energy from the incident electron and emits a secondary electron, along with radiation. In elastic scattering, electrons retain most of its incident energy and its scattered trajectory is different from its initial trajectory, becoming back scattered electrons. The secondary and back-scattered electrons then hit a detector which consists of semiconductors. These semiconductors generate currents when excited by electrons, which are then converted into an image. The electron beams typically have a penetration depth of 1 μm , so this technique relies on the reflection of electrons from the surface, therefore information only of the surface of a sample can be obtained. This is in contrast to transmission electron microscopy, where electrons are transmitted through a sample, and

deeper morphological information can be obtained. Length scales around 20 nm can be distinguished using SEM. Figure 3.2 shows the working principle of a scanning electron microscope.

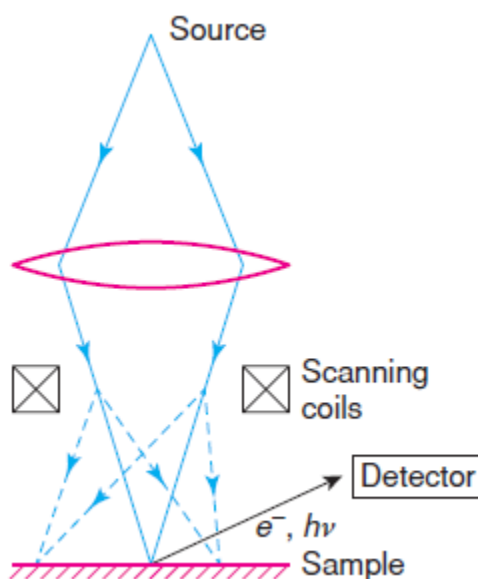


Figure 3.2: Diagrammatic representation of the working principle of a scanning electron microscope. Image source:².

3.2.1.2. Procedure

Dry powder samples are dispersed in absolute ethanol and sonicated for 10 minutes before being drop casted onto carbon coated aluminium stickers. Samples were coated in gold using a sputter coater. Scanning electron microscopy (SEM) images were taken at different magnifications using a FEI Inspect F scanning electron microscope with an accelerating voltage of 5 keV. Image J software was used for image analysis. SEM images of silica and reduced silica will be taken to determine its morphological structure, particle size, and degree of sintering. This will be particularly useful for Chapters 4 and 5 where the effect of particle size of silica on the conditions of the reduction reaction is investigated.

3.2.2. Transmission electron microscopy (TEM)

3.2.2.1. Theory

In transmission electron microscopy (TEM) an image is created by electrons which transmit through a sample, as oppose to reflecting off a sample. Similarly to SEM, a beam of electrons is focussed onto a target sample and scattered by the sample. Electrons which transmit through the sample are magnified through projector lenses and focussed onto a fluorescent screen. When electrons hit the fluorescent screen, light is generated creating an image of the sample. TEM provides morphological information about the sample bulk as opposed to just the surface. TEM can be used to resolve length scales smaller than the limits of SEM due to the higher accelerating voltage of the electrons. TEM is used to image particles too small to be resolved by SEM (≤ 20 nm), and to confirm the presence of internal porosity in reduced Stöber silicas in Chapter 4 and 5.

3.2.2.2. Procedure

Samples were dispersed in ethanol by ultrasonication then drop-casted onto 400 mesh copper TEM grids coated with lacey carbon films (Agar Scientific). TEM images were analysed using Image J software. All TEM images presented in this work were collected by Dr. Colm O'Regan using a Jeol R005 80-300kV transmission electron microscope.

3.2.3. Powder X-ray diffraction (XRD)

3.2.3.1. Theory

X-rays are a type of electromagnetic radiation with wavelengths on the order of 1-10 angstroms. X-rays are therefore able to interact with matter at the atomic scale, providing useful information on crystal structures and arrangements³. When electrons are rapidly decelerated by a magnetic field or by collision with a metal electrode, X-rays of varying wavelengths and intensities are produced. The wavelength of each photon of X-ray depends on the energy lost by the electron during deceleration to produce it. Since electrons can lose energy in either a single collision or multiple collisions, the X-rays produced form a continuous spectrum between short and long wavelengths. If the accelerating voltage exceeds a certain cut-off voltage whereby the electrons collide with the target material with enough energy to eject its K-shell electrons, a vacancy is created in the K-shell. An electron jumps from an outer shell to fill the vacancy in the inner K-shell, producing high intensity X-rays with characteristic wavelengths corresponding to the energy released from this jump. These characteristic wavelengths are specific to the target material. It is far more likely that an electron from an L-shell will jump to fill the K-shell vacancy, and the X-rays released from this jump are called the K_{α} radiation. A less probable event can occur where an outer M-shell electron will jump to the K-shell, and the produced X-rays with this characteristic wavelength are called K_{β} radiation. As a result, the intensity of K_{α} radiation is around 10 times higher than K_{β} radiation. The K_{α} peak is made up of doublet peaks, with the $K_{\alpha 1}$ peak having an intensity twice that of the $K_{\alpha 2}$ peak. The weighted average of the peaks is used since the wavelengths of the two are very close. For the purpose of X-ray diffraction, a monochromatic beam of X-rays is required, and the K_{α} peak is used since it is the most intense. A filter is used to absorb K_{β} radiation, so majority of the X-rays produced have wavelengths corresponding to K_{α} radiation, with very small amounts of K_{β} radiation. The resulting filtered beam of X-rays are then collimated and directed at a sample for X-ray diffraction.

An X-ray diffraction laboratory setup consists of an evacuated tube to which a large negative potential (~30kV) is applied, with respect to the anode. Electrons are accelerated from the cathode to the

anode. From equation [1], the higher the atomic number (Z), and the voltage (V), the greater the intensity of X-rays produced:

$$I = AiZV^m \quad \text{Equation 1}$$

I is the total intensity of the X-rays produced, A is a proportionality constant, and i is the tube current. Hence, atomic number and voltage provides two of the criteria for choice of metal to use as an anode target in diffraction work.

X-rays are scattered when they collide with atoms in their path of propagation. When multiple rays propagating parallel to each other collide with a plane regularly spaced atoms in a crystal, the diffracted rays can interfere destructively or constructively depending on whether their relative phase. If they are in phase, or out of phase by whole integers of their wavelengths, they interfere constructively, and their amplitudes add. The criteria for constructive interference to occur is dependent on the spacing between the atoms in the crystal (d), the angle at which the rays collide with the plane atoms (θ), and the wavelength of the X-rays (λ), as given by the Bragg equation⁴

$$n\lambda = 2d\sin(\theta)$$

n is an integer which is referred to as the order of reflection of the planes and gives the limitation that constructive interference can only occur between rays with path lengths differing by whole wavelengths. This is demonstrated in Figure 3.3, whereby the diffracted beams 1' and 2' are in phase due to the spacing between atoms P and Q being a whole wavelength apart.

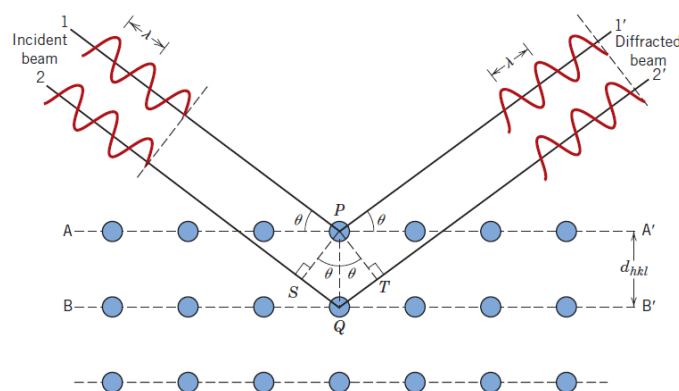


Figure 3.3: Schematic showing constructive interference between two rays 1' and 2', being diffracted from crystal planes spaced whole wavelengths apart. Image source:⁵.

Given that crystal planes are spaced on the order of 3\AA , and that $\sin(\theta)$ has a magnitude no greater than 1, λ cannot be greater than 6\AA , which sets another criterion for the choice of anode target for diffraction work. K_{α} radiation cannot be greater than 6\AA , or too small ($<1\text{\AA}$), which makes diffraction angles difficult to measure. A few common transition metals, chromium, cobalt, molybdenum, and silver are therefore used in laboratory diffractometers with the most commonly used being copper, with a $K_{\alpha 1}$ wavelength of 1.5406\AA . Using X-ray diffraction (XRD), information about a crystalline sample's d-spacing can be obtained, which can be used to identify or confirm the presence of the material.

3.2.3.2. Procedure

The work reported in this thesis was centred upon synthesising crystalline silicon (c-Si), hence XRD was used to confirm the presence of c-Si in heat treated and acid etched samples. This was done by matching peaks obtained from XRD to peaks from a known standard of c-Si. The specific technique used was powder X-ray diffraction (pXRD). After being dried in a vacuum oven at 80°C for at least 24 hours, samples were ground into a fine powder using an agate mortar and pestle. pXRD was performed using the Stoe Stadi P (CuLP) diffractometer. 5 diffractograms were collected for each sample within the 2θ range of 1 and 120° , each taking 6 minutes. The diffractograms were combined using the WinXPow software to produce a single, averaged diffractogram for each sample.

3.2.4. Thermal gravimetric analysis (TGA)

3.2.4.1. Theory

The weight of a sample changes when heated, due to various processes such as moisture loss, decomposition or oxidation. Thermal gravimetric analysis (TGA) is a technique used to measure this change in weight as a function of temperature and time. A sample of known mass is placed in a crucible, with a perforated lid to allow movement of vapour and gases. The change of mass of the sample is determined and recorded using a microbalance. The thermal gravimetric analyser contains a microbalance, onto which the crucible is placed. The analyser heats the sample according to a pre-programmed heating profile and records the mass at set time intervals. An inert or oxidising atmosphere can be used. The change in mass can then be used to determine various properties of the sample. If a metal powder is heated under an oxidising atmosphere, the mass of the sample will increase as it oxidises. The total mass gained at the end of the heating profile can be used to determine the purity of the original metal powder, and it is this principle that will be used for the measurement of yield in this work.

3.2.4.2. Procedure

Samples were first dried in a vacuum oven at 120°C for at least 24 hours before placing thermal gravimetric analysis. Automated TGA was performed using a Perkin Elmer TGA 4000. Manual TGA was also performed, and the results were compared with automatic TGA to confirm the validity of the manual method. The manual method is as follows. A clean crucible with a perforated lid was weighed on a microbalance. A small amount (5-10 mg) of sample to be analysed was placed in the crucible. The crucible, now filled with the sample was weighed in order to determine the mass of the sample. The crucible was then placed in a furnace which heats the sample according to a programmed heating profile. The temperature was ramped up to 1000°C at a rate of 10°C/min. The sample was held at this temperature for 16 hours to ensure complete oxidation of the elemental Si present before being cooled naturally to room temperature. The crucible was then weighed using a microbalance and the

difference in mass before and after heating was calculated. The procedure described was the same for automated TGA, without the need of manually recording the sample.

TGA was performed on samples which were acid etched and dried at in a vacuum oven at 120°C for at least 24 hours. At this point, only silicon and silicon dioxide remained. TGA was used to determine the amount of Si as a percentage of the total moles of Si, elemental and oxidised in the sample. This was the yield of the sample, and was calculated from the mass change using the following equations

$$\text{mass of } O_2 \text{ gained (g)} = \text{oxidised mass(g)} - \text{preoxidised mass(g)}$$

$$\text{moles of } O_2 \text{ gained} = \frac{\text{mass of } O_2}{\text{molar mass of } O_2}$$

Given that Si reacts with O_2 at a 1:1 ratio, the number of moles of Si is equal to the moles of O_2 gained. From this the mass of elemental Si that was present in the sample before oxidation was calculated by:

$$\text{mass of Si} = \text{moles of Si} \times \text{molar mass of Si}$$

The mass of SiO_2 was then found by subtracting the mass of Si originally in the sample by the pre-oxidised mass. Dividing by the molar mass of SiO_2 gave the number of moles of SiO_2 in the pre-oxidised sample. Finally, the yield was calculated by:

$$\text{yield (mol\%)} = \frac{\text{moles of Si} \times 100}{\text{moles of Si} + \text{moles of } SiO_2}$$

3.2.5. Surface area and pore analysis

3.2.5.1. Theory

Surface area and pore size of a material is important as it relates to the material's performance in an application. The surface area of a material can be measured in a laboratory using the gas physisorption phenomenon. Gases can interact with a solid surface by adsorbing onto it through a condensation process. The amount of gas that is adsorbed onto a surface is a function of the pressure of the non-adsorbed (adsorbent) gas above the surface, and the exposed area of the surface. If the amount of gas adsorbed is known, through accurate and sensitive pressure measurements, along with the cross-sectional area of each gas molecule, then the surface area can be calculated. This is the basis of vacuum volumetric measurements⁶. The major assumption here is that when gases adsorb onto a solid surface, the surface will be covered with only a monolayer of gas. In reality, multilayer adsorption will occur before completion of the first monolayer and therefore there is no pressure or pressure range whereby only a single complete monolayer exists.

High energy (adsorption potential) sites on a solid surface will exist in many materials, such as within micropores (<2 nm) and adsorption will preferentially occur at these sites. As the inner walls of mesopores achieve monolayer coverage, the empty, unfilled space in the pore is now narrower, and becomes a high energy site, so adsorbents will also preferentially adsorb at these sites over open, flat sites. This behaviour of gases adsorbing onto solid surfaces gives rise to common isotherms which are defined by IUPAC⁷ and shown in Figure 3.4 below.

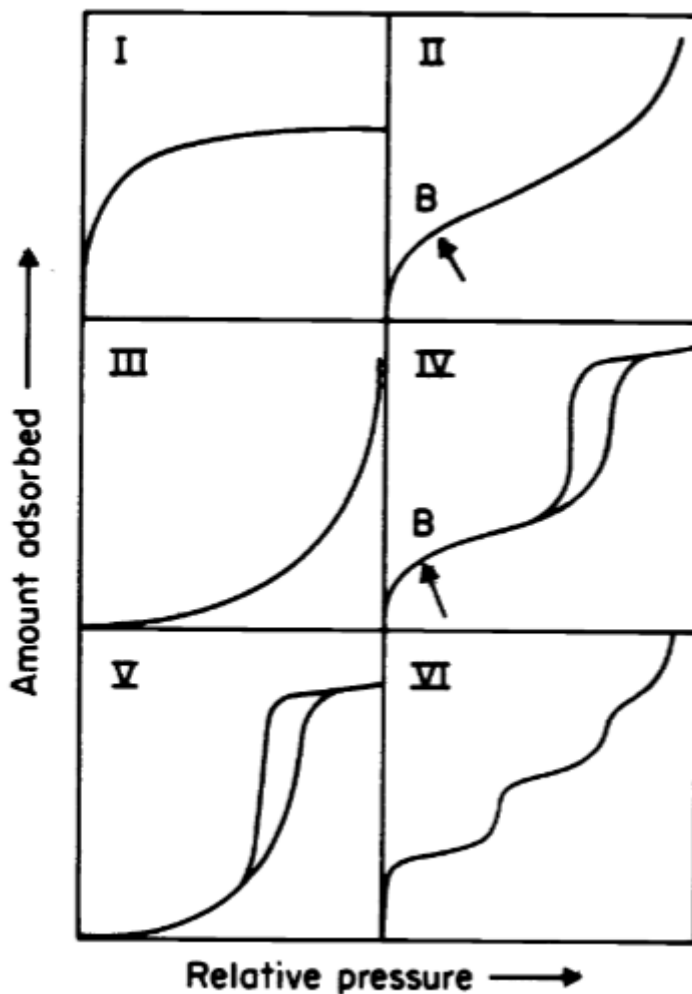


Figure 3.4: Characteristic adsorption isotherms assigned Types 1 – 4 by IUPAC. Image taken from:⁷.

Type 1 isotherms indicate the presence of micropores and very little external surface areas. Micropores are filled first, hence a large amount of gas can be adsorbed at very low pressures. Once the micropores have been filled, the amount of gas that can be adsorbed is asymptotic at higher pressures due to limited external surface areas.

Type 2 isotherms indicate a non-porous or macroporous material. The point at which monolayer coverage is achieved is indicated by the inflexion at point B although it is accepted that multi-layer adsorption occurs before this.

Type 3 isotherms are characteristic of non-porous materials. Pore-filling does not occur, hence no inflexion point is seen in the isotherm.

Mesoporous materials exhibit Type 4 isotherms in gas adsorption measurements. At low relative pressures, Type 4 isotherms have the same trend as type 2 isotherms whereby the completion of a monolayer is indicated by a point of inflexion. However, at higher pressures, adsorbent molecules condense within the pores due to pore narrowing from the monolayer of gas. This is indicated by a sharp increase in amount of gas adsorbed. A hysteresis is seen on the desorption branch, and this is due to the difference in the pore filling and emptying behaviour (Figure 3.5)⁶.

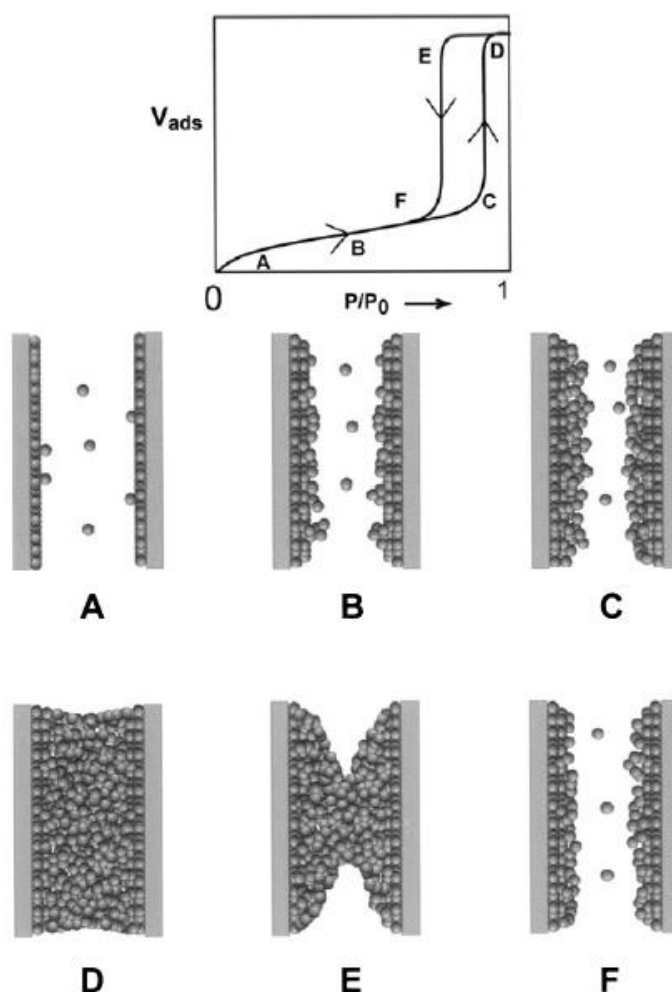


Figure 3.5: Mesopore filling and emptying during adsorption (A – C) and desorption (D – F) respectively, giving rise to isotherm hysteresis. Image source: ⁶.

Type 5 isotherms initially follow type 3 isotherms at low pressures, indicating weak interactions between adsorbent and adsorbate, and hence, lack of a pronounced inflexion point. At higher pressures, hysteresis is seen due to the pore condensation as described in Figure 3.5.

Type 6 isotherms are seen in uniform, spherical non-porous surfaces, where steps in the isotherm indicate multi-layer adsorption.

From the isotherms, information on the surface area can be gained using the relation between the amount of gas adsorbed at different partial pressures, originally described by Brunauer, Emmett and Teller (BET). The BET equation is as follows:

$$\frac{1}{W \left(\frac{P}{P_0} - 1 \right)} = \frac{1}{W_m C} + \frac{C - 1}{W_m C} \left(\frac{P}{P_0} \right)$$

Where C is a factor which takes into account the energy of adsorption, the vibrational frequency of the adsorbate and a condensation coefficient. W is the weight of gas adsorbed, W_m the weight of gas adsorbed in the monolayer. P is the pressure at which the measurement is being taken, and P_0 is the saturation pressure, making P/P_0 the relative pressure.

Plotting the BET equation as a straight line allows for C and W_m to be determined from the slope and intercept respectively. Information about the pore size can be determined from gas adsorption measurements and using the Barrett-Joyner-Halenda method (BJH). The BJH method for pore analysis has its roots in the Modified Kelvin Equation:

$$\ln \left(\frac{P}{P_0} \right) = \frac{-2\gamma V}{rRT}$$

V represents the molar volume of the adsorbed liquid, γ the surface tension of the adsorbate, r the radius of the pore and R and T are the gas constant and temperatures respectively.

3.2.5.2. Procedure

Gas adsorption is carried out at the boiling point of the adsorbed gas. Nitrogen gas is accepted as the arbitrary adsorptive standard due to its small molecular cross-sectional area of 16.2 Å, which allows it to penetrate micropores, and wide availability of liquid nitrogen. Samples were in the form of a powder and are first dried in a degasser at 120°C under vacuum for a minimum of 24 hours. Gas adsorption was carried out using a Micromeritics Tristar 3000. The samples were then placed in a

sample tube which was immersed into a dewar containing liquid nitrogen. The programme was set to measure void space of the tube was measured using helium prior to adsorption measurements. Measurements were carried out between the P/P_0 range of 0.01 and 0.99.

3.2.6. Electrochemical testing

An electrochemical cell consists primarily of an anode, a cathode, electrolyte and a separator. Additionally, for a lithium-ion cell, a hermetically sealed casing is required to prevent exposure of cell contents to oxygen and moisture. Various cell architectures (cylindrical, prismatic, and pouch) are available for real world applications (Figure 3.6)⁸.

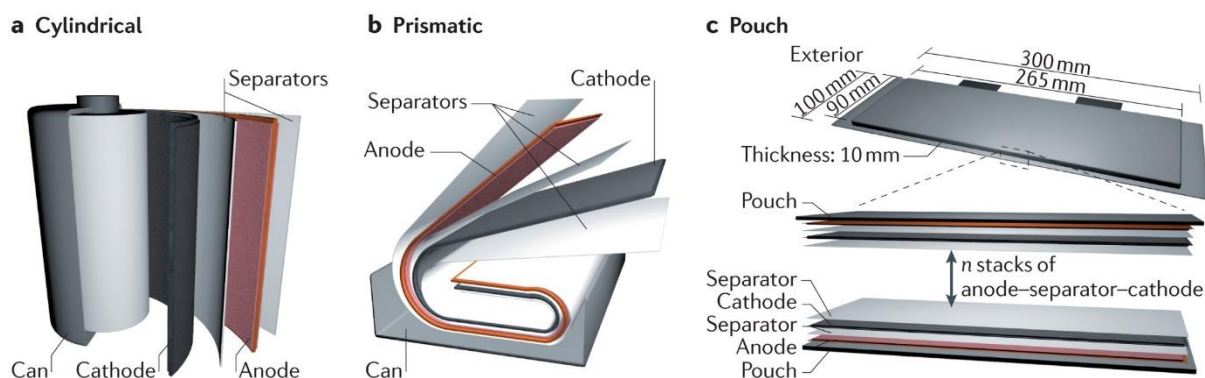


Figure 3.6: Cylindrical, prismatic and pouch cell architectures are designed for different real-world applications. These cells can be combined to form battery packs with higher voltage and current capabilities. Image source:⁸

These involve sophisticated assembly equipment and processes and require large amounts of active material (~10 – 100g) and electrolyte to achieve capacities that are suitable for their assigned application. For laboratory experiments, small amounts (~100 mg) of active material are synthesised and tested at a time, hence cylindrical, prismatic and pouch cells are not suitable for lab-scale material testing. Additionally, given that the performance of new materials synthesised in the lab can be unpredictable or fail completely, testing a large number of materials in these cell architectures is wasteful and costly. Instead, a more suitable architecture, the coin cell, is used. In this type of cell, less than 10 mg of active material is required for electrochemical testing. Coin cells are simple to assemble, and assembly can be done with a high success rate in a laboratory equipped for electrode

material research. The most common types of coin cells are 2016, and 2032, where the diameter of the cells are both 20mm, and the thicknesses of the cells are 1.6 or 3.2 mm respectively.

The components that make up a 2016 coin cell is shown in Figure 3.7. The coin cell consists of a stainless-steel (SS) casing, which, when crimped, acts as a sturdy and robust housing, preventing the movement of material in and out of the cell during electrochemical testing. For this work, copper foil was used as the current collector due to the voltage window (0.001 – 1.2V) within which materials were tested. The active material is coated on the copper foil, on the side facing the separator. Lithium foil is commonly used in laboratory cell testing, to provide an excess amount of lithium. Depending on the thickness of the electrode coating and the lithium foil, a SS spacer is used to ensure good physical contact between the electrodes and the casing.

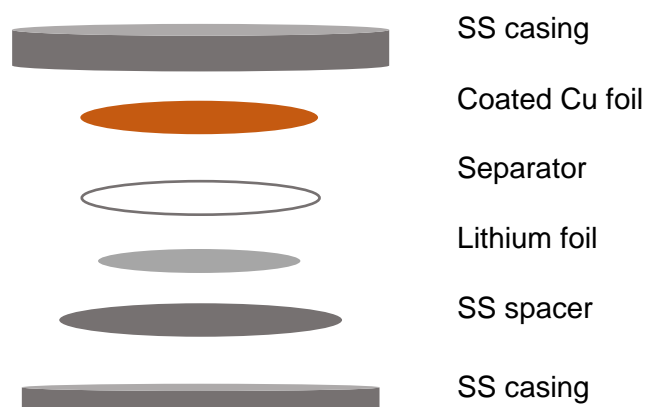


Figure 3.7: Schematic of a lithium-ion coin cell assembly.

3.2.6.1. Procedure

The electrode material synthesised in this work was in powder form. In order to make good contact with a current collector (copper foil), a water-based slurry was prepared, consisting of a binder and conductive carbon. To prepare the slurry, 0.05 g of CMC was first added to 2 mL of water in a PTFE container, then mixed in a Thinky ARE-250 mixer for 30 minutes to create a viscous, homogeneous mixture. Then, 0.05 g of C65 carbon was added to the mixture and mixed for a further 10 minutes. Finally, 0.15 g of synthesised silicon was added and mixed for a further 10 minutes. The slurry was

drop-casted onto a 10 μm thick copper foil using a doctor blade set to 300 μm . The coated foil was left to dry for 30 minutes under ambient conditions, then stored in a vacuum oven at 80°C overnight.

10 mm diameter electrodes were punched from the coated foil and each was weighed using a microbalance. The electrodes were then assembled into a coin cell in a glovebox as depicted in Figure 3.7 above, using a cell crimper. The separator used was Whatman GF/A glass fibre. The SS spacers were 5 mm thick, and the lithium foil was 9 mm in diameter and 38 μm thick.

Cells were put through an open circuit 'rest' step for 8 hours before constant current cycling. Galvanostatic cycling was performed on the cells between 0.01 and 1.2 V vs. Li at a C-rate of 0.1C for 100 charge and discharge cycles. The capacity was calculated based on the weight of active material, which was then used to set the current to match a C-rate of 0.1C.

3.3. References

- 1 W. Stöber, A. Fink and E. Bohn, *Journal of Colloid And Interface Science*, 1968, **26**, 62–69.
- 2 A. West, *WILEY*, 2014, 584.
- 3 B. D. Cullity, *Elements of X-ray Diffraction*, Addison-Wesley, 2nd Edition., 1957.
- 4 C. G. Pope, *J Chem Educ*, 1997, **74**, 129.
- 5 W. D. Callister and D. G. Rethwisch, *Fundamentals of Materials Science and Engineering: SI version*, John Wiley & Sons, 9th Edition., 2014.
- 6 S. Lowell, J. E. Shields, Martin. A. Thomas and M. Thommes, *Characterization of Porous Solids and Powders: Surface Area, Pore Size and Density*, Springer, 2004.
- 7 M. Thommes, K. Kaneko, A. v. Neimark, J. P. Olivier, F. Rodriguez-Reinoso, J. Rouquerol and K. S. W. Sing, *Pure and Applied Chemistry*, 2015, **87**, 1051–1069.
- 8 J. W. Choi and D. Aurbach, *Nature Reviews Materials*, 2016, **1**, 1–16.

4. Exploiting nanoscale effects enables ultra-low temperature to produce porous silicon

Royal Society of Chemistry Advances
Volume 11, Issue 56
October 2021
Doi: 10.1039/d1ra07212a

*Maximilian Yan and Siddharth V. Patwardhan**

Department of Chemical and Biological Engineering, Green Nanomaterials Research Group, The University of Sheffield, Mappin Street, Sheffield S1 3JD, UK. [*s.patwardhan@sheffield.ac.uk](mailto:s.patwardhan@sheffield.ac.uk)

Received: 27th September 2021

Accepted: 21st October 2021

Published: 1st November 2021

4.1. Contribution

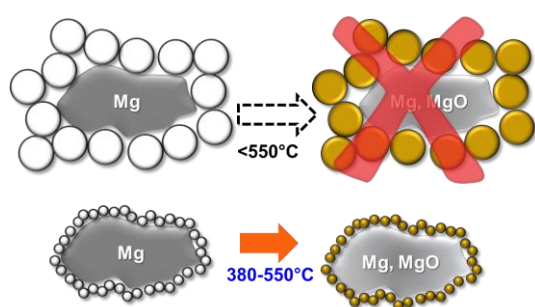
I performed the majority of the experimental work in this paper. TEM was performed by Dr. Colm O'Regan, of the Sorby Centre for Electron Microscopy. I also prepared the manuscript draft. SVP contributed to the project supervision, experimental design and editing of the manuscript.

Exploiting nanoscale effects enables ultra-low temperature to produce porous silicon

*Maximilian Yan and Siddharth V. Patwardhan**

Department of Chemical and Biological Engineering, Green Nanomaterials Research Group, The University of Sheffield, Mappin Street, Sheffield S1 3JD, UK. [*s.patwardhan@sheffield.ac.uk](mailto:s.patwardhan@sheffield.ac.uk)

4.2. Graphical Abstract



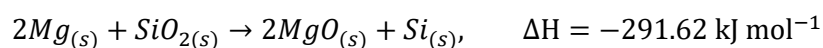
We show the first evidence of reduction of silica occurring at temperatures as low as 380°C to produce porous silicon without sacrificing the porosity and yield, thus paving the way for sustainable manufacturing.

4.3. Abstract

The magnesiothermic reduction (MgTR) of silica has been recently shown to produce porous silicon which can be used in applications such as photocatalysis and energy storage. MgTR typically requires $\geq 650^{\circ}\text{C}$ to achieve meaningful conversions. However high temperatures are detrimental to the highly desired porosity of silicon, while also raising doubts over the sustainability of the process. In this work we show for the first time that the onset temperature of the MgTR is dependent on particle size of the feedstock silica. Using both in-house synthesised and commercial silica, we have shown that only particles ≤ 20 nm are able to trigger the reaction at temperature as low as 380°C, well below a cut-off temperature of 500°C, producing porous, crystalline silicon. The decrease in temperature requirement from $\geq 650^{\circ}\text{C}$ to 380°C achieved with little modification to the overall process, without any additional

downstream processing, represents significant implications for sustainable and economical manufacturing of porous silicon.

Porous silicon is a material which is heavily studied due to its structural and electronic properties, which lends itself well to applications such as photocatalytic water splitting,¹ photoluminescence,² and energy storage.³ However, for this material to become commercially accessible, a method of sustainably producing high quality silicon on a large scale is needed. It has recently been shown that the magnesiothermic reduction (MgTR) as a bulk method of producing porous silicon has a great potential for scaling up, especially when compared to the carbothermal⁴ and electrochemical etching methods.⁵ The MgTR is a reaction in which powdered Mg, the reducing agent, is mixed with powdered silica and heated in a furnace under argon atmosphere. The reaction mixture is typically heated to 650°C, and proceeds as shown in Equation 1:



The mixture, once removed from the furnace, is then immersed in HCl to remove any magnesium species. It was shown that higher reduction temperatures ($\geq 650^\circ\text{C}$) favour reaction completion,⁶ however higher temperatures are detrimental for the desired porosity caused by sintering of nanocrystals. Below 650°C, the yield begins to drop, until a cut-off temperature of 500°C is reached, below which the reaction cannot proceed. Eutectic mixtures containing magnesium and Al have been shown to trigger the MgTR as low as 450°C to produce a yield of silicon of 64 mol%.⁷ The drawback is that to form the eutectic, the metals have to be heated to 660°C initially, which is the melting point of aluminium. Alternatively, a two-step reduction method has been demonstrated whereby the MgTR can progress at 300°C, however this method requires the reactants to be heated initially to 650°C to trigger the reaction.⁸

In addition to the need for carrying out MgTR at lower temperatures to maintain porosity, from scalability and sustainability perspectives, being able to lower the temperature requirement without sacrificing the porosity and most importantly, yield, would have positive implications to this process. Herein, for the first time, we demonstrate a method of achieving the MgTR reaction at low temperatures ($<450^\circ\text{C}$) without the use of eutectics or prior need of heating to 650°C, to produce

porous silicon with yields comparable to silicon made at temperatures above 650°C. Through a systematic study, we demonstrate the importance and the effects of particle size of the silica feedstock on MgTR temperature.

It is well known that nanoparticles exhibit enhanced reactivity compared to their bulk counterparts due to an increase in surface energy from their high surface to volume ratio. It is thus possible to exploit this nanoscale effect by using silica nanoparticles in order to activate the MgTR reaction at low temperatures. However, the effects of silica particle sizes on MgTR have not been investigated yet. In this study, silica nanoparticles of sizes 500, 75 and 20 nm were synthesised using the Stöber method (see S.I.).⁹ These samples, referred to as S500, S75 and S20 respectively, were characterised using electron microscopy and N₂ adsorption (Figure 1 and Table S1). As expected, the particles showed well-defined spherical morphology with a tight particle size distribution and they did not possess any internal porosity.

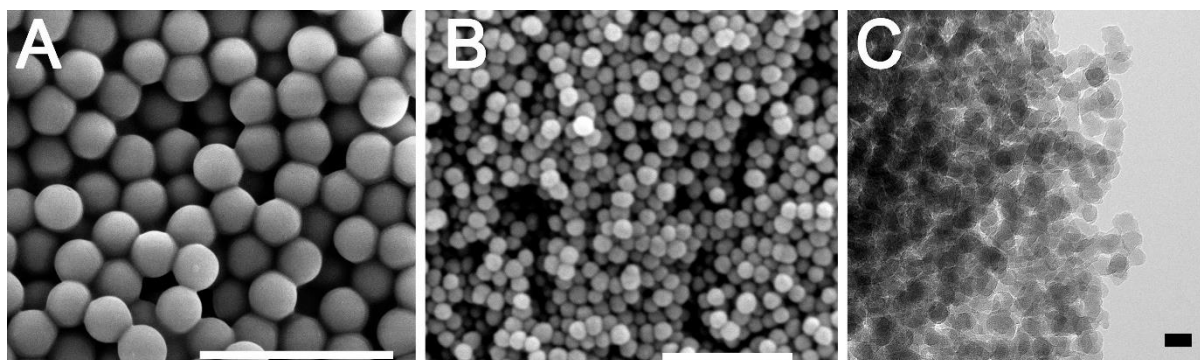


Figure 1: Electron microscopy images of A) S500, B) S75 and C) S20. Scale bars of A, B and C are 2 μm, 500 nm and 20 nm respectively.

The samples of silica were mixed with magnesium and reduced in a furnace at a range of temperatures between 450 and 750°C. The reduction products were then washed with acid to remove Mg-containing species before characterising with SEM to study the morphology and XRD to detect the presence of crystalline silicon. When 500 nm silica (S500) were used, the absence of diffraction peaks for MgTR performed at 450°C indicated that no crystalline product was formed at this temperature, consistent with the literature (Figure 2A). MgTR temperature $\geq 550^\circ\text{C}$ was required to produce crystalline silicon as evident from peaks at 28, 47, 56, 68 and 76°, corresponding to 111, 220,

311, 400 and 331 crystal planes of Si, which matched the polycrystalline silicon standard. There were no peaks that correspond to MgO or unreacted Mg in any of the samples, thus confirming the effectiveness of the post-reaction acid washing.

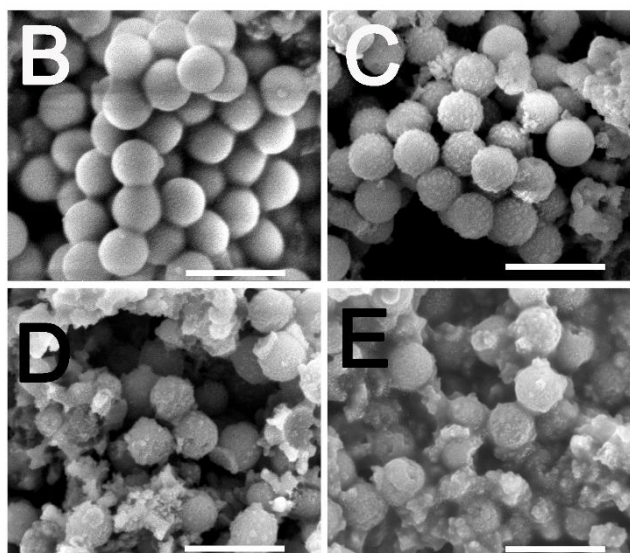
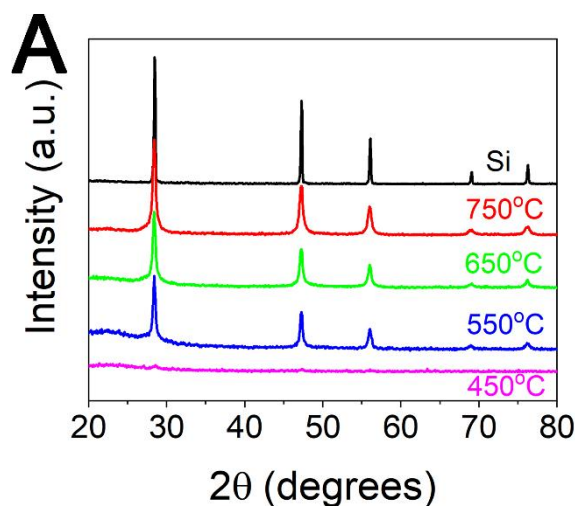


Figure 2: Diffraction patterns of products obtained from reducing S500 at different temperatures, along with a polycrystalline silicon standard (Si, NIST Standard 640d). SEM images of 500 nm silica particles reduced at B) 450°C, C) 550°C D) 650°C, and E) 750°C after washing in HCl are shown. Scale bars for SEM images are 1 μm .

The SEM images of S500 upon MgTR at 450°C showed a lack of any changes in the morphology, confirming that the particles have not undergone reduction. For temperatures of 550°C, specks on the surface of the silica particles can be observed in the SEM images (Figure 2B-D), which are consistent with the formation of silicon crystals reported in the literature.¹⁰ At 650°C and 750°C the spherical morphology was less obvious due to breakage of silica particles from extensive reduction

and from the sintering of the newly formed crystalline silicon nanoparticles, again consistent with the literature.¹⁰ These silicon samples were porous in nature, e.g. S500 reduced at 650°C were mesoporous with some microporosity and had a specific surface area of 179 m²/g (see Figure S2 and Table 2). MgTR using 75 nm silica particles (S75) followed a similar trend, where crystalline silicon was produced at all reduction temperatures except 450°C as shown in Figure S1.

In contrast to S500 and S75, when the 20 nm silica particles (S20) were used as the silica precursor for MgTR, crystalline silicon was produced at 450°C as verified by characteristic sharp peaks in the XRD shown in Figure 3A. The silicon produced had specific surface area of 184 m²/g, similar to the silicon obtained from reducing S500 at 650°C. The formation of crystalline silica was further confirmed by TEM analysis shown in Figure 3B. The Lattice planes are shown by arrows in Figure 3B to highlight the crystallites. In order to determine whether the larger silica samples had produced amorphous Si, we quantified the yields by oxidising the MgTR products and any associated change in weight was measured using thermal gravimetric analysis (TGA). This method allows for quantification of both crystalline and amorphous silicon present in the bulk sample and hence it is preferred over surface analysis using techniques such as XPS.¹⁰

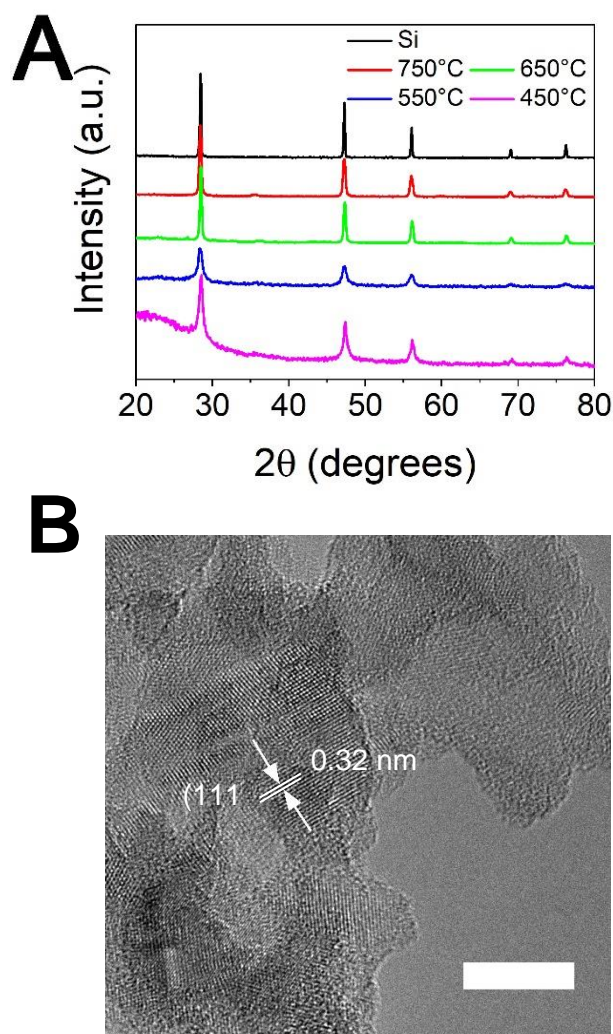


Figure 3: (A) Diffractograms of the reduction products of 20 nm silica particles. (B) TEM image of MgTR products obtained from S20 at 450°C (scale bar is 10 nm). Arrows indicate the crystallites formed.

When the MgTR was carried out at temperatures $\geq 550^\circ\text{C}$, the yields of silicon obtained from different particle sizes were similar irrespective of silica particle size (differences are within the measurement errors, see Figure 4A). However, prominent differences were seen at 450°C and below. 20 nm particles gave a yield of silicon of around 35 and 40 mol% for MgTR temperatures of 400°C and 450°C, while at the same MgTR temperatures ($< 550^\circ\text{C}$), S500 and S75 did not produce any detectable silicon. These results are in strong agreement with the results from XRD, where only 20 nm particles produced crystalline silicon at such low temperatures. Further lowering the MgTR temperature to 395°C resulted in no detectable amount of silicon for any of the silica particles used (data not shown). This is the first evidence of MgTR of silica occurring at temperatures as low as

400°C. These results also show for the first time that for MgTR reaction to occur at low temperatures, there is a particle size threshold: only the particles below this threshold will be able to initiate the MgTR reaction at sub-450°C temperatures.

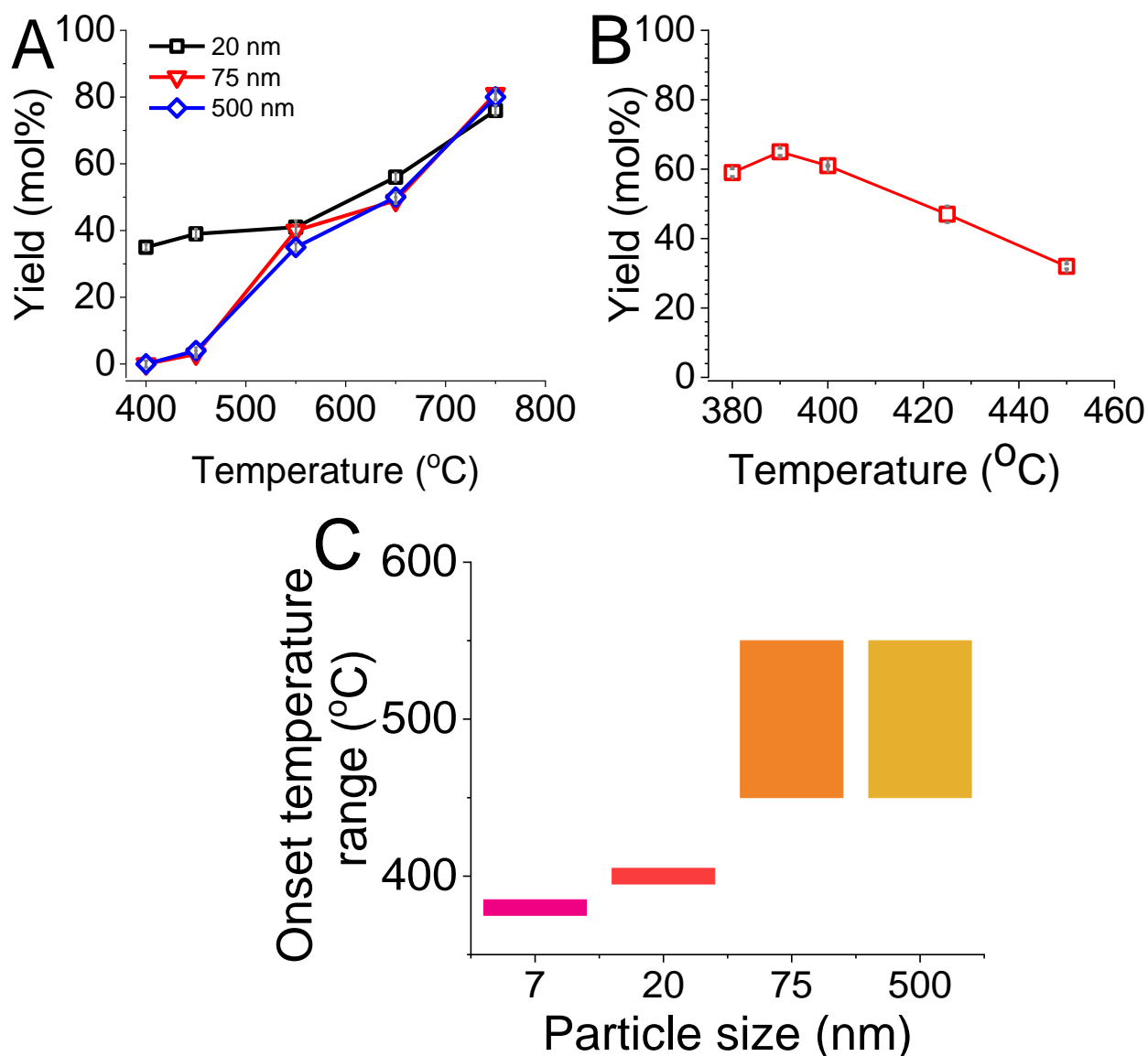


Figure 4: (A) The change in yield with MgTR temperature for different silica particle sizes. (B) Yields as a function of MgTR temperature for 7 nm silica. (C) Temperature brackets for the onset of MgTR with respect to the silica particle sizes.

This particle size threshold for lowering the activation temperature of MgTR is of particular interest. It is likely that using even smaller particles can lower the onset of MgTR further. In order to explore this possibility, 7 nm diameter fumed silica (purchased from Sigma, referred to as F7) was used to probe MgTR at low temperatures.¹¹ F7 was able to produce silicon at 450°C with a specific surface area of

177 m²/g (again similar to that found for S500 at 650°C). Interestingly, F7 produced silicon at temperatures as low as 380°C (Figure 4B) as confirmed with XRD (Figure S3). It is also worth noting that using this commercial silica further demonstrates that the activation of MgTR at lower temperatures exploiting the nanoscale effects is not limited to one type or source of silica particles. When MgTR was performed at 375°C, silicon formation was not detected (data not shown). It was also observed that the yield of silicon from F7 at its onset temperature of 380°C (~60 mol%) was far higher than the yield recorded from S20 at its respective onset temperature of 400°C (35 mol%). The yield of silicon from F7 declined from 390°C as the temperature was raised to 450°C (a decrease from 65 mol% to 32mol%). It is likely that side reactions which consume the freshly formed silicon (e.g. the formation of magnesium silicide) are favoured at different temperatures.

These results show that the temperature needed to activate the MgTR reaction is dependent on the particle size of the feedstock silica. The smaller the particles, the lower the onset temperature (Figure 4C). However, above a certain size (≥ 75 nm), the onset temperature did not reduce. We have therefore shown the first evidence of silica being converted to silicon via the MgTR reaction at a temperature as low as 380°C, using only magnesium as the reducing agent. It is well known that nanoparticles exhibit enhanced reactivity compared to their bulk counterparts arising.^{12, 13} This well-known nanoscale effect is likely to reduce the activation barrier for initiating MgTR reaction, and hence the energy input required to initiate the reaction is lower.¹⁴ This explains our findings where only the smaller silica nanoparticles (≤ 20 nm) react at temperatures ≤ 450 °C.

In conclusion, we have shown for the first time that the particle size of the feedstock silica affects the temperature requirement of MgTR reaction due to the nanoscale phenomenon. The MgTR has an onset temperature which is dependent on particle size. Stöber particles ≥ 75 nm have a reduction onset temperature of ≥ 550 °C. For particles ≤ 20 nm, the onset temperature decreases with particle size, where 20 nm particles were able to reduce at 400°C while 7 nm particles are able to reduce at 380°C. This study shows that it is possible to produce silicon at lower temperatures with minimal compromise to yield. Further studies are required to understand and manipulate the mechanisms of this low temperature process. The findings in this paper paves the way for the development of a

sustainable and scalable MgTR reaction strategy to produce porous silicon for photocatalysis, energy storage and other applications.

4.4. Experimental methods

4.4.1. Materials and reagents

Magnesium powder (99.98%) of -325 mesh grade and ethanol (absolute) were purchased from VWR. Ammonium hydroxide solution (28%), tetraethyl orthosilicate (TEOS 99.9%) and hydrochloric acid (HCl) were purchased from Sigma-Aldrich. Fumed silica was also purchased and used as received from Sigma-Aldrich.

4.4.2. Stöber silica synthesis

Silica nanospheres of various sizes were made via the Stöber method. Ethanol (Absolute, VWR) and TEOS (Sigma-Aldrich) were added to volumetric flask and mixed with a Teflon coated magnetic stirring bar. After 10 minutes of mixing, deionised water was added, and following 10 more minutes of mixing, 28% ammonium hydroxide solution was added dropwise to the solution. The amounts of ethanol and ammonium hydroxide were varied to achieve the desired concentration of ammonium hydroxide. The solution was stirred for a further 24 hours at 20°C, followed by centrifugation at 5000 rpm for 15 minutes to separate the particles from the solution. The particles were rinsed with deionised water to remove excess ethanol, ammonium hydroxide and TEOS, then centrifuged once more at 5000 rpm for 15 minutes, before being dried overnight at 80°C. Smaller particles (≤ 20 nm) were separated using a dialysis membrane with a 14 kDA molecular weight cut-off, immersed in a deionised water bath. The conductivity (inverse resistance) of the water bath was measured at 4-hour intervals using a multimeter on 2 M Ω resistance setting, and when two consecutive readings were the same, the water in the bath was removed and replenished with fresh de-ionised water to introduce a new diffusion gradient. This was repeated several times until the conductivity was unchanging, then the particles within the dialysis membrane were separated by drying on an evaporating dish.

4.4.3. Silicon synthesis

The preparation of the precursors for MgTR was according to our previously reported method MENEDELEY CITATION PLACEHOLDER 1 using magnesium powder (325 mesh, 99.8%, Alfa Aesar) and the synthesised Stöber silica nanospheres a weight ratio of 1:1, giving the stoichiometric mole ratio of 2.5:1. In every reduction, 0.5 g of magnesium and 0.5 g of silica were used. In mixed size silica precursors, the total mass of silica used in each reaction remained the same. A ramp rate of 1°C/min was used for all reductions. Samples were heated at maximum temperatures for a duration of 6 hours then cooled naturally to room temperature.

4.4.4. Analytical techniques

Scanning electron microscopy (SEM) images of the as synthesised and reduced Stöber particles were taken using FEI Inspect F electron microscope. Samples were prepared by dispersing dry silica powder in ethanol and drop casted onto carbon coated aluminium sheets, then gold coated using a sputter coater. **Transmission electron microscopy (TEM) imaging** was performed on a Jeol R005 80-300kV transmission electron microscope. Samples were dispersed in ethanol by ultrasonication then drop-casted onto 400 mesh copper TEM grids coated with lacey carbon films (Agar Scientific). TEM images were analysed using Image J software. **Powder X-ray diffraction (XRD)** technique was performed using the Stoe Stadi P (CuIP) diffractometer, with copper $K_{\alpha 1}$ radiation of wavelength 1.5406 Å. 5 diffractograms were collected for each sample within the 2θ range of 1 and 120°, each taking 6 minutes. The diffractograms were combined to reduce background noise, then analysed using WinXPow software. **Thermal gravimetric analysis** was performed using a Perkin Elmer TGA 4000, under continuous flow of oxygen. To ensure complete oxidation of the silicon present, samples were heated from 20°C to 950°C at a rate of 40°C/min, holding at maximum temperature for 24 hours, before cooling at 40°C/min to room temperature. **Surface area and pore size measurements** were performed using a Micromeritics Tristar 3000. Samples were degassed under vacuum at 120°C for 24 hours, then their weights were recorded. Warm and cold free space measurements were taken using He before and after immersing in liquid nitrogen, respectively. Adsorption and desorption

isotherms were then collected within the range of 0.001 and 0.999 P/P_0 using N_2 as the adsorbent whilst samples were immersed in a liquid nitrogen-filled dewar. Specific surface area was deduced from the isotherms by fitting with the BET model. Pore volumes and average pore diameters were deduced using the BJH model on the desorption branch.

4.5. Acknowledgements

The authors thank EPSRC for funding this research (EP/L016818/1, EP/P006892/1 and EP/R025983/1). Dr. Jake Entwistle (University of Sheffield) and Professor Marc Knecht (University of Miami) are thanked for helpful discussions.

4.6. References

1. I. S. Curtis, R. J. Wills and M. Dasog, *Nanoscale*, 2021, **13.4**, 2685-2692.
2. A. G. Cullis, L. T. Canham and P. D. J. Calcott, *Journal of Applied Physics*, 1997, **82**, 909-965.
3. M. N. Obrovac, L. Christensen, D. B. Le and J. R. Dahn, *Journal of The Electrochemical Society*, 2007.
4. N. V. Nemchinova, V. A. Bychinskii, S. S. Bel'skii and V. E. Klets, *Russian Journal of Non-Ferrous Metals*, 2008, **49**, 269-276.
5. Z. Bao, M. R. Weatherspoon, S. Shian, Y. Cai, P. D. Graham, S. M. Allan, G. Ahmad, M. B. Dickerson, B. C. Church, Z. Kang, H. W. Abernathy, C. J. Summers, M. Liu and K. H. Sandhage, *Nature*, 2007, **446**, 172-175.
6. J. E. Entwistle, G. Beaucage and S. V. Patwardhan, *Journal of Materials Chemistry A*, 2020, **8**, 4938-4949.
7. Y. Lai, J. R. Thompson and M. Dasog, *Chemistry - A European Journal*, 2018, **24**, 7913-7920.
8. S. A. Martell, Y. Lai, E. Traver, J. MacInnis, D. D. Richards, S. MacQuarrie and M. Dasog, *ACS Applied Nano Materials*, 2019, **2**, 5713-5719.
9. W. Stöber, A. Fink and E. Bohn, *Journal of Colloid And Interface Science*, 1968, **26**, 62-69.
10. J. Entwistle, A. Rennie and S. Patwardhan, *Journal of Materials Chemistry A*, 2018, **6**, 18344-18356.
11. These were fumed silica and it was used due to practical difficulties in obtaining meaningful quantities of <20 nm Stöber silicas.
12. Z. Y. Zhou, N. Tian, J. T. Li, I. Broadwell and S. G. Sun, *Chemical Society Reviews*, 2011, **40**, 4167-4185.
13. X. Li, H. Tang, X. Lu, S. Lin, L. Shi and Z. Huang, *Entropy*, 2015, **17**, 5437-5449.
14. Z. Y. Huang, X. X. Li, Z. J. Liu, L. M. He and X. C. Tan, *Journal of Nanomaterials*, 2015, **16**, 388-396.

5. Nanoscale triggering effect unlocks sustainable manufacturing of high-performance porous silicon anodes

*Maximilian Yan and Siddharth V. Patwardhan**

Department of Chemical and Biological Engineering, Green Nanomaterials Research Group, The University of Sheffield, Mappin Street, Sheffield S1 3JD, UK. *s.patwardhan@sheffield.ac.uk

5.1. Contributions

I performed all the reductions, XRD, TGA, gas adsorption experiments and collected all SEM images. I made all the electrodes, constructed the coin cells and performed all electrochemical testing. The TEM images were collected by Dr. Colm O'Regan. I prepared the initial manuscript, and Prof. Siddharth Patwardhan helped with the editing.

This chapter has been redacted

6. Large-scale manufacturing of porous silicon via the magnesiothermic reduction: a techno-economic analysis

Maximilian Yan ^{a,b}, Sarah Martell^b, Mita Dasog^b, Solomon Brown^a and Siddharth V. Patwardhan^{a*}

^a *Department of Chemical and Biological Engineering, The University of Sheffield, Mappin Street, Sheffield S1 3JD, United Kingdom.*

^b *Department of Chemistry, Dalhousie University, 6274 Coburg Road, Halifax, NS B3H 4R2, Canada.*

* *Corresponding author, s.patwardhan@sheffield.ac.uk*

6.1. Contributions

I performed the technoeconomic calculations and prepared the manuscript. SP helped with the editing of the manuscript. Experimental planning and data collected for this paper were jointly performed by me and SM. In particular, SM performed two-step reductions and measured the associated yield. I performed low-temperature (360°C and 380°C) and baseline reductions as well as the yield measurements for both reductions. I also performed electrochemical testing. SM led, while I assisted with the synthesis of the Stöber particles used in the two-step, baseline and low-temperature reduction. MD and SP advised on the experimental planning and SB advised on planning of the techno-economic analysis.

This chapter has been redacted

7. Conclusions and outlook

7.1. Conclusions

The increase in demand for porous silicon due to the growth of the lithium-ion battery market has prompted the work presented in this thesis. The carbothermal reduction is a suitable, well-established process for producing electronic grade silicon where high-purity wafers are required. Electronic grade silicon is not suitable as an anode material for lithium-ion batteries, and therefore the huge amounts of energy required by the carbothermal process is not warranted.

The magnesiothermic reduction is the most promising replacement for the carbothermal reduction, as it operates at $\sim 650^\circ\text{C}$ and produces porous silicon as opposed to a dense ingot. This process was studied in this thesis, in particular, the economics of the process, as well as strategies to improve the process in favour of the economics.

Prior to the studies in this thesis, it was generally accepted that the onset of reduction could be seen at 450°C , giving a poor yield ($<10\%$), and that the yield increased when higher temperatures were used. The reduction is most often carried out at a minimum of 650°C which is the melting point of Mg. At and above this temperature the reaction could proceed to give an appreciable yield. The work presented in Chapter 4 of this thesis demonstrated for the first time the dependence of reaction onset temperature on particle size of the silica. A cut-off exists at 20 nm, whereby particles smaller than this would not undergo a reduction at 450°C . 20 nm particles could be reduced by Mg at 450°C , producing a yield of 35 mol% while 7 nm fumed silica could be reduced at 380°C , producing a yield of Si of 60 mol%. The latter yield was comparable to that achieved at 650°C .

Given that the reduction has not previously been reported to proceed at such low temperatures, little is understood about the mechanisms of the reaction. A curious trend is the increase in yield when the reduction temperature was lowered from 450 to 380°C . This indicates closely competing reaction kinetics, and different reactions are favoured at different temperatures within this range. If the low

temperature reduction method were to be considered for scale-up, future work should focus on building an understanding of the kinetics and mechanisms between 380 and 450°C.

From a process economics perspective, lowering the reduction temperature, decreasing dwell time and increasing the ramp rate decreases energy costs.

7.2. Outlook

A number of changes could be made to the process parameters in favour of process economics however it is important to remember that a tension exists between the different heating steps, the yield, and the properties of the resulting silicon. From existing studies, it is possible to predict how each of the dwell time, ramp rate and reduction temperature affect the pore properties, and to a lesser extent, the yield. However, it is impossible to predict the result of changing a combination of these conditions. Therefore a 'black box' still exists in our understanding and to remove it would allow us to efficiently tune and optimise the reaction without performing large amounts of iterative experiments. For example, it is well known that higher ramp rates encourage sintering, due to rapid heat build-up and insufficient dissipation. This heat build-up is a result of rapid external heat input, causing the reaction to proceed at high rates, releasing even more heat due to its exothermic nature. This might mean that a lower dwell time could be used, or even a lower temperature. Investigating a combination of just 3 different ramp rates for each of 3 different temperatures and 3 different dwell times to find a trend would require a minimum of 27 reductions. This number quickly multiplies to over 100 reductions when investigating the effect of adding salts or performing repeats. Yet, even with a dataset this large, it would still be difficult to then 'translate' these results to other types of silica, given the wide variety of existing types.

The MgTR has been studied heavily since it was first reported in 2007, and a range of reduction conditions and silica feedstocks have been used. High yields and specific capacities have been reported in many studies however rarely were the same set of conditions and feedstocks used in multiple studies. This indicates from a materials chemistry perspective that there may not be a single type of silica which possesses a specific set of properties ideal for the MgTR to proceed and produce

high performing silicon. Rather it indicates that silica with different properties require different conditions to be converted into high performing silicon.

Throughout the temperatures considered here, the SiO_2 remains a solid, which means that that the reaction is mass transfer limited. Thus, feedstocks with different structural properties will undergo the reduction via different mechanisms and kinetics. Reaction kinetics are dependent on the reaction conditions, so a set of conditions which works for one type of feedstock may not for another. Being able to map the different kinetics and mechanisms to feedstock properties is the first step in determining the optimum conditions for any given silica type.

The choice of feedstock depends on its price and availability, both of which are affected by geopolitical factors. It follows that, economically, there may not be an 'ideal' silica, since silica that is available in great abundance today may become severely affected by supply chain issues tomorrow, causing its price to soar. If the same set of product properties could be achieved with different types of silica simply by changing the reduction conditions, then the choice of silica could be made based solely on its market price. This would ensure that the MgTR remains feedstock versatile and supply chain independent.

An ideal strategy would describe the best combination of reduction conditions to exploit reaction kinetics and thermodynamics, along with the correct particle sizes to use to have better control of reactant distribution and homogeneity whilst still maintaining a low Mg: SiO_2 ratio.

Understanding the kinetics and mechanisms would enable a MgTR 'toolkit' to be built, whereby the exact conditions can be stated to convert a given silica feedstock into silicon with a set of desired properties. It may then be possible to improve the yield and product quality while decreasing energy costs or at least, have a meaningful discussion, with quantitative proof, on whether sacrificing one metric while favouring another would improve the overall economics of the process. By painting a complete picture of what is happening at every step of the reaction from a kinetic study, it will be possible to make the changes to the process for economic benefit, without the need for large amounts of experiments.

8. Appendix

8.1. Chapter 4 Supplementary information

Electronic Supplementary Information

Exploiting nanoscale effects enables ultra-low temperature to produce porous silicon

*Maximilian Yan and Siddharth V. Patwardhan**

Department of Chemical and Biological Engineering, Green Nanomaterials Research Group, The University of Sheffield, Mappin Street, Sheffield S1 3JD, UK. *s.patwardhan@sheffield.ac.uk

Table S1: Concentration of NH₃ used in Stöber silica synthesis and the resulting silica particle sizes measured by TEM.

[NH ₃] (M)	Particle diameter (nm)	Internal specific surface area (m ² /g)
0.01	20 ± 2	45
0.05	75 ± 8	9
1.13	500 ± 17	6

Table S2: Properties of silica and their reduction products at different temperatures are summarised.

Sample	Silicon Yield (mol%)	Specific surface area (m ² /g) ^a	Total pore volume (cm ³ /g)
S20	n/a *	189	0.79
S500	n/a *	7	0.01
S20 450°C	35	184	0.24
S20 650°C	56	92	0.19
S500 650°C	50	179	0.29
F7	n/a *	424	0.7
F7 380°C	58	70	0.16
F7 450°C	31	177	0.47

^a This is total surface area (internal and external).

* This is the feedstock silica samples which has not undergone reduction and hence a yield of silicon is not applicable.

Table S3: Crystal planes identified in Figure S4 and associated d-spacings, 2θ angles and miller indices.

d-spacing (nm)	2θ (degrees)	Miller Indices
0.32	28	(111)
0.20	48	(220)
0.17	56	(311)
0.14	76	(331)

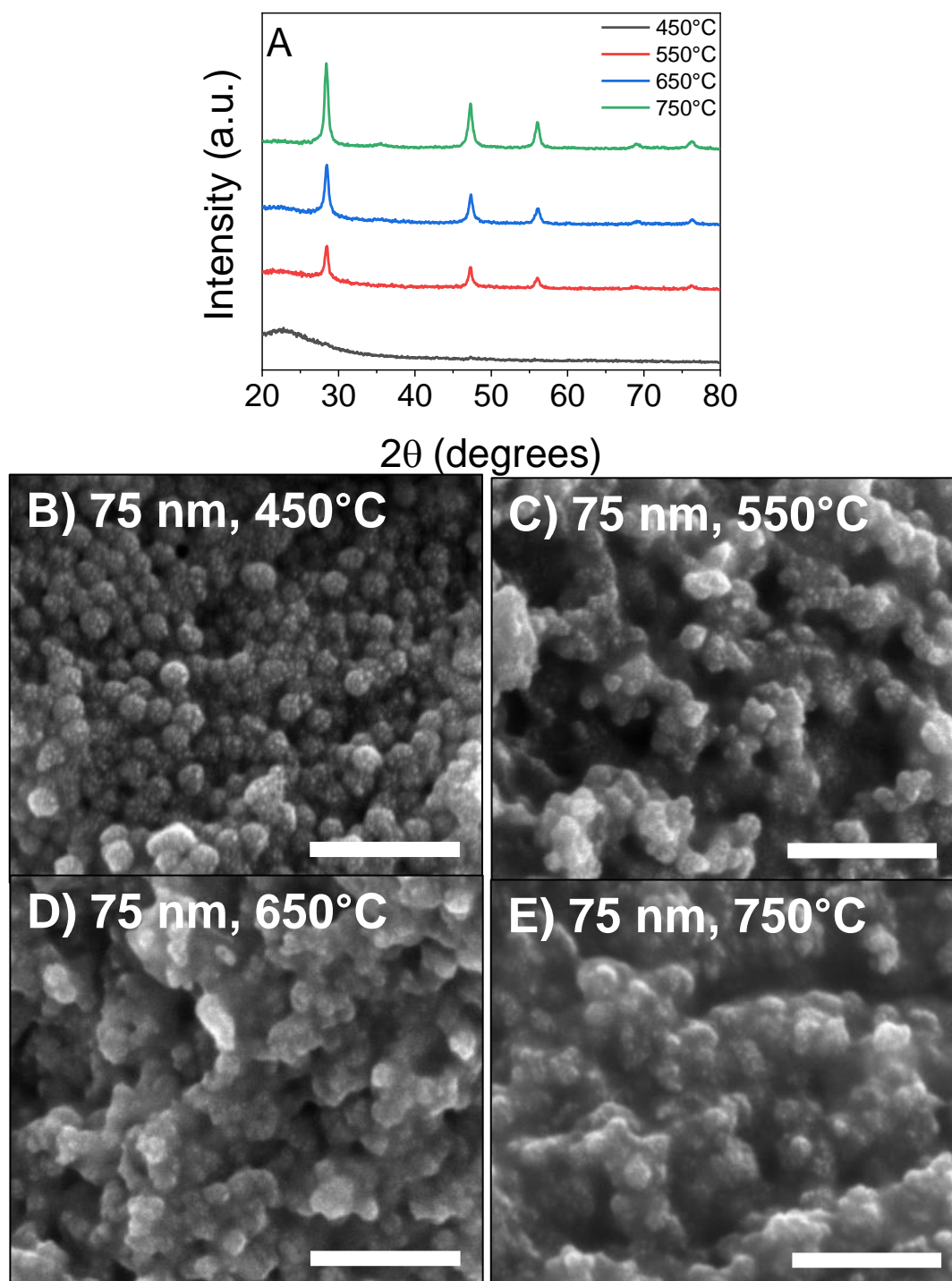


Figure S1: (A) XRD and (B-E) SEM images of 75 nm particles (S75) reduced at different temperatures. Scale bars of SEM images are 500 nm. All data was collected on samples after HCl etching.

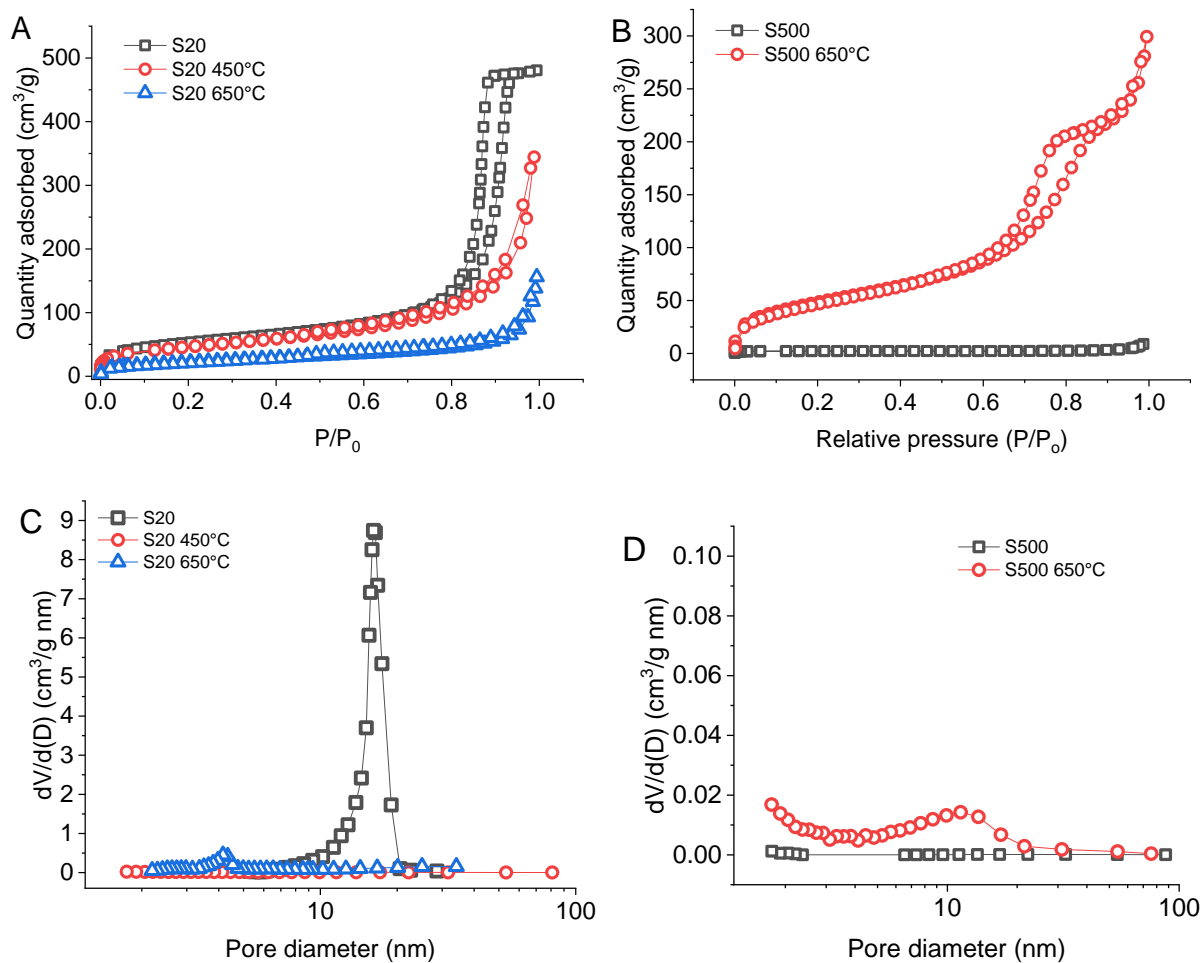


Figure S2: The isotherms for pristine and reduced A) S20 particles* and B) S500 particles are given. C) The BJH desorption pore sizes are shown for C) S20 and D) S500 samples, both reduced and unreduced samples. *While S20 does not have any internal surface area, the data in parts (A) and (C) include external surface area.

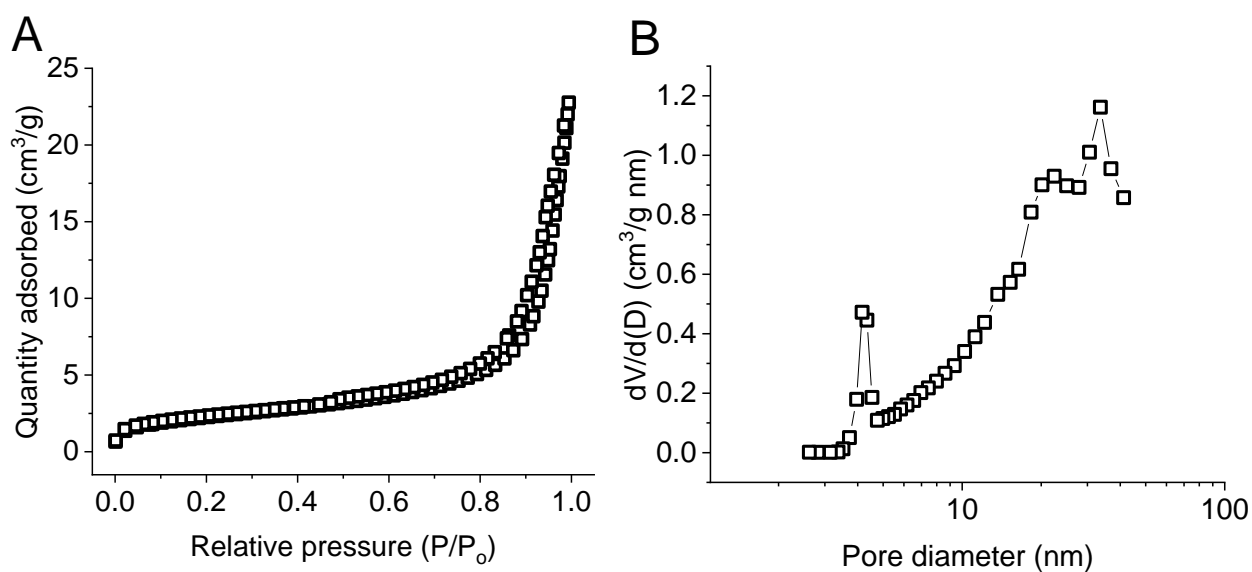


Figure S3: A) Gas adsorption isotherm and B) pore size distribution of 75 nm particles (S75) reduced at 650°C.

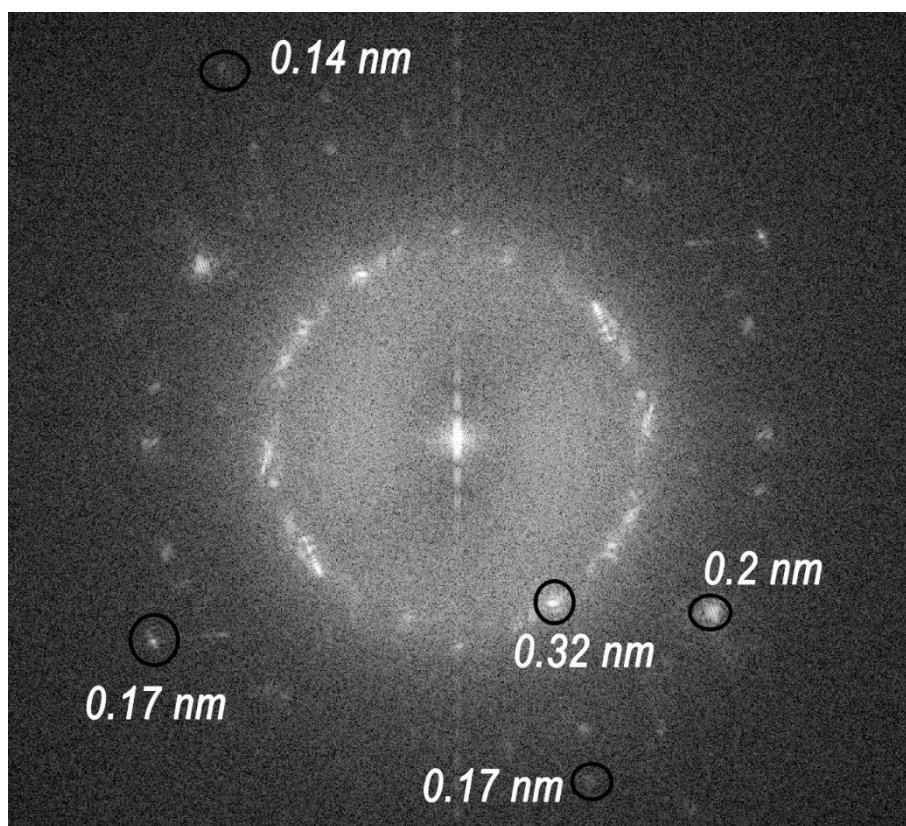


Figure S4: FFT analysis of the TEM image shown in Figure 3B. d-spacings for all identified crystal planes are shown on the image and associated parameters are listed in Table S3.

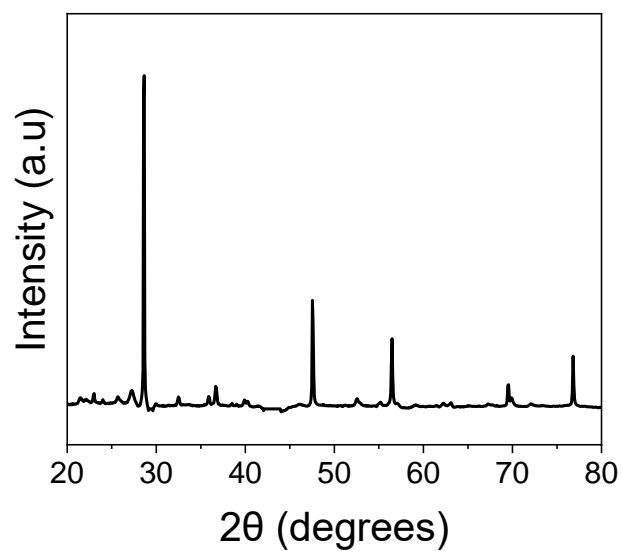


Figure S5: XRD of the reduction of F7 at 380°C after washing in HCl.

**Supplementary information for Chapters 4 and 5 has
been redacted**